

Durham E-Theses

Full-orbit studies of wave-particle interaction on the Mega Ampere Spherical Tokamak

SUN, TIAN TIAN

How to cite:

SUN, TIAN TIAN (2021) *Full-orbit studies of wave-particle interaction on the Mega Ampere Spherical Tokamak*, Durham theses, Durham University. Available at Durham E-Theses Online:
<http://etheses.dur.ac.uk/14253/>

Use policy

The full-text may be used and/or reproduced, and given to third parties in any format or medium, without prior permission or charge, for personal research or study, educational, or not-for-profit purposes provided that:

- a full bibliographic reference is made to the original source
- a [link](#) is made to the metadata record in Durham E-Theses
- the full-text is not changed in any way

The full-text must not be sold in any format or medium without the formal permission of the copyright holders.

Please consult the [full Durham E-Theses policy](#) for further details.

Full-orbit studies of wave-particle interaction on the Mega Ampere Spherical Tokamak

Tiantian Sun

A thesis presented for the degree of
Doctor of Philosophy



Centre for Advanced Instrumentation

Durham University

United Kingdom

September 2021

Abstract

Energetic particles with super-Alfvénic speeds could potentially drive Alfvénic instabilities in a magnetically confined plasma. The driven waves can influence the fast particle distribution function as energetic particles are redistributed or lost to the vessel wall leading to a reduction in energetic particle confinement and heating efficiency. This thesis investigates the interaction between particles and waves via full orbit numerical simulations. The work presented herein takes steps towards the development of a capability to assess whether future reactor scenarios will be susceptible to these adverse effects or not.

A full orbit particle tracking code has been developed to calculate particle trajectories and more importantly to compute particle orbital frequencies as they are followed in the simulation. Based on the wave-particle resonance condition, resonant particles are identified using this code for realistic tokamak geometries.

Experimental observations of fast-ion driven waves on the MAST tokamak are presented. Magnetic perturbations in the kilo-Hertz range are detected by a set of high resolution Mirnov coils during the neutral beam injection heating phase where the mode frequency is observed to chirp downwards over the course of a magneto-hydrodynamics (MHD) burst. A decrease in fast-ion deuterium alpha signals is found to be correlated with the electromagnetic bursts indicating fast ion redistribution during the MHD activity. Simulation results suggest that the increase in plasma pressure is disproportional to the increase in NBI heating power in the presence of MHD modes. The effect of instabilities on energetic particle behaviour has been analysed by calculating resonance maps and resonant particle orbits. Full orbit calculations show that the chirping frequency broadens the wave-particle resonance region which can result in enhanced particle transport.

Preliminary attempts have been made to evaluate fast particle transport induced by chirping modes using the non-linear full orbit HALO code. The chirping behaviour of the mode frequency is simulated by an ad-hoc function similar to experimental measurement. Calculations are performed for a simple cylindrical tokamak geometry and a mocked-up alpha particle distribution. An $n = 6$ toroidal Alfvén eigenmode (TAE) is found numerically for this equilibrium. The results of the simulations show that fast particles are transported outwards from

the plasma centre when chirping modes are present while no significant particle transport is seen when the mode frequency is constant. The level of transport is affected by either mode amplitude or chirping rate. These results suggest that the inclusion of a chirping effect is necessary to study particle redistribution in the presence of fast-ion modes when considering plasma scenarios in the future.

Acknowledgements

I would like to thank my supervisors Ray Sharples, James Buchanan and Michael Fitzgerald for their support and guidance throughout the project. Their supervision has been of great value. I would like to thank Michael Fitzgerald for helping me get settled when I first moved to Culham. I would also like to thank Rob Akers for providing assistance with the `LOCUST` code and Asger Jacobsen for providing the FIDA data. I would also like to thank Sam Gibson and Lucy Kogan for providing MAST equilibrium data. I would like to thank James Buchanan for assistance with the `HALO` code development and demonstration in Chapter 5, proof reading and suggestions for improvement of the thesis.

This work was financially support by CSC, EPSRC, CCFE and Durham University. Simulations were performed using the computational resources at the Culham Centre for Fusion Energy. Much of the data visualisation of the results uses plotting libraries in `Python`.

Last but not least, I would like to thank my friends and family for your support and encouragement all the time.

Contents

| | |
|--|--------------|
| Declaration | ix |
| List of Figures | xi |
| List of Tables | xxiii |
| 1 Introduction | 1 |
| 1.1 World energy | 1 |
| 1.2 Fusion energy | 2 |
| 1.3 The Tokamak | 7 |
| 1.4 The MAST and MAST-U Tokamaks | 8 |
| 1.5 Neutral beam injection | 11 |
| 1.6 Diagnostics | 14 |
| 1.6.1 Mirnov coil array | 15 |
| 1.7 Fast ions | 15 |
| 1.8 Outline | 20 |
| 2 Theoretical review | 21 |
| 2.1 Charged particle motion in magnetically confined devices . . . | 22 |

| | | |
|----------|--|-----------|
| 2.1.1 | Gyro motion | 22 |
| 2.1.2 | $\mathbf{E} \times \mathbf{B}$ drift | 23 |
| 2.1.3 | ∇B drift | 24 |
| 2.1.4 | Curvature drift | 25 |
| 2.1.5 | Constants of motion | 25 |
| 2.2 | Magnetohydrodynamics | 27 |
| 2.3 | Equilibrium | 30 |
| 2.4 | MHD instability | 36 |
| 2.4.1 | Linearisation | 37 |
| 2.4.2 | Normal mode formulation | 39 |
| 2.4.3 | Homogeneous plasmas | 40 |
| 2.4.4 | Landau damping | 42 |
| 2.5 | Kinetic-MHD model | 44 |
| 2.5.1 | Guiding centre theory | 45 |
| 2.5.2 | Linear perturbation theory | 47 |
| 2.5.3 | Resonance condition | 51 |
| 3 | Particle tracking in electromagnetic fields | 55 |
| 3.1 | The Boris solver | 57 |
| 3.2 | Coordinate transformations | 59 |
| 3.3 | Initialisation | 62 |
| 3.4 | Workflow of the particle pushing code | 63 |
| 3.5 | Code validation | 64 |
| 3.6 | Calculations of particle orbits in MAST | 67 |
| 3.7 | Calculations of motion frequencies | 71 |
| 3.8 | Summary | 77 |
| 4 | Fast-ion driven modes | 79 |

| | | |
|----------|---|------------|
| 4.1 | Plasma scenarios | 79 |
| 4.2 | FIDA diagnostics | 83 |
| 4.3 | Calculations of resonance maps | 87 |
| 4.4 | Resonant transport | 90 |
| 4.5 | Summary | 94 |
| 5 | Fast ion transport due to chirping modes | 97 |
| 5.1 | Introduction | 97 |
| 5.2 | The HALO model | 98 |
| 5.2.1 | Wave-particle energy transfer | 98 |
| 5.2.2 | Monte-Carlo modelling | 100 |
| 5.2.3 | Noise reduction | 101 |
| 5.2.4 | Inputs for HALO | 102 |
| 5.3 | Modelling chirping modes | 105 |
| 5.4 | Study scenario | 108 |
| 5.5 | Results | 110 |
| 5.6 | Discussion and summary | 120 |
| 6 | Conclusion | 123 |
| 6.1 | Results | 124 |
| 6.2 | Outlook | 126 |
| | Bibliography | 129 |

Declaration

The work in this thesis is based on research carried out at the Centre for Advanced Instrumentation, Department of Physics, University of Durham, England. No part of this thesis has been submitted elsewhere for any other degree or qualification, and it is the sole work of the author unless referenced to the contrary in the text.

Copyright © 2020 by Tiantian Sun.

“The copyright of this thesis rests with the author. No quotation from it should be published without the author’s prior written consent and information derived from it should be acknowledged”.

List of Figures

| | | |
|-----|---|---|
| 1.1 | (a) Experimentally measured fusion cross sections versus centre-of-mass energy. The critical particle energy for a fusion reaction to take place is around 10 keV for the D-T reaction and nearly 100 keV for the D-He ³ or D-D reactions. The maximum cross section of the D-T reaction is also prominently higher than those of the other two reactions and occurs at a relatively low energy of approximately 100 keV. (b) Maxwell-averaged cross section as a function of temperature for reactions of interest to controlled fusion. The D-T reaction is advantageous for realising nuclear reactions after considering a Maxwellian velocity distribution (images taken from [2]). | 3 |
|-----|---|---|

| | | |
|-----|--|----|
| 1.2 | A Lawson diagram shows the requirement of the ion temperature T_i , density n_i and energy confinement time τ_E for gain factors Q and the operational plasma parameters that fusion devices can achieve. Large tokamak programs such as JET, DIII-D or JT-60U are close to a net fusion power $Q = 1$. One of the scientific objectives of the ITER project is to achieve a gain factor of $Q = 10$ to demonstrate the feasibility of fusion energy as an alternative energy source (image taken from [9]). | 4 |
| 1.3 | A schematic diagram of a tokamak. The resulting helical magnetic field is contributed by the toroidal magnetic field generated by the blue toroidal coils and the poloidal magnetic field produced by the grey poloidal coils and plasma current indicated by the green arrowed line circulating the torus. The light purple shadow area shows the plasma confined surface. The helical magnetic field lines sit on this surface which we refer to as the poloidal flux surface and will be discussed in detail in the next chapter (image taken from [15]). | 7 |
| 1.4 | Typical configuration of a spherical (up) and conventional (down) tokamak. The spherical tokamak is compact and the aspect ration $A = R/a$ is normally less than 2 (image taken from [21]). | 9 |
| 1.5 | Schematic diagrams of (a) MAST [22] and (b) MAST-U [23]. A distinct feature of MAST-U is the super-X divertor configuration indicated by the red solid lines in (b). The edge plasmas and impurities can be diverted to the target plates by following the extended magnetic field lines. | 10 |

| | | |
|------|--|----|
| 1.6 | A schematic diagram of a JET neutral beam injector. Neutral atoms undergo ionisation, acceleration, neutralisation (and residual ions are collected by deflection magnets and ion dump) before being injected into the plasma (image taken from [34]). | 12 |
| 1.7 | A numerical solution of the fast ion distribution shows the full and half energy components of the NBI on ASDEX Upgrade. The third and half energy merge together as the background plasma ions slow down and smears the third peak in energy (image taken from [37]). | 14 |
| 1.8 | A typical magnetic spectrogram of MAST discharge for shot #17944. The colour on the 2D graph shows the amplitude of the magnetic perturbation and dominant harmonics with toroidal mode number $n = 1 \sim 4$ are identified [47]. | 16 |
| 1.9 | (a) Dispersion relation of three waves with poloidal harmonics of $m = -1 \sim -3$ in a cylindrical plasma with current and plasma density gradient [55]; (b) Radial structure of TAE continuum in TFTR for $n = 3$. Here, x is the minor radius (image taken from [56]). | 18 |
| 1.10 | Magnetic spectrogram of Alfvénic activities excited by ICRH in JET plasmas [57]. The TAE gap is in approximately 200 kHz while the mode frequency of the elliptic Alfvénic eigenmode (EAE) is about twice ω_{TAE} . Here, s can be approximated by $s \approx r/a$. . . | 19 |

| | | |
|-----|--|----|
| 2.1 | (a) Transverse motions of charged particles in a constant magnetic field; (b) Drift motion in the presence of a small \mathbf{E} field. The positive charge accelerates at the left-half circle and its velocity reaches a maximum value at the top of the circle, point b ; it decelerates at the right-half circle and reaches a minimum velocity at the bottom of the circle, point d . The gyro radius increases as the particle moves upwards from $d \rightarrow b$ and decreases as it moves downwards from $b \rightarrow d$. The particle trajectory cannot be closed and the particle drifts with a velocity \mathbf{v}_E | 24 |
| 2.2 | Contours of the constant equilibrium pressure are nested toroidal surfaces. Both the magnetic field and the current lines lie on the constant pressure surfaces. | 32 |
| 2.3 | Poloidal surface \mathbf{S}_p used to calculate the magnetic flux. | 32 |
| 2.4 | A typical MHD equilibrium profile for a MAST discharge reconstructed by EFIT/EFIT++. The LCFS is labelled with red solid line and the magnetic axis is marked with a red cross '+' (taken from [72]). | 37 |
| 2.5 | Particles with velocity above resonance gain energy from waves and lose energy to waves when below resonance. Landau damping occurs when $\frac{\partial f_{\parallel}}{\partial v_{\parallel}} < 0$ indicating more particles gain energy than lose energy which leads to a net growth in particle energy and damping in wave energy. Landau growth corresponds to a opposite situation. | 44 |

| | | |
|------|--|----|
| 3.1 | Leapfrog scheme. The initial velocity and position are given and updated in a staggered way. The velocity $v_{n-1/2}$ is advanced to $v_{n+1/2}$ after a time interval and the position x_n is updated to x_{n+1} using $v_{n+1/2}$ | 58 |
| 3.2 | Coordinates transformation | 59 |
| 3.3 | Flowchart to summarise the steps of solving the Lorentz equations of a charged particle in an equilibrium magnetic field. | 64 |
| 3.4 | The constant \mathbf{B} field is along the z direction and the computational trajectory of a deuterium ion on $x - y$ plane is a closed circle. . . | 65 |
| 3.5 | (a) x and (b) y dimension of the circular gyro orbit. | 66 |
| 3.6 | Negligible energy variation during the particle tracking. | 67 |
| 3.7 | Top view of the tokamak showing the toroidal projections of different types of particle orbits, where $X = R \cos \phi$ and $Y = R \sin \phi$. . . | 68 |
| 3.8 | Poloidal projections of particle orbits. Markers \star show the initial particle positions. | 69 |
| 3.9 | (a) Deeply and barely trapped particle orbits. Both the full orbit and the G.C. orbit of the deeply trapped particles are illustrated. (b) A potato orbit whose bounce point is on the magnetic axis marked with the symbol \times | 70 |
| 3.10 | (a) An example of a lost orbit whose the G.C. position maintains confined but the full orbit is beyond the confined boundary; in the simulation, the lost boundary is defined as $\psi_n = 1$ corresponding to the black solid line. (b) Plane of Z_{ini} , $\lambda = v_{ }/v$ with $E = 15$ keV, showing domains of confined and lost particles in MAST. . . | 71 |
| 3.11 | Calculations of the poloidal frequencies f_θ by timing a particle passing through the $Z = Z_0$ plane. f_θ is given by $f_\theta = 1/(N_2 - N_1)dt$ where dt is the time interval. | 72 |

| | | |
|------|--|----|
| 3.12 | (a) Temporal evolution of the toroidal angle ϕ of a passing particle; ϕ periodically changes between $-\pi$ to π . (b) Cumulative toroidal angle derived from ϕ is a monotonic function of time. | 73 |
| 3.13 | (a) Temporal evolution of the toroidal angle ϕ of a trapped particle; (b) Cumulative toroidal angle derived from ϕ . Toroidal frequency $f_\phi \approx (\varphi_2 - \varphi_1)/[2\pi(N_2 - N_1)dt] \approx (\varphi_3 - \varphi_1)/[2\pi(N_3 - N_1)dt]$. . . | 75 |
| 3.14 | Orbit averaging in the calculations of poloidal and toroidal fre- quencies. The computational noise reduces as the number of orbit averaging increases. | 75 |
| 3.15 | The toroidal frequency of a passing particle converges as dt re- duces. The particle with $\lambda = 0.75$ is launched from $R = 1.0$ m and $Z = Z_0$ | 76 |
| 4.1 | Time trace for MAST discharge #29210. (a) NBI power, (b) plasma current, (c) line integrated electron density, (d) electron temperature at core, (e) Mirnov coil signals for instability analysis. | 81 |
| 4.2 | (a) The frequencies of MHD bursts and (b) toroidal mode number of the chirping modes are given in the spectrum of the magnetic perturbations during beam injection. | 82 |
| 4.3 | On-axis pressure p_0 evaluated using EFIT++ show the changes in plasma equilibria as the second beam is turned on. p_0 is normalised by the atmospheric pressure p_{atm} | 83 |
| 4.4 | Top view of the MAST showing the toroidal projections of the FIDA vertical and toroidal reference views, together with the NBI beamlines [83]. | 84 |

| | | |
|------|--|----|
| 4.5 | Weight function of the toroidal line of sight FIDA system at three locations: $R = 1.07, 1.14$ and 1.20 m, where the minimum energy $E_{\min} = 45$ keV. Only ions in the coloured region in velocity space can contribute to the measured FIDA signal. The brightness of the colour scales the sensitivity of particles to the FIDA diagnostic, implying that a charge exchange reaction is more likely to take place at $\lambda = -1$ | 85 |
| 4.6 | Marked drops in FIDA radiance are correlated with visible MHD bursts at 140 ms, 147 ms, 155ms, 173ms, 194 ms and 200 ms. . . | 86 |
| 4.7 | Resonance maps identifying particles that can interact with $n = 1$ chirping modes at (a) $t = 150$ and (b) $t = 205$ ms. 100×100 test markers are populated at $R = 107$ cm and $Z = 0$ cm. Chirping frequencies are sampled within the range observed. Possible mathematical solutions to the resonance condition are illustrated in the graphs. Passing and trapped particles are plotted but there are no lost particles since the initial location is close to the core. . | 88 |
| 4.8 | Orbits of the resonant particles labelled with red and blue crosses in the resonance map showing in Fig. 4.7 at $E = 50$ keV. | 89 |
| 4.9 | (a) Resonance map for 100×100 particles at $R = R_0$ and $E = 50$ keV at $t = 150$ ms; (b) mapping resonance map of (λ, Z_{ini}) onto normalised (μ, P_ϕ) phase space. The colours represent the difference between the toroidal and poloidal motion frequencies. . | 92 |
| 4.10 | Orbits of resonant particles with varying P_ϕ | 93 |
| 4.11 | Speculative formation and evolution of structures in the particle distribution F based on the resonance maps. | 94 |

| | | |
|-----|---|-----|
| 5.1 | 2D Hammersley set generated by using prime base of 2 and 3. A total size of 120 markers are distributed uniformly but irregularly in the space of gyro angle $\alpha \in [-\pi, \pi]$ and pitch $\lambda = v_{\parallel}/v \in [-1, 1]$. | 101 |
| 5.2 | Workflow of HALO . A plasma equilibrium is provided by EFIT . Mode eigenfunctions and frequencies are calculated for this equilibrium by the linear MHD code MISHKA in straight field line coordinates and then converted to cylindrical coordinates. (image taken from ref. [89].) | 103 |
| 5.3 | The energy-exchange occurring between the TAE and alpha particles (left) and non-linear growth of the TAE (right) (images taken from Ref. [89]) | 106 |
| 5.4 | The mode frequency $\omega(t)$ is assumed to be a linear function of time. ω_0 is the eigen-frequency computed by the MISHKA code. The ad-hoc chirping frequency are realised by a coefficient η . $\eta < 1$ is for down chirping modes and $\eta > 1$ for up chirping modes. | 107 |
| 5.5 | A circular equilibrium for benchmarking the HALO code. This equilibrium represents a simplified conventional tokamak configuration with a circular poloidal cross section. The magnetic axis is located at $R = 3$ m. ψ_n is the normalised flux surface function and in the range of $0 \leq \psi_n \leq 1$. This equilibrium is used for the calculations throughout this chapter. | 109 |
| 5.6 | Solutions of eigenmodes found by MISHKA for the bulk plasma confined in the circular flux surface as described above. | 109 |

| | | |
|------|---|-----|
| 5.7 | A mocked-up alpha particle distribution function $f_0(E, P_\phi)$ is used in the simulation. f_0 is constructed by a product form $f_0 = h_1(P_\phi)h_2(E)$. Here, the spatial dependence of f_0 is given by h_1 term and the collision drag from background ions and electrons on alpha particles is described in h_2 term. | 111 |
| 5.8 | Time slices for $t = 1-6$ ms of particles being transported from the plasma centre (blue region) to edge (red region) due to a chirping mode. $\langle df \rangle$ is a quantity proportional to the change of the particle number. The mode amplitude $A_0 = 10^{-3}$ is fixed throughout the simulation and the chirp coefficient is $\eta = 0.25$ corresponds to a down chirping frequency. The grey contours are the poloidal flux function from the equilibrium data and the solid grey line labels the LCFS. The blank squares come from the data filtering of $\pm 4\sigma$, where σ is the standard deviation of $\langle df \rangle$ | 112 |
| 5.9 | Asymmetric distribution of the redistributed particles. Inboard and outboard sides refer the radial location R relative to the magnetic axis R_0 | 113 |
| 5.10 | Time slices at 1-6 ms of $\langle df \rangle$ binned in E and P_ϕ space. P_ϕ is normalised by $e\psi_{\text{bry}}$ where ψ_{bry} is the poloidal flux at the boundary (LCFS). Most of resonant particles are at energy $E < 0.5$ MeV. A boundary between the particle loss and gain appears at $P_\phi = 0$ surface. Parameters of the simulation are the mode amplitude $A_0 = 10^{-3}$ and chirp coefficient $\eta = 0.25$ | 114 |

- 5.11 $\langle df \rangle$ is binned in one dimensional space (a) toroidal angular momentum P_ϕ ; (b) normalised poloidal flux ψ_n ; (c) particle toroidal velocity v_ϕ . P_ϕ is normalised by $e\psi_{\text{bry}}$ where ψ_{bry} is the poloidal flux surface function at the boundary (LCFS). Subplots (a) and (c) enjoy high degree of similarity and the change in v_ϕ is likely to be responsible for particle transport in P_ϕ space. Subplot (b) shows particles are transported from plasma centre $\psi_n = 0.1$ to outer region $\psi_n = 0.4$ and the LCFS $\psi_n = 1$. Eventually those particles escape the confinement region and hit on the facing wall. 115
- 5.12 Reduced particle transport in the presence of the eigenmode with a constant mode frequency $\omega_0 = 481$ keV computed by the MISHKA code. The initial mode amplitude is $A(t = 0) = 10^{-3}$. $A(t)$ evolves in time as the mode interacts with particles and is solved consistently by the HALO. The particle transport level is much lower than those induced by a chirping mode. 117
- 5.13 The particle transport level varies with the chirp coefficient η . Calculations with various η track particles for the same time of 6 ms and all curves shown here are the final measures at $t = 6$ ms. The mode amplitudes for all are constant $A_0 = 10^{-3}$ except the one marked with $A = A(t)$ (orange dashed). $\eta > 1$ and $0 < \eta < 1$ correspond to up and down chirping frequencies, respectively. The particle transport enhances with growing $|\eta - 1|$ which states the deviation of the ending mode frequency away from the initial value ω_0 computed by the MISHKA code. The exception is when $\eta = 1$ (non-chirp case). Interestingly whether the mode amplitude evolves in time or not (orange dashed and green solid lines), the particle transport is constantly small. 118

| | | |
|------|--|-----|
| 5.14 | The mode amplitude has an effect on the particle transport induced by a down chirping mode. The change in particle number is largely reduced as the mode amplitude weakens. When A_0 is on the order of 10^{-4} or smaller, the chirping mode will not affect the particle transport. The chirp coefficient $\eta = 0.25$ and the simulation time is 6 ms for all cases. | 119 |
| 5.15 | $\langle df \rangle$ calculated by two different quasi-random sequences, “H1” (solid) and “H2” (dashed or dotted). The simulation results are more diverged with decreasing mode amplitude. | 119 |
| 5.16 | Coefficient of the variation, $CV = \sigma / \mu$, where σ and μ are the standard deviation and mean value, respectively. As A_0 increases, CV is reduced and the results are converged for simulating particles with different initial states. | 120 |

List of Tables

- 1.1 Key parameters for MAST and MAST-Upgrade. The designed size of the plasma in MAST-U remains same as MAST. Operational parameters such the magnetic field and the NBI power are improved by 50% and 25%. The additional off-axis power is expected to alleviate the fast-ion driven instabilities due to a narrow fast ion distribution near the plasma core (table taken from [19]). 11
- 3.1 Data from the simulation results used to calculate the toroidal motion frequency f_ϕ of a passing particle (time step $dt = 1 \times 10^{-10}$). 74

Introduction

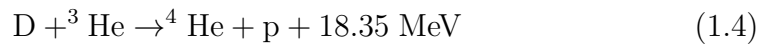
1.1 World energy

The energy supply in today's world primarily relies on traditional fossil fuels, i.e. oil, natural gas and coal. Renewable and clean energy such as nuclear, wind, and solar energy only account for a small fraction of energy consumption globally. Fossil fuel is an ancient and accessible energy source but also limited. Meanwhile, the demand for energy is increasing every year with the progress in people's living standard. Another threat is climate change. A large amount of greenhouse gas emission from fossil fuel burning could change global climate and bring extreme weather events such as drought, flood, storm, etc. These are deadly for agriculture and can cause significant threats and losses to human life. There are problems in clean energy as well. There is no effective solution for disposing radioactive products from fission nuclear reactions and currently the only way to deal with them is to bury them deep underground. Imagine in several decades the earth becomes a radioactive waste dump. Wind and solar energy is easily influenced by the geographic location or the factor of weather and thus cannot be an energy source solely. Fusion energy offers a clean, sustainable alternative power

source which has the potential to address the issues outlined above.

1.2 Fusion energy

Fusion energy makes use of the energy generated by nuclear fusion reactions and it could be a potential candidate solution for future energy requirements because the reactions used do not produce long lived radioactive byproducts, and they do not emit greenhouse gas like burning fossil fuels. The fuel options of fusion are various and abundant. According to Einstein's mass-energy relationship, the fusing of light elements releases a large amount of binding energy if the total mass of the final products is smaller than that of the reacting nuclei. The important nuclear fusion reactions for the isotopes of hydrogen are given below [1]:



For simplicity of notation, the following symbol replacements are made: deuterium $\rightarrow \text{D}$; hydrogen $\rightarrow \text{p}$; helium (α) $\rightarrow {}^4\text{He}$; helium-3 $\rightarrow {}^3\text{He}$.

In order to fuse, two positively charged nuclei must come into contact, winning over the repulsive Coulomb force. The need to overcome the Coulomb barrier in nuclear reactions makes them difficult to initiate. The cross section and reactivity determine the probability of the occurrence of a nuclear reaction. The cross section measures the probability that a pair of nuclei will undergo a nuclear fusion reaction and reactivity is defined as the probability of reaction per unit time per density of target nuclei, as shown in Fig.

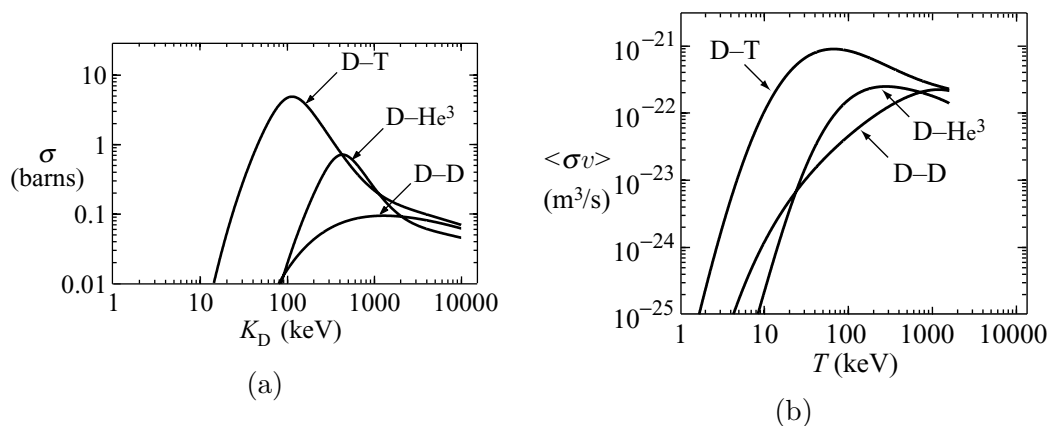


Figure 1.1: (a) Experimentally measured fusion cross sections versus centre-of-mass energy. The critical particle energy for a fusion reaction to take place is around 10 keV for the D-T reaction and nearly 100 keV for the D-He³ or D-D reactions. The maximum cross section of the D-T reaction is also prominently higher than those of the other two reactions and occurs at a relatively low energy of approximately 100 keV. (b) Maxwell-averaged cross section as a function of temperature for reactions of interest to controlled fusion. The D-T reaction is advantageous for realising nuclear reactions after considering a Maxwellian velocity distribution (images taken from [2]).

1.1. The D-T reaction involves the fusion of a deuterium nucleus with a tritium nucleus. It has the highest reactivity at lowest reaction temperature and hence is the easiest of all the fusion reactions to initiate and produces a significant amount of nuclear energy. The reactivity of the D-T reaction $\langle\sigma v\rangle$ peaks at a temperature of ~ 15 keV. At temperatures as high as this Deuterium and Tritium are fully ionised and form plasmas.

To realise thermonuclear fusion power, there are two basically different approaches. The first method is inertial confinement fusion (ICF) [3]. This is a process in which the surface of a small pellet containing the fusion fuel is rapidly heated by high-energy lasers or particle beams. By a rocket-like inward reaction the pellet implodes and then the fusion fuel is compressed to super high densities and is adiabatically heated until the pellet core is brought to ignition. Studies and experiments are on going in some research institutes, such as the National Ignition Facility (NIF) at Lawrence Livermore

National Laboratory [4]. A recent experiment at NIF generated more than 1.3 MJ of fusion energy - around 70% of the energy put in by the laser, nearly achieving an ignition (the energy losses are balanced by the alpha-particle heating) [5]. Another form of nuclear fusion is magnetic confinement fusion (MCF), whereby the charged plasma is confined by a magnetic field. It is also the focus of this thesis. One of the most common approaches to MCF is by means of the tokamak configuration, such as ITER [6], JET [7] and JT-60SA [8].

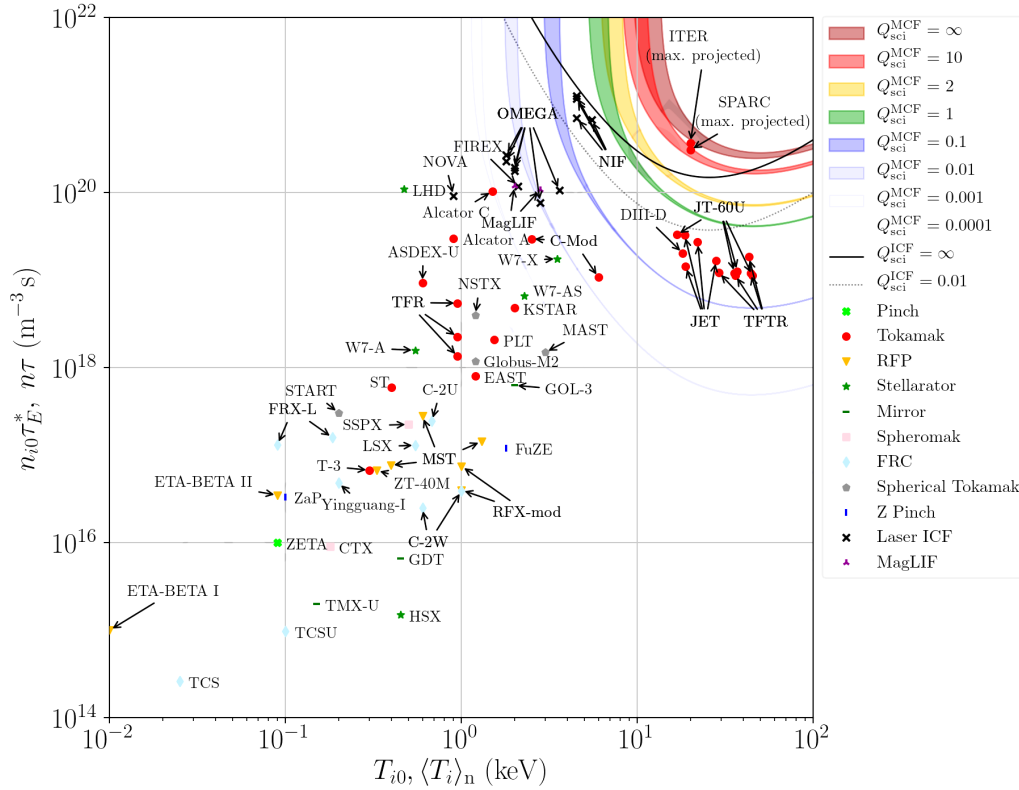


Figure 1.2: A Lawson diagram shows the requirement of the ion temperature T_i , density n_i and energy confinement time τ_E for gain factors Q and the operational plasma parameters that fusion devices can achieve. Large tokamak programs such as JET, DIII-D or JT-60U are close to a net fusion power $Q = 1$. One of the scientific objectives of the ITER project is to achieve a gain factor of $Q = 10$ to demonstrate the feasibility of fusion energy as an alternative energy source (image taken from [9]).

In 1955, J. D. Lawson proposed a useful expression demonstrating the re-

quirement for fusion power balance, that is, to produce net fusion energy, the plasma must be confined by a device at a high temperature T at a sufficiently high density n and for long enough time τ_E so that the fusion power released is greater than the externally applied heating power and this is often referred to as the ‘Lawson criterion’ [10, 11]. The power balance equation is written as

$$P_{heat} - \frac{W}{\tau_E} - P_{rad} = 0. \quad (1.5)$$

Here, P_{heat} is the heating power. The term W/τ_E refers to the thermal conduction loss where τ_E is the energy confinement time and the plasma stored energy per unit volume W is given by the density and temperature of electrons and ions

$$W = \frac{3}{2}(n_i T_i + n_e T_e). \quad (1.6)$$

The radiation losses P_{rad} in fusion plasmas mainly include the Bremsstrahlung radiation which comes from the Coulomb collision between particles, cyclotron radiation because charged particles orbit around the magnetic field lines, and line radiation due to incompletely ionised impurities [12]. It is not economic to power the plasma constantly using external heating to generate electricity since this often consumes more energy than the input due to inefficiencies in energy conversion. Each D-T reaction releases $E_f = 17.6$ MeV energy in the form of the kinetic energy of a neutron and an α particle ($E_\alpha = 3.5$ MeV). Self-sustaining operation can be obtained by self-heating via the produced α particles so that the external energy supply can be saved. If we assume that the heating power is provided by α particles, then

$$P_{heat} = P_\alpha, \quad (1.7)$$

where P_α the alpha power per unit volume. If we assume a 50-50 D-T fuel mixture and equal temperature of ions and electrons, that is, $n_i = n_e = n/2$

and $T_i = T_e$, P_α can be written as

$$P_\alpha = \frac{1}{4} E_\alpha n^2 \langle \sigma v \rangle \quad \text{W/m}^3. \quad (1.8)$$

Attempts have been made to evaluate the radiation losses such as electron-ion Bremsstrahlung and electron cyclotron radiation with relativistic correction [13, 14]. If we are being optimistic on the radiation so the emission can be completely reflected back and absorbed by the plasma, then the power balance relation can be given by

$$\frac{W}{\tau_E} = P_\alpha, \quad (1.9)$$

where the radiation power loss is assumed to be zero for simplicity. Using the expression for the stored energy in Eq. (1.6), the requirement for a self-sustaining plasma can be written as

$$n\tau_E > \frac{12T}{E_\alpha < \sigma v >}. \quad (1.10)$$

A Lawson diagram as shown in Fig. 1.2 demonstrates the minimum requirements for obtaining varying scientific gain Q_{sci} factor defined by the ratio of fusion power and external heating power P_{heat} :

$$Q_{sci} = P_{fus}/P_{heat}. \quad (1.11)$$

Eq. (1.10) corresponds to the $Q_{sci} = \infty$ curve where there is no heating source and the plasma temperature is maintained via the collision process with fusion products, i.e., alpha particles. Progress has been made to improve the energy confinement and operation towards the self-sustained burning condition via either MCF or ICF approach on contemporary machines, such as the ITER project [6], which is targeting a first plasma in 2025 and is aiming at $T_i \sim 18$ keV and a high fusion gain of $Q \sim 10$.

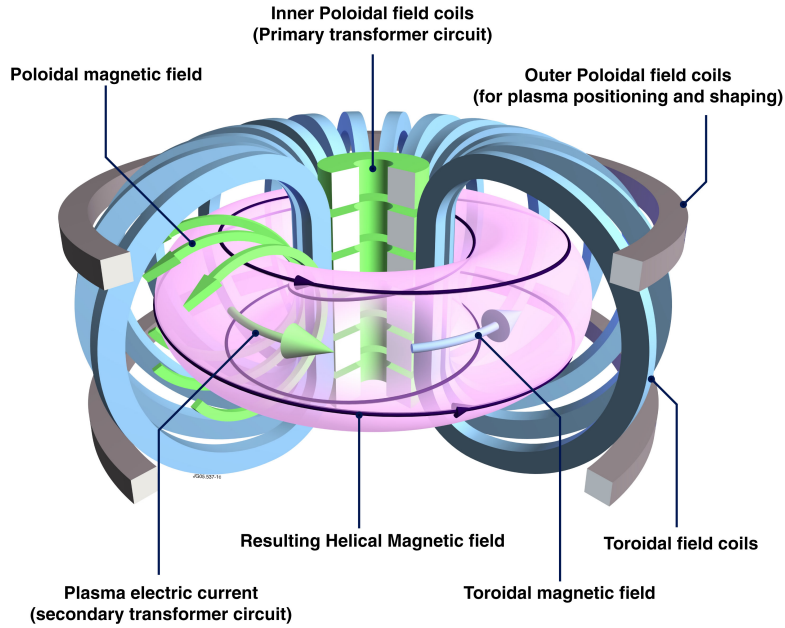


Figure 1.3: A schematic diagram of a tokamak. The resulting helical magnetic field is contributed by the toroidal magnetic field generated by the blue toroidal coils and the poloidal magnetic field produced by the grey poloidal coils and plasma current indicated by the green arrowed line circulating the torus. The light purple shadow area shows the plasma confined surface. The helical magnetic field lines sit on this surface which we refer to as the poloidal flux surface and will be discussed in detail in the next chapter (image taken from [15]).

1.3 The Tokamak

The tokamak comes from a Russian acronym “Toroidal’naya Kameras Magnitnymi Katushkami”, which means a device whereby the fusion plasma is confined in a torus shaped magnetic field in a toroidal chamber. A schematic diagram of a tokamak is presented in Fig. 1.3. The plasma is confined in a vacuum vessel and the initial plasma is usually formed by the central solenoid (CS) that supplies a changing magnetic flux through the the torus and induces a toroidal electric field. A distance between the plasma and the facing materials is obtained by the helical magnetic configuration. The toroidal components of the field is created by the toroidal field (TF) coils which

pass through the inner and outer vessel. The motions of charged particles are the gyro motions following field lines and the end loss can be avoided by the closed toroidal field. However, this alone is insufficient to confine the plasma completely. The gradient and curvature of the toroidal magnetic field lead to opposite drift motions for electrons and ions. Then the charge separation generates an electric field and plasmas will rapidly hit the wall due to the $E \times B$ drift. A set of poloidal field (PF) coils is located symmetrically about the mid-plane for shaping, vertical stability and radial force balance. It is worth noting that the driven plasma current is the main source of the poloidal field rather than the PF current. Combinations of the toroidal and poloidal magnetic components result in rotating field lines traversing the torus and confining charged particles.

1.4 The MAST and MAST-U Tokamaks

MAST (short for the **M**ega **A**mpere **S**pherical **T**okamak) is a medium-sized spherical tokamak (ST) based at Culham Centre for Fusion Energy (CCFE). The concept of the spherical tokamak was initially proposed by Peng and Strickler in 1986 [16]. STs have low aspect ratio compared to conventional tokamaks, such as ASDEX Upgrade [17], DIII-D [18], or ITER [6]. Here the aspect ratio A is the ratio of the major to minor radius of the plasma, $A = R/a$. Typically A is less than 2, such as for MAST/MAST Upgrade, $A \sim 0.85 \text{ m}/0.65 \text{ m} \sim 1.33$ [19]; for another medium-sized ST device NSTX/NSTX Upgrade, $A \sim 1.25 - 1.33$ [20]. This means that STs look more like a cored apple than the ring-doughnut shape of a traditional tokamak as shown in Fig. 1.4.

MAST has recently been upgraded to MAST-U and the construction has

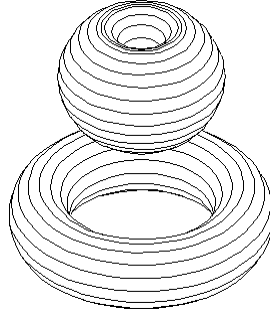


Figure 1.4: Typical configuration of a spherical (up) and conventional (down) tokamak. The spherical tokamak is compact and the aspect ratio $A = R/a$ is normally less than 2 (image taken from [21]).

been completed in 2018. The scientific objectives of MAST-U are to explore the capability of the ST in exhaust, current drive, high beta operation and plasma confinement [19]. Schematic diagrams of MAST and MAST-U are presented in Fig. 1.5. The new device has substantially improved features. These include a super-X divertor configuration [24, 25] which uses expanded magnetic flux configurations and advanced plasma facing materials to handle the high heat flux. Due to the longer connection length and flux expansion the super-X divertor can create significantly reduced target heat fluxes than a regular divertor. Key parameters for MAST and MAST-Upgrade are summarised in Table. 1.1. The external heating system is also improved from 3.8 MW to 5.0 MW and now includes an extra off-axis beam injector [26]. The effect of off-axis heating on stabilising energetic particle modes and reducing anomalous transport has been confirmed on previous MAST experiments and TRANSP simulations [27]. The neutral beam injection is the only auxiliary heat source both on MAST and MAST-U and introduces energetic components into the main confined region of the tokamak. The toroidal magnetic field has also been increased by 50%, and the plasma current and pulse length are increased to 2MA and 5s, respectively.

The ST device is characterised by low requirement for the toroidal field B_t

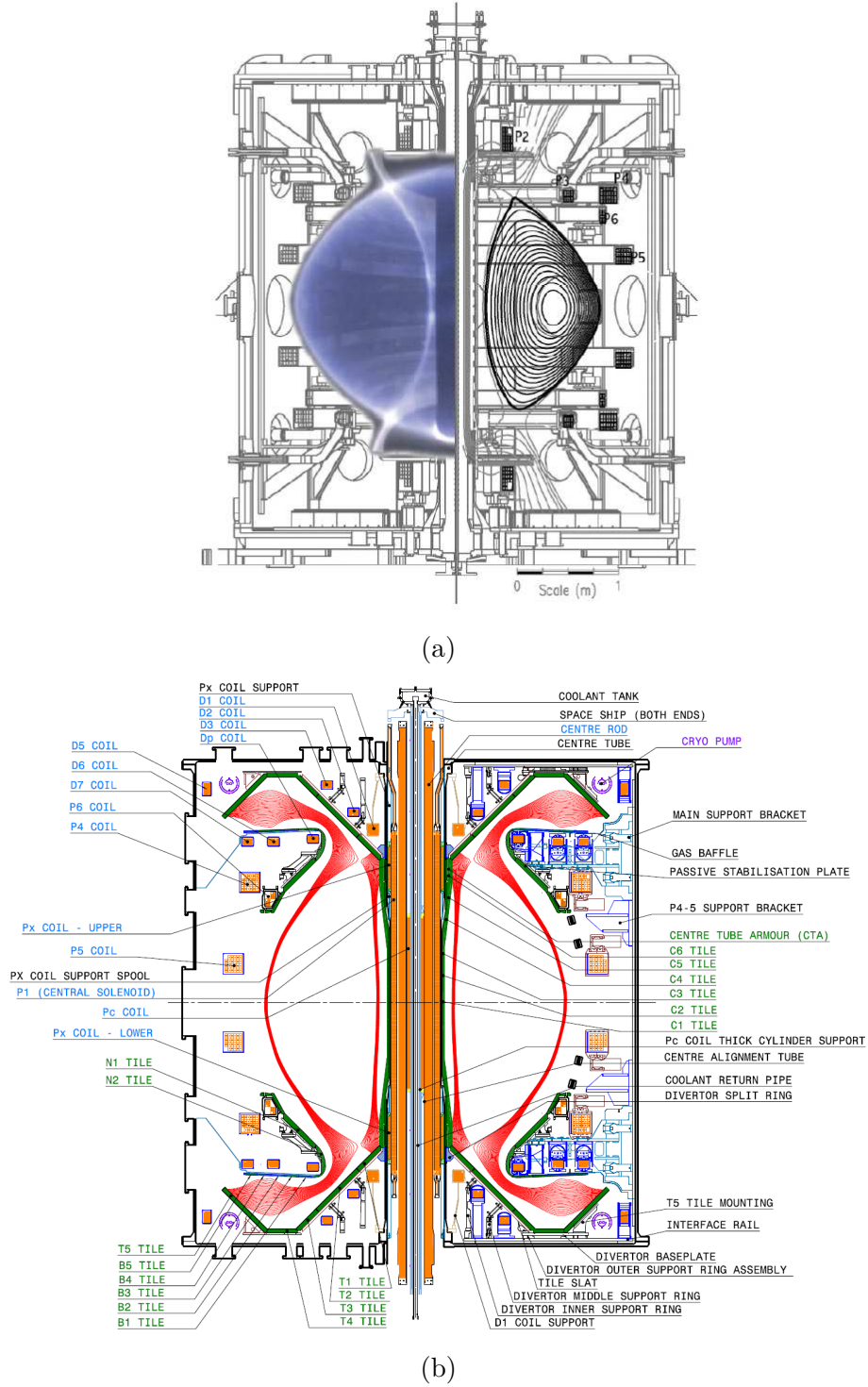


Figure 1.5: Schematic diagrams of (a) MAST [22] and (b) MAST-U [23]. A distinct feature of MAST-U is the super-X divertor configuration indicated by the red solid lines in (b). The edge plasmas and impurities can be diverted to the target plates by following the extended magnetic field lines.

| Parameter | MAST | MAST-U |
|----------------------------------|------|--------|
| Major radius (m) | 0.85 | 0.85 |
| Minor radius (m) | 0.65 | 0.65 |
| Plasma current (MA) | 1.3 | 2.0 |
| Magnetic field at R = 0.85 m (T) | 0.52 | 0.75 |
| Total NBI power (MW) | 3.8 | 5.0 |
| On-axis power | 3.8 | 2.5 |
| Off-axis power | 0 | 2.5 |
| Pulse length | 0.6 | 5 |

Table 1.1: Key parameters for MAST and MAST-Upgrade. The designed size of the plasma in MAST-U remains same as MAST. Operational parameters such the magnetic field and the NBI power are improved by 50% and 25%. The additional off-axis power is expected to alleviate the fast-ion driven instabilities due to a narrow fast ion distribution near the plasma core (table taken from [19]).

and high normalised plasma pressure β , which is the ratio of the plasma pressure to the pressure of the magnetic field required to contain the plasma. The highest toroidal beta of any tokamak has been achieved by START [28], which was the first generation ST built at Culham. The value of beta measures the efficiency of a magnetic thermonuclear reactor confining the plasma so the ST has demonstrated its potential for realising commercial fusion energy. A path to fusion energy with the ST as a candidate for future fusion device has been proposed [29–31]. The UK Atomic Energy Authority (UKAEA) recently embarked upon the STEP (Spherical Tokamak for Energy Production) program to build a Spherical Tokamak power station to put electrical power on the grid by 2040 [32].

1.5 Neutral beam injection

Neutral beam injection (NBI) [33] is an efficient approach for heating plasmas in present tokamaks. The high energy beams are produced via several steps as shown in Fig. 1.6. First, the neutral source gas typically Deuterium is ion-

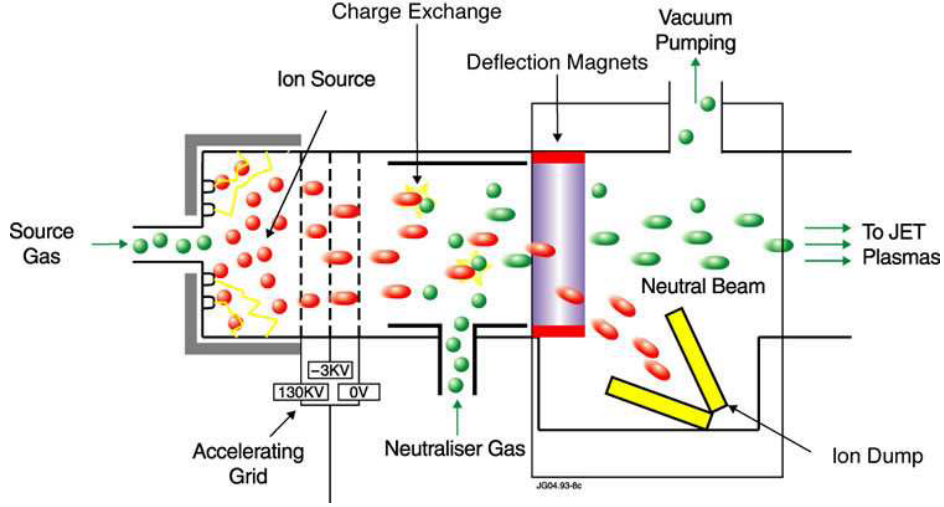


Figure 1.6: A schematic diagram of a JET neutral beam injector. Neutral atoms undergo ionisation, acceleration, neutralisation (and residual ions are collected by deflection magnets and ion dump) before being injected into the plasma (image taken from [34]).

ised, generating positively or negatively charged ions. These charged particles then gain kinetic energy via applied high voltages. After the Deuterium ions are populated and accelerated, they are transferred into a neutraliser unit which is filled with neutral gas. The neutralised particles are not affected by the electromagnetic field in the tokamak and can rapidly deposit at desirable locations, such as the plasma core where a large beam energy is always required. An ion dump unit is installed to collect charged particles after the neutraliser so only the neutral beam is injected into the tokamak. The background plasmas are then heated via Coulomb collisions with the injected particles after the injected particles are ionised.

For large fusion devices, such as JT-60SA or ITER, high beam energy is required to drive the current and heat the plasma and a negative ion source is used. This is due to the fact that negatively charged Deuterium ions more easily lose their electrons and become neutral during neutralisation at high energies so the efficiency η is higher, where η is defined by the ratio of the

beam power to the input power. However, the technique of producing negative ions is much more challenging. This can be understood as it is difficult to attach an electron to the neutral atom compared with losing an electron from the neutral atom during ionisation.

The NBI fast-ion distribution function f can be calculated by solving the Fokker-Planck equation

$$\frac{\partial f}{\partial t} + (\vec{v} \cdot \nabla_{\vec{x}} f + \vec{a} \cdot \nabla_{\vec{v}} f) = \hat{C}(f) + \sigma \quad (1.12)$$

where \vec{v} and \vec{a} are velocity and acceleration of particles. $\hat{C}(f)$ and σ correspond to the collision operator and the source term due to NBI, respectively. Simulation codes such as NUBEAM [35], ASCOT [36] RABBIT [37], or HALO [38] solve this equation using Monte Carlo techniques. A typical solution for f displays three distinct energy peaks corresponding to the full, half and third fraction of the beam injection energy. These energy components come from the ionisation of heavier molecules, i.e. D_2^+ and D_3^+ which are also generated together with D^+ ions. In all cases the energy received by the molecule is the same as they are single charged and gain an energy eV where V is the voltage they accelerate through. In the case of a diatomic or triatomic molecule, this energy is split between two or three Deuterium ions produced when the molecule dissociates in the plasma leading to half and third components. Fig. 1.7 shows a characteristic solution of the fast ion distribution function [37]. In this model, collisions between fast ions are neglected. The half and third energy components of the NBI appear to merge together, and the background plasma ions cause slowing down which smears the peaks downwards in energy.

The NBI system on MAST has undergone several upgrades [39–41]. It is equipped with two positive ion injectors (PINIs), denoted by the south-south

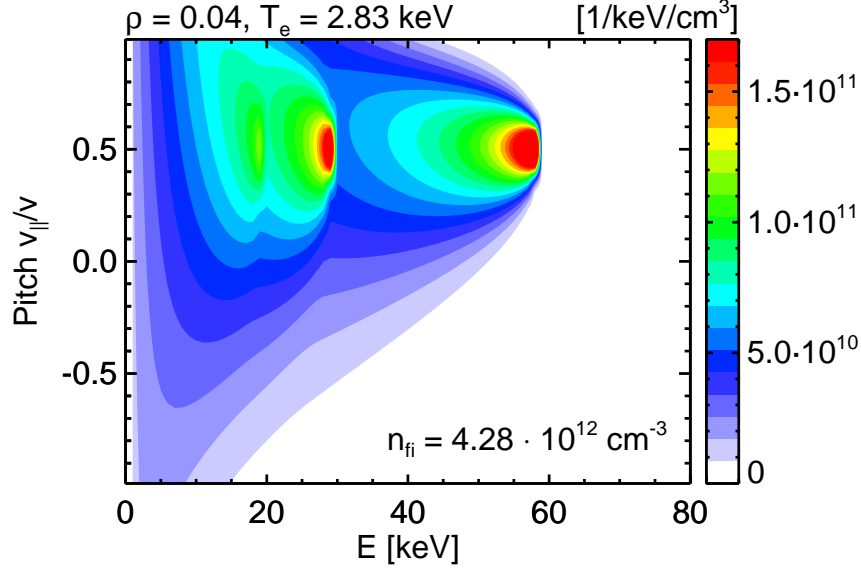


Figure 1.7: A numerical solution of the fast ion distribution shows the full and half energy components of the NBI on ASDEX Upgrade. The third and half energy merge together as the background plasma ions slow down and smears the third peak in energy (image taken from [37]).

(SS) beam and the south-west (SW) beam, and can deliver long pulses for a duration of up to 5 seconds. Each injector can operate with a beam power of up to 2.5 MW at 70 keV [42]. Fast data acquisition and real time control of the beam current are implemented so that the beam power can be conditioned as required [43]. The injected neutral beam changes the particle distribution function, adding a “bump-on tail” at the high energy region. The gradient in the particle distribution could drive a series of MHD instabilities [44].

1.6 Diagnostics

MAST has a wide range of plasma diagnostic systems. In this section, only the key diagnostics used to measure fast-ion driven modes are described. We start with an overview of the Mirnov coil system, which is an important tool for identifying and analysing MHD activity.

1.6.1 Mirnov coil array

The Mirnov coil array measures the current induced by the varying magnetic components perpendicular to the coil circuits, providing a direct observation of the electromagnetic behaviours. It is located just above the mid-plane on the low-field side and at $R = 1.7$ m, approximately 30 cm away from the plasma edge. Nine sets of coils are installed at different toroidal locations and each set consists of three concentric orthogonal coils for measuring three dimensional fluctuations [45]. The measured signals at various locations are analysed in spectrograms where both temporal and spatial Fourier decomposition are applied [46],

$$x_k = \frac{1}{2\pi} \int e^{-j\omega t} F_k d\omega \quad (1.13)$$

$$= \frac{1}{2\pi} \int e^{-j\omega t} \sum_{i=1}^M \alpha_i(\omega) e^{jn_i\phi_k} d\omega \quad (1.14)$$

where x_k is the signal from the k th coil at toroidal location ϕ_k . F_k is the temporal Fourier transform of x_k at angular frequency ω . α_i is the complex amplitude of each toroidal eigenmode n_i . M is the total number of toroidal modes of the plasma. The Mirnov coil array on MAST has a high resolution allowing electromagnetic fluctuations at frequencies from 10 kHz up to several megahertz to be detected. A typical spectrogram is shown in Fig. 1.8 which demonstrates an example of the Fourier decomposition of the magnetic perturbation measured by the outboard Mirnov array for a MAST discharge.

1.7 Fast ions

As discussed in section 1.2, plasmas need to be heated to maintain a preferential reaction temperature ($T_i \sim 15$ keV) so that the thermal conduction and

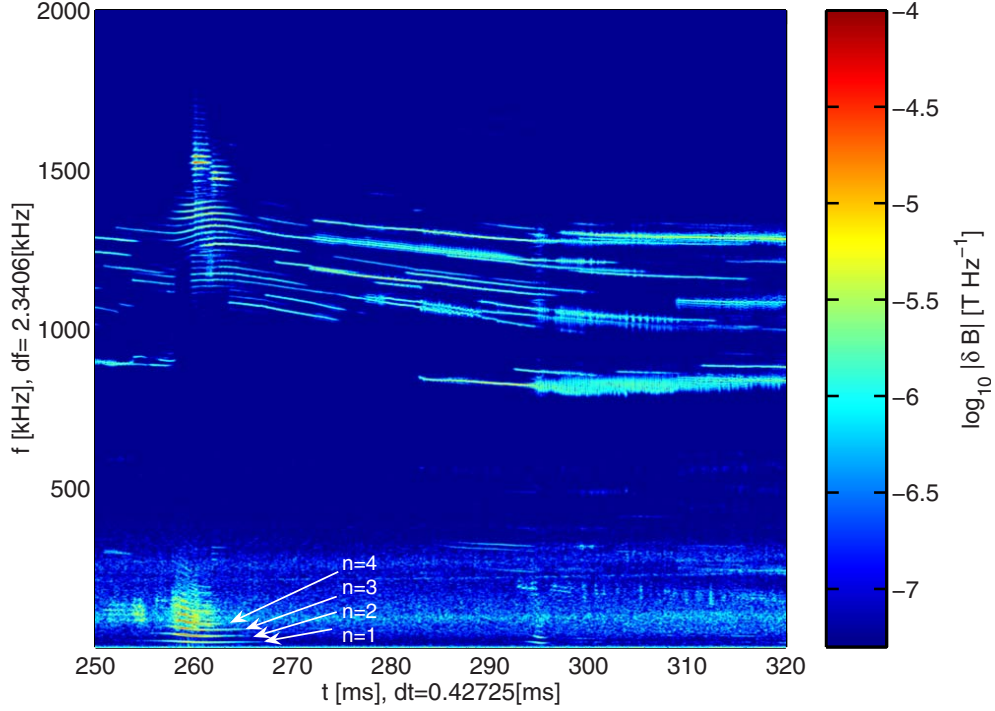


Figure 1.8: A typical magnetic spectrogram of MAST discharge for shot #17944. The colour on the 2D graph shows the amplitude of the magnetic perturbation and dominant harmonics with toroidal mode number $n = 1 \sim 4$ are identified [47].

radiation losses can be compensated or overcome. This cannot only rely on auxiliary heat because it is difficult and expensive to heat plasmas up to this temperature. Therefore, the energy released from the D-T fusion product α particles with an energy of 3.5 MeV should be exploited as much as possible in order to achieve the power balance and self-sustained burning. On the other hand, for plasmas without significant D-T reactions, the study of fast ions can be undertaken by exploiting the development of plasma auxiliary heating techniques. Fast ions can be generated by NBI and radio frequency wave heating. Various mechanisms generate fast particle populations with energies significantly larger than the bulk plasma energy and typically non-Maxwellian distributions [48]. The energy and spatial gradients of the fast ion distributions act as a source of free energy and can drive plasma unstable.

Experimentally, we observe a plethora of different waves and instabilities with different frequencies, mode numbers and spatial structures while the heating system is active [49]. These modes, once excited, can cause redistribution and potentially loss of the driving fast particles. This can result in deleterious effects such as loss of heating efficiency and wall damage [50–52]. Given the above it is essential that we understand the interaction of fast particle populations and waves in plasmas in order to confidently design safe reactor scenarios.

Some of these MHD events are recognised as Alfvén eigenmodes (AEs) [53]. AEs can be driven by the radial pressure gradient of energetic particles that have enough energy to resonate with Alfvén waves. Alfvén waves were first theoretically predicted by H. Alfvén in 1942 when he studied the motion of a conducting liquid in a constant magnetic field by combining the properties of the electromagnetic field and hydrodynamics [54]. These waves propagate along the direction of the magnetic field with a phase velocity $v_A = B/\sqrt{4\pi\rho}$ where ρ is the mass density of the fluid. The wave frequency satisfies a dispersion relation given by $\omega = v_A k_{\parallel}$ where k_{\parallel} is the parallel wave number along the field. For a cylindrical and spatially inhomogeneous plasma, $v_A(r)$ and $k_{\parallel}(r)$ are a function only of the position r . The dispersion relation $\omega^2 = \omega_A^2 = k_{\parallel}^2(r)v_A^2(r)$ displays a continuous spectrum as shown in Fig. 1.9 (a), where three poloidal harmonics with mode number $|m| = 1 - 3$ are completely independent in a cylinder. The Alfvén continuum is stable and difficult to excite as the particle energy is usually not high enough to overcome continuum damping [53]. Also the angular velocity is a function of radius and consequently the waves undergo strong shearing which results in damping.

In a tokamak configuration, the toroidicity breaks the poloidal symmetry

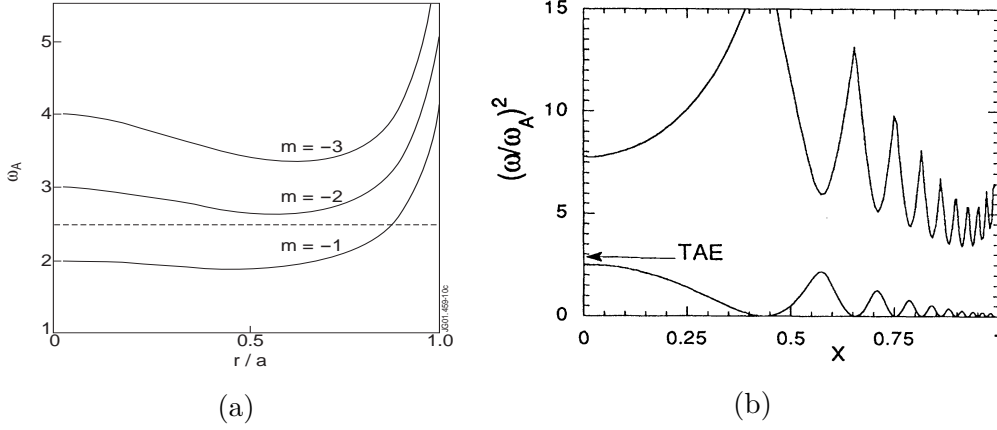


Figure 1.9: (a) Dispersion relation of three waves with poloidal harmonics of $m = -1 \sim -3$ in a cylindrical plasma with current and plasma density gradient [55]; (b) Radial structure of TAE continuum in TFTR for $n = 3$. Here, x is the minor radius (image taken from [56]).

which results in the coupling of different poloidal mode components. Alfvén eigenmodes exist in the gaps of the continuum due to the coupling of two neighbouring branches of shear Alfvén waves with poloidal number m and $m+1$, $\omega = k_{\parallel m} v_A = -k_{\parallel m+1} v_A$. Fig. 1.9 (b) shows a typical Alfvén continuum computed for a TFTR tokamak discharge, together with a discrete eigenfrequency for the toroidal Alfvén eigenmode (TAE). The mode has perturbed electric $\delta \mathbf{E}_{\perp}$ and magnetic $\delta \mathbf{B}_{\perp}$ components perpendicular to the equilibrium magnetic field. Most of the magnitude of a TAE with mode numbers m and n is peaked in the vicinity of the rational surface with safety factor given by $q = (m+1/2)/n$ and corresponding frequency is $\omega_{TAE} = k_{\parallel} v_A = v_A/2qR$ [55].

Significant efforts have been made to develop techniques to diagnose fast-ion driven modes. The radial mode structure in plasma core can be determined by internal plasma measurements with soft x-ray diagnostics [58] or electron cyclotron emission (ECE). The magnetic perturbations are obtained by means of cross-correlation analysis with the measurements of the electron temperature. Both the temperature via ECE and density perturb-

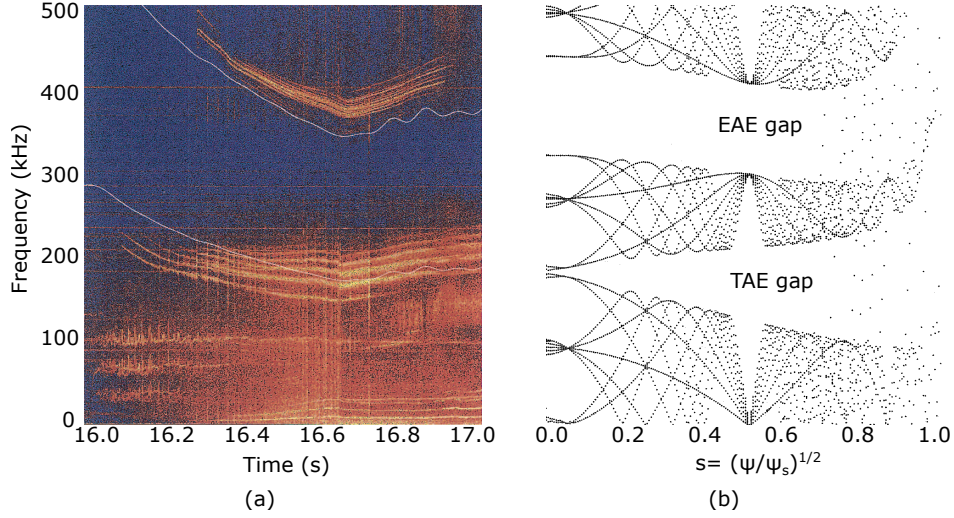


Figure 1.10: Magnetic spectrogram of Alfvénic activities excited by ICRH in JET plasmas [57]. The TAE gap is in approximately 200 kHz while the mode frequency of the elliptic Alfvénic eigenmode (EAE) is about twice ω_{TAE} . Here, s can be approximated by $s \approx r/a$.

ations using beam spectroscopy are found to be closely consistent with the predictions obtained in ideal MHD simulations [59]. The measurements of magnetic perturbations can be performed using a set of high-resolution magnetic pick-up coils. The external magnetic diagnostic coils are capable of detecting perturbations at frequencies from 10 kHz up to several megahertz. Experimental observations have shown that the typical mode frequency of TAEs is 100 ~ 200 kHz. The poloidal and toroidal harmonics are analysed using Fourier decomposition. Fig. 1.10 (a) is a spectrum showing the TAE bursts with toroidal mode number $|n| = 1 - 3$ [57].

In addition, the energetic population could also destabilise other MHD modes, known as “energetic particle modes” (EPM) [60]. These modes are not supported by the bulk plasmas and could exist outside the TAE gap. In MAST discharges, it can be observed that TAEs develop into EPM with beam injections [61, 62]. These EPMs are sometimes referred to as “fishbones” due to their appearance in the spectrogram.

1.8 Outline

Fast-ion driven instabilities have been observed on various fusion devices [53, 63, 64]. In MAST, TAE and fishbone modes with chirping frequencies are excited as the energetic neutral beams are injected into plasmas and fast-ion redistribution takes place simultaneously. The work of this thesis investigates these processes using full orbit simulations. Equations of charged particle motions in electromagnetic field, along with the MHD description for plasmas and a kinetic-MHD model are reviewed in Chapter 2. Based on the hybrid model, a wave-particle resonance condition which is a function of particle motion frequencies and wave frequency is derived. In Chapter 3, a particle pushing code is developed to calculate particle full orbit confined by a 2-dimensional tokamak magnetic field and the orbital frequencies in poloidal and toroidal directions as it is orbiting around the tokamak. In Chapter 4, a plasma discharge in MAST is investigated where TAE and fishbone modes with chirping frequencies are driven and fast ion redistribution is observed as the energetic neutral beams are injected into plasmas. Chapter 5 discusses the HALO model and the simulation of fast ion redistribution induced by the TAE modes using this model. In Chapter 6, these results are summarised and future work is outlined.

Theoretical review

Much of the work of this thesis is concerned with the interaction of fast particle populations with magnetohydrodynamic waves in plasmas. To understand such interactions, it is necessary to first understand the basic behaviour of charged particles in electromagnetic fields and the ideal MHD stability of plasmas in confining magnetic fields. This chapter firstly explores the motion of charged particles in electromagnetic fields. The single particle description neglects the interaction between charged particles, and the motion is determined by Newton's equations of motion and given initial conditions of positions and velocities. This approximation can give intuitive physics pictures of charged particle trajectories in some complicated fields and explain many features of plasmas. It is also the starting point for understanding the magnetic confinement of plasmas. Then the second section describes magnetohydrodynamics in which a plasma is considered as a conductive fluid. It combines classical fluid dynamics and electrodynamics and focuses on the collective behaviours of a plasma rather than the single particle motion. The MHD description is often used to study the macroscopic properties of a plasma, such as the macroscopic equilibrium, stability and many kinds of wave oscillation phenomena. Furthermore, Landau damping [65] is

discussed in one dimension. This explains how energy is exchanged between an electromagnetic wave and particles in the plasma. Lastly, the MHD-kinetic hybrid model [66] based on guiding centre approximation is reviewed. The derivation leads to an important and useful formula, known as the condition of wave-particle resonance. As will be shown in the next chapter, a code has been developed to identify the resonant particles confined by an equilibrium field based on this resonance condition.

2.1 Charged particle motion in magnetically confined devices

2.1.1 Gyro motion

The motion of a particle of charge q and mass m in an electromagnetic field is governed by the equation [2]

$$m \frac{d\mathbf{v}}{dt} = q(\mathbf{v} \times \mathbf{B} + \mathbf{E}). \quad (2.1)$$

For a straight and constant magnetic field $\mathbf{B} = B\hat{\mathbf{z}}$, Eq. (2.1) reduces to

$$\begin{cases} \dot{v}_x = qv_y B/m, \\ \dot{v}_y = -qv_x B/m, \\ \dot{v}_z = 0. \end{cases} \quad (2.2)$$

By defining gyro frequency $\omega_c = |q|B/m$, the solutions of the motion equations are

$$\begin{cases} x = (v_\perp/\omega_c) \sin(\omega_c t + \alpha) + x_0, \\ y = (v_\perp/\omega_c) \cos(\omega_c t + \alpha) + y_0, \\ z = v_\parallel t + z_0, \end{cases} \quad (2.3)$$

where $x_0, y_0, z_0, v_\perp, v_\parallel$ and α are determined by initial conditions. v_\parallel and v_\perp denote the velocity components parallel and perpendicular to the magnetic field. The particle trajectory in the plane perpendicular to the magnetic field satisfies the circular equation

$$(x - x_0)^2 + (y - y_0)^2 = r_c^2, \quad (2.4)$$

where $r_c = v_\perp / \omega_c$ is the gyro radius or Larmor radius. This is the radius of gyro motion as the particle rotates around the centre of the orbit (x_0, y_0) . The centre of the gyro-orbit is referred to as the guiding centre, measuring the average location during a gyro-period $2\pi / \omega_c$. The gyro motion of a charged particle circulating around the field line is the fundamental movement in a magnetic confinement device.

2.1.2 $\mathbf{E} \times \mathbf{B}$ drift

In a magnetic confined plasma, the magnetic field is not straight and constant, so an analytic solution for the particle motion cannot in general be found. However, the dominant motion is still the cyclotron motion perpendicular to the magnetic field line but with a set of superimposed drifts when the variation of the field is small in time and space. The addition of a finite electric field causes a drift both perpendicular to \mathbf{E} and \mathbf{B} , known as $\mathbf{E} \times \mathbf{B}$ drift. The drift velocity is written as

$$\mathbf{v}_E = \frac{\mathbf{E} \times \mathbf{B}}{B^2}. \quad (2.5)$$

For the case of a positively charged particle, the electric field accelerates the motion of the particle when $\mathbf{E} \cdot \mathbf{v}_\perp > 0$ and slows down the particle when $\mathbf{E} \cdot \mathbf{v}_\perp < 0$ as the particle attempts to complete each circular gyro-motion. The acceleration leads to an increasing \mathbf{v}_\perp and therefore larger gyro radius \mathbf{r}_c

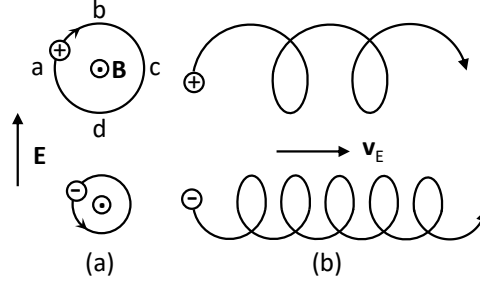


Figure 2.1: (a) Transverse motions of charged particles in a constant magnetic field; (b) Drift motion in the presence of a small \mathbf{E} field. The positive charge accelerates at the left-half circle and its velocity reaches a maximum value at the top of the circle, point b ; it decelerates at the right-half circle and reaches a minimum velocity at the bottom of the circle, point d . The gyro radius increases as the particle moves upwards from $d \rightarrow b$ and decreases as it moves downwards from $b \rightarrow d$. The particle trajectory cannot be closed and the particle drifts with a velocity \mathbf{v}_E .

since $\mathbf{r}_c \sim \mathbf{v}_\perp/B$ while the deceleration reduces \mathbf{r}_c . Over a gyro-period, the guiding centre of the gyro-motion overall drifts away from its original location without the electric field. The drift due to an arbitrary force \mathbf{F} applied to the particle can be found via the substitution $\mathbf{E} \rightarrow \mathbf{F}/q$ and is given by

$$\mathbf{v}_D = \frac{\mathbf{F} \times \mathbf{B}}{qB^2}. \quad (2.6)$$

2.1.3 ∇B drift

A charged particle immersed in a non-uniform magnetic field experiences a mirror force if the field strength varies along the particle trajectory. When the magnetic magnitude varies only slightly over the length scale of the Larmor radius, $r_c \nabla B/B \ll 1$, the ∇B drift velocity can be evaluated by

$$\mathbf{v}_{\nabla B} = \frac{W_\perp}{qB^3} \mathbf{B} \times \nabla B, \quad (2.7)$$

where $W_\perp = mv_\perp^2/2$ is the perpendicular kinetic energy. $\mathbf{v}_{\nabla B}$ is often expressed in terms of the magnetic moment $\mu = W_\perp/B$,

$$\mathbf{v}_{\nabla B} = \frac{(-\mu \nabla B) \times \mathbf{B}}{qB^2}, \quad (2.8)$$

where $\mathbf{F} = -\mu\nabla B$ is the mirror force. The force is in the direction of $-\nabla B$, implying a repulsive force from the region where B field is higher to the region of lower B field.

2.1.4 Curvature drift

A closed and toroidal magnetic field is used to confine fusion plasmas in order to avoid end losses. The field line is hence not straight and can be characterised by the radius of curvature vector \mathbf{R}_c . When the field line is slightly bent, i.e. $R_c \gg r_c$, the motion of a charged particle can be considered as an addition of the guiding centre drift and the gyro-motion. The guiding centre curvature drift velocity is given by

$$\mathbf{v}_\kappa = \frac{mv_\parallel^2}{qB^2R_c^2}\mathbf{R}_c \times \mathbf{B} = \frac{\mathbf{F} \times \mathbf{B}}{qB^2}, \quad (2.9)$$

where $\mathbf{R}_c/R_c^2 = -\mathbf{b} \cdot \nabla \mathbf{b}$ and \mathbf{b} is the unit vector of the magnetic field. $\mathbf{F} = mv_\parallel^2\mathbf{R}_c/R_c$ is the centrifugal force felt by the guiding centre due to the curved B field.

2.1.5 Constants of motion

Along the particle trajectory, several quantities are conserved and can be derived from Eq. (2.1). First, a general energy conservation relation can be found by forming the dot product of the motion equation (2.1) with \mathbf{v} . This leads to

$$\begin{aligned} m\mathbf{v} \cdot \frac{d\mathbf{v}}{dt} &= q\mathbf{E} \cdot \mathbf{v}, \\ \frac{d}{dt} \left(\frac{1}{2}m\mathbf{v}^2 \right) &= -q\nabla\Phi \cdot \mathbf{v} = -q\frac{d\Phi}{dt}, \\ \frac{1}{2}mv^2 + q\Phi &= \text{constant}. \end{aligned} \quad (2.10)$$

where the electromagnetic field is assumed to be static. It is hence expressed as the gradient of the scalar potential $\mathbf{E} = -\nabla\Phi$. The conclusion is that

the sum of kinetic and potential energy of a charged particle in a static electromagnetic field is constant. The kinetic energy is conserved when $\mathbf{E} = 0$ indicating that the magnetic field does no work on a charged particle.

The second conservation relation is the canonical toroidal momentum under the condition of toroidal symmetry. The Lagrangian of a charged particle in the conservative field is given by [67]

$$\mathcal{L}(\mathbf{x}, \dot{\mathbf{x}}, t) = \frac{1}{2}m\dot{\mathbf{x}}^2 - q\Phi(\mathbf{x}, t) + q\dot{\mathbf{x}} \cdot \mathbf{A}, \quad (2.11)$$

where the vector potential \mathbf{A} is defined by $\mathbf{B} = \nabla \times \mathbf{A}$. The Lagrangian \mathcal{L} , expressed in terms of canonical coordinates (R, ϕ, Z) , is written as

$$\mathcal{L}(R, \phi, Z, \dot{R}, \dot{\phi}, \dot{Z}, t) = \frac{1}{2}m(\dot{R}^2 + \dot{Z}^2 + R^2\dot{\phi}^2) + q(\dot{R}A_R + \dot{Z}A_Z + R\dot{\phi}A_\phi - \Phi). \quad (2.12)$$

Substituting $\mathcal{L}(R, \phi, Z, \dot{R}, \dot{\phi}, \dot{Z}, t)$ into the Lagrange equation of motion and considering only the ϕ equation

$$\begin{aligned} \frac{d}{dt} \left(\frac{\partial \mathcal{L}}{\partial \dot{\phi}} \right) - \frac{\partial \mathcal{L}}{\partial \phi} &= 0, \\ \frac{d}{dt} (mR^2\dot{\phi} + qRA_\phi) &= 0, \\ P_\phi \equiv mR^2\dot{\phi} + qRA_\phi &= \text{constant}. \end{aligned} \quad (2.13)$$

The canonical toroidal momentum P_ϕ is a constant due to the toroidal symmetry $\partial \mathcal{L} / \partial \phi = 0$. The second term in P_ϕ can be expressed in terms of the poloidal magnetic flux $\psi_p = 2\pi RA_\phi$, leading to $P_\phi = mR^2\dot{\phi} + q\psi_p/2\pi$.

The third invariant of interest is the magnetic moment $\mu = mv_\perp^2/2B$. The magnetic moment is an adiabatic invariant, which is conserved if the magnetic field varies only slightly over the the scale of the gyro radius. The motion of the guiding centre along the \mathbf{B} field is dominated by the mirror force,

$$m \frac{dv_\parallel}{dt} = -\mu \nabla_\parallel B \quad (2.14)$$

Multiplying (2.14) by $v_{\parallel} = ds/dt$ yields

$$\frac{d}{dt} \left(\frac{1}{2} m v_{\parallel}^2 \right) = -\mu \frac{ds}{dt} \frac{dB}{ds}. \quad (2.15)$$

Using energy conservation

$$\frac{d}{dt} \left(\frac{1}{2} m v_{\parallel}^2 + \frac{1}{2} m v_{\perp}^2 \right) = 0, \quad (2.16)$$

we have

$$\begin{aligned} \frac{d}{dt} \left(\frac{1}{2} m v_{\perp}^2 \right) &= \mu \frac{dB}{dt}, \\ \frac{d}{dt} (\mu B) &= \mu \frac{dB}{dt}, \\ B \frac{d\mu}{dt} &= 0. \end{aligned} \quad (2.17)$$

This shows that μ is a constant in time since B is non-zero.

The consequence of μ being a constant of motion is that when a charged particle is moving in a non-uniform magnetic field, the particle perpendicular kinetic energy is changing with B field in order to maintain the value of μ as $\mu = W_{\perp}/B$ by definition. Hence the parallel energy might reduce to zero as B grows and then the parallel motion is reversed. The guiding centre can therefore be trapped between two strong magnetic field locations. This is known as the bounce motion of the guiding centre.

2.2 Magnetohydrodynamics

Magnetohydrodynamics (MHD) is a way to describe the collective behaviours of plasmas in an electromagnetic field. The plasmas are divided into many small fluid elements which still contain relatively large numbers of ions and electrons, denoted by plasma density n ,

$$n_{\alpha}(\mathbf{r}, t) = \int f_{\alpha}(\mathbf{r}, \mathbf{v}, t) d\mathbf{v}. \quad (2.18)$$

where $f_\alpha(\mathbf{r}, \mathbf{v}, t)$ is the particle distribution function for each species α and it is normally a function of spatial position, velocity and time. The fluid velocity \mathbf{u} is the average velocity over the total number of particles within the fluid element,

$$\mathbf{u}_\alpha(\mathbf{r}, t) = \frac{1}{n} \int \mathbf{v} f_\alpha(\mathbf{r}, \mathbf{v}, t) d\mathbf{v} = \langle \mathbf{v} \rangle. \quad (2.19)$$

with $\langle \dots \rangle$ denoting the average over velocity space.

The total pressure tensor has nine elements given by

$$\begin{aligned} \mathbf{P} &= n_\alpha m_\alpha \langle \mathbf{v} \mathbf{v} \rangle = n_\alpha m_\alpha \mathbf{u}_\alpha \mathbf{u}_\alpha + n_\alpha m_\alpha \langle \mathbf{w} \mathbf{w} \rangle \\ \mathbf{P} &= n_\alpha m_\alpha \mathbf{u}_\alpha \mathbf{u}_\alpha + \mathbf{p}_\alpha + \pi_\alpha \end{aligned} \quad (2.20)$$

Here, $\mathbf{w} = \mathbf{v} - \mathbf{u}_\alpha$ is the random component of the particle velocity. \mathbf{p}_α and π_α represent the diagonal and off-diagonal terms of the pressure tensor, respectively. When the coordinate is rotated along the field line and the remaining two coordinates are chosen to be perpendicular to the magnetic field, the three dependent scalar pressure components can be written as

$$\mathbf{p}_\alpha = \begin{bmatrix} p_\perp & & \\ & p_\perp & \\ & & p_\parallel \end{bmatrix}. \quad (2.21)$$

When a local thermodynamic equilibrium state is achieved, the MHD equilibrium pressure is isotropic: $p_\perp = p_\parallel = p$ and the temperature is $T = p/n$. For an anisotropic system, $p_\perp \neq p_\parallel$, $\mathbf{p}_\alpha = p_\perp(\mathbf{I} - \mathbf{b}\mathbf{b}) + p_\parallel \mathbf{b}\mathbf{b} = p_\perp \mathbf{I} + (p_\parallel - p_\perp)\mathbf{b}\mathbf{b}$, where \mathbf{I} is the unit tensor and

$$\mathbf{b}\mathbf{b} = \begin{bmatrix} 0 & & \\ & 0 & \\ & & 1 \end{bmatrix}. \quad (2.22)$$

In a plasma, each fluid element is composed of fully ionised ions and electrons. As the mass of the ions is greater than the mass of the electrons,

i.e., $m_i \gg m_e$, we can simply neglect electron mass and hence the mass density can be written as $\rho = nm_i$, where $n_i = n_e \equiv n$ because of quasi-neutrality. In addition, the momentum of the fluid is also predominantly carried by ions so the fluid velocity is defined by $\mathbf{u} = \mathbf{u}_i$. The current density is determined by the difference of the flow velocity of ions and electrons $\mathbf{j} = en(\mathbf{u}_i - \mathbf{u}_e)$. The total pressure is simply the contributions of both species: $p = p_i + p_e = 2nT$ and $T = (T_i + T_e)/2$. One special situation is when the ions have the same temperature as the electrons, $T_i = T_e = T$, the expression of the pressure then reduces to $p = nT$.

The resulting MHD equation set are conservative relations of mass, momentum and energy coupled with Maxwell's equations:

$$\frac{\partial \rho}{\partial t} + \nabla \cdot (\rho \mathbf{u}) = 0 \quad \text{Mass continuity} \quad (2.23)$$

$$\rho \frac{d\mathbf{u}}{dt} + \nabla p - \mathbf{j} \times \mathbf{B} = 0 \quad \text{Momentum balance} \quad (2.24)$$

$$\frac{d}{dt} \left(\frac{p}{\rho^\gamma} \right) = 0 \quad \text{Adiabatic equation of state} \quad (2.25)$$

$$\mathbf{E} + \mathbf{u} \times \mathbf{B} = 0 \quad \text{Ohm's law} \quad (2.26)$$

$$\nabla \cdot \mathbf{E} = 0 \quad \text{Gauss's law} \quad (2.27)$$

$$\nabla \times \mathbf{E} + \frac{\partial \mathbf{B}}{\partial t} = 0 \quad \text{Faraday's Law} \quad (2.28)$$

$$\nabla \times \mathbf{B} - \mu_0 \mathbf{j} = 0 \quad \text{Ampere's Law} \quad (2.29)$$

$$\nabla \cdot \mathbf{B} = 0 \quad \text{No magnetic monopoles} \quad (2.30)$$

where the convective derivative is given by

$$\frac{d}{dt} = \frac{\partial}{\partial t} + \mathbf{u} \cdot \nabla. \quad (2.31)$$

In these equations, the fluid variables are the mass density ρ , the fluid velocity \mathbf{u} and the pressure p . $\gamma = 5/3$ is the ratio of specific heats. The electromagnetic variables are the electric field \mathbf{E} , the magnetic field \mathbf{B} , and the current

density \mathbf{j} . μ_0 is the permeability of free space. We have assumed that the plasma is a perfect conductor in Ohm's law, that is, the electrical conductivity is infinite, $\sigma_c \rightarrow \infty$. This is widely true for fusion plasmas as σ_c increases with the plasma temperature T : $\sigma_c \propto T^{3/2}$. This set of MHD equations is also known as ideal MHD equations because of the perfect conductivity assumption of Ohm's law.

Due to the assumptions made in deriving the MHD equations, they are valid for describing processes on temporal and spatial scales which obey the following relations [68],

$$\lambda_{\perp} \gg r_c, \quad (2.32)$$

$$\lambda_{\parallel} \gg \lambda_c, \quad (2.33)$$

$$\tau \gg \tau_c, \quad (2.34)$$

where the characteristic time scale is τ . The perpendicular and parallel length scales are denoted by λ_{\perp} and λ_{\parallel} , respectively. r_c is the gyro radii, λ_c the mean free path of a particle and τ_c the typical collision time.

2.3 Equilibrium

An MHD equilibrium is achieved when the plasma state is independent of time, that is, $d\mathbf{u}/dt = 0$ in the momentum conservation equation

$$\rho \frac{d\mathbf{u}}{dt} + \nabla p - \mathbf{j} \times \mathbf{B} = 0. \quad (2.24)$$

Then the equilibrium condition is given by

$$\mathbf{j} \times \mathbf{B} = \nabla p, \quad (2.35)$$

where the magnetic force $\mathbf{j} \times \mathbf{B}$ is balanced by the pressure gradient force ∇p . The magnetic force can also be written as

$$\mathbf{j} \times \mathbf{B} = \frac{1}{\mu_0} (\nabla \times \mathbf{B}) \times \mathbf{B} = \nabla \cdot \mathbf{T}. \quad (2.36)$$

Here, the stress tensor \mathbf{T} is given by

$$\mathbf{T} = \frac{1}{\mu_0} (\mathbf{B}\mathbf{B} - \frac{1}{2} B^2 \mathbf{I}) \quad (2.37)$$

where \mathbf{I} is the unit stress. The force balance equation (2.35) becomes

$$-\nabla p + \mathbf{j} \times \mathbf{B} = \nabla \cdot (\mathbf{T} - p\mathbf{I}), \quad (2.38)$$

and

$$\mathbf{T} - p\mathbf{I} = -(p + B^2/2\mu_0)\mathbf{I} + \mathbf{B}\mathbf{B}/\mu_0. \quad (2.39)$$

The normal component of the total stress is $(\mathbf{T} - p\mathbf{I}) \cdot \mathbf{n} = -(p + B^2/2\mu_0)\mathbf{n} + (\mathbf{B} \cdot \mathbf{n})\mathbf{B}/\mu_0$, which implies that the total stress is a combination of the plasma pressure p , magnetic pressure $B^2/2\mu_0$ and the magnetic tension B^2/μ_0 along the field line driven by the curvature of the field lines. The quantity $\beta = 2p/\mu_0 B^2$ evaluated by the ratio of the plasma thermal pressure and the magnetic pressure is often used as an important plasma equilibrium parameter. This factor measures the efficiency of plasma confinement by the magnetic field and a low value of β indicates that a substantial amount of magnetic pressure is used to contain not much thermal pressure.

From Eq. (2.35), it can be easily found that \mathbf{B} , \mathbf{j} and ∇p satisfy the following relations:

$$\mathbf{B} \cdot \nabla p = 0, \quad (2.40)$$

$$\mathbf{j} \cdot \nabla p = 0, \quad (2.41)$$

which imply that both the magnetic field lines and the current lines lie on the contours of constant pressure but the angle between \mathbf{B} and \mathbf{j} is arbitrary

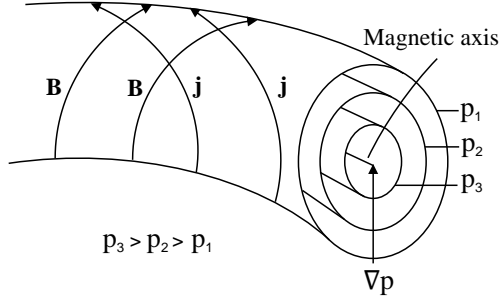


Figure 2.2: Contours of the constant equilibrium pressure are nested toroidal surfaces. Both the magnetic field and the current lines lie on the constant pressure surfaces.

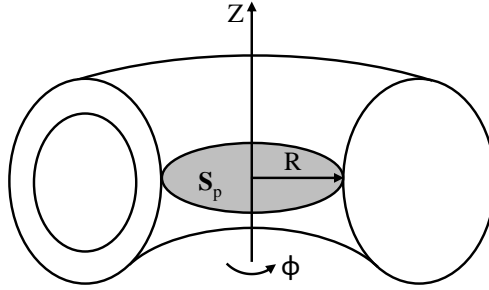


Figure 2.3: Poloidal surface S_p used to calculate the magnetic flux.

as shown in Fig. 2.2. These contours are usually referred to as magnetic flux surfaces or flux surfaces. The limiting situation is that the flux surface degenerates into a single line and the magnetic field line is also on this single line. In such case, the magnetic field is purely in the toroidal direction and this occurs at the magnetic axis in the centre of the device and at the X points in diverted plasmas [23].

The helicity of the magnetic field line on each flux surface is described by the *safety factor* q , defined by $q = 2\pi/\iota$, where ι represents the angle changes in the poloidal plane when the magnetic field line goes around the torus once (the toroidal angle changes 2π). If the magnetic field returns to the starting point after completing n loops around the torus and m loops around the poloidal plane, $q = n/m$ is a rational number and the flux surface is called a rational surface.

A favourable pressure profile in a tokamak is when the plasmas are hot and dense near the centre of the poloidal cross section so that the plasmas are well confined and isolated from the material walls. Hence the contours of constant pressure are nested toroidal surfaces whose the innermost layer corresponds to a maximum pressure. In Fig. 2.2, $p = p_1, p_2, p_3$ label three flux surfaces which are wrapped by the field lines. We can define any surface quantity ψ to be a function of p so that the magnetic field can be easily expressed.

From Eq. (2.40) it follows that $\mathbf{B} \cdot \nabla\psi = 0$ for a system that is orthogonal, implying that if we can choose an orthogonal system with one of the \mathbf{B} components along $\nabla\psi$, then the strength of this component B_ψ would be zero since $B_\psi = \mathbf{B} \cdot \nabla\psi$ by definition. Consequently, the equilibrium degrees of freedom reduce to two when a flux surface coordinate system is used.

A cylindrical right-handed coordinate system is formed by (R, ϕ, Z) as shown in Fig. 2.3. The magnetic field consists of three components: B_R , B_ϕ and B_Z . In a flux surface coordinate system, the magnetic field can be decomposed as $\mathbf{B} = B_\psi \mathbf{e}_\psi + B_\phi \mathbf{e}_\phi + B_p \mathbf{e}_p$, where $B_\psi = 0$. \mathbf{e}_ψ , \mathbf{e}_ϕ , \mathbf{e}_p are a set of local orthogonal unit vectors perpendicular to each other, $\mathbf{e}_\psi = \nabla\psi/|\nabla\psi|$ and \mathbf{e}_p is in the direction of $\nabla\psi \times \mathbf{e}_\phi$.

The axisymmetric assumption implies that $\partial/\partial\phi = 0$. Then $\nabla \cdot \mathbf{B} = 0$ can be written as

$$\frac{1}{R} \frac{\partial}{\partial R}(RB_R) + \frac{\partial B_Z}{\partial Z} = 0. \quad (2.42)$$

The poloidal magnetic field \mathbf{B}_p can be described by a scalar function ψ in

this way so that the the above equation is automatically satisfied:

$$B_R = -\frac{1}{R} \frac{\partial \psi}{\partial Z}, \quad (2.43)$$

$$B_Z = \frac{1}{R} \frac{\partial \psi}{\partial R}, \quad (2.44)$$

$$\mathbf{B}_p = \mathbf{B}_R + \mathbf{B}_Z = \frac{1}{R} \nabla \psi \times \mathbf{e}_\phi. \quad (2.45)$$

Here it is only assumed that $\psi(p)$ is a function of pressure and it has no specific physics significance.

A simple representation of the magnetic field and current can be found by using the poloidal magnetic flux as a coordinate, defined as:

$$\psi_p = \int_{\mathbf{S}_p} \mathbf{B} \cdot d\mathbf{S}_p, \quad (2.46)$$

where \mathbf{S}_p is the poloidal surface as shown in Fig. 2.3. This quantity is defined on a flux surface and so can be considered a monotonic function of p , that is, $\psi_p = \psi_p(p)$. Using Eq. (2.44), the relation between the general ψ function and the flux surface function ψ_p can be found via

$$\psi_p = \int_0^{2\pi} d\phi \int_0^R R B_Z dR = 2\pi \psi. \quad (2.47)$$

Ampere's law in Eq. (2.29) gives the current density $\mathbf{j} = \nabla \times \mathbf{B} / \mu_0$. Here \mathbf{j} can be decomposed as $\mathbf{j} = j_\phi \mathbf{e}_\phi + \mathbf{j}_p$ and $\mathbf{j}_p = j_R \mathbf{e}_R + j_Z \mathbf{e}_Z$ so the components j_ϕ , j_R and j_Z are expressed in terms of the magnetic field components:

$$j_\phi = \frac{1}{\mu_0} \left(\frac{\partial B_R}{\partial Z} - \frac{\partial B_Z}{\partial R} \right) \mathbf{e}_\phi = -\frac{1}{\mu_0 R} \Delta^* \psi, \quad (2.48)$$

$$j_R = -\frac{\partial B_\phi}{\mu_0 \partial Z} = -\frac{1}{\mu_0 R} \frac{\partial F}{\partial Z}, \quad (2.49)$$

$$j_Z = \frac{1}{\mu_0 R} \frac{\partial F}{\partial R}, \quad (2.50)$$

where

$$F = R B_\phi \quad (2.51)$$

and the elliptic operator Δ^* is given by

$$\Delta^* = R \frac{\partial}{\partial R} \left(\frac{1}{R} \frac{\partial}{\partial R} \right) + \frac{\partial^2}{\partial Z^2} = \frac{\partial^2}{\partial R^2} + \frac{\partial^2}{\partial Z^2} - \frac{1}{R} \frac{\partial}{\partial R}. \quad (2.52)$$

The \mathbf{R} component of the MHD equilibrium equation is given by

$$\frac{dp}{dR} = j_\phi B_Z - j_Z B_\phi. \quad (2.53)$$

Substituting Eq. (2.44), (2.48) and (2.50) for B_Z , j_ϕ and j_Z into Eq. (2.53) and using

$$\frac{dp}{dR} = \frac{dp}{d\psi} \frac{d\psi}{dR}, \quad (2.54)$$

the equilibrium equation (2.53) becomes

$$\Delta^* \psi = -\mu_0 R^2 \frac{dp}{d\psi} - \frac{1}{2} \frac{dF^2}{d\psi}, \quad (2.55)$$

where both pressure $p(\psi)$ and $F(\psi) = RB_\phi$ are functions of the flux surface label ψ . Eq. (2.55) is known as the Grad-Shafranov (GS) equation [69, 70], which describes general axisymmetric toroidal equilibria.

The Grad-Shafranov equation describes 2-dimensional MHD equilibrium in a toroidally confined configuration. The physical variables in the equation, such as p and ψ are independent of the toroidal angle, ϕ and yet to be calculated. Experimental measurements are required to provide boundary conditions to solve the equation and obtain valid equilibria. **EFIT/EFIT++** [71] is a numerical code that is designed to solve the Grad-Shafranov equation and has been successful in reconstructing MHD equilibrium profiles of magnetic field and plasma pressure using experimental constraints. The code uses data from magnetic probes and flux loops to give the shape of the magnetic flux surfaces and D_α data to determine the plasma boundary location [72]. On MAST, measurements from the motional stark effect diagnostics [73] are used to constrain the current distribution at a single time point in

each discharge. The electron temperature T_e and density n_e are measured by Thomson scattering system at 29 radial locations across the mid-plane [74]. The ion temperature T_i is inferred from the charge exchange recombination measurements [75]. The equilibrium pressure profile can also be constrained using $n_i T_i + n_e T_e$ and the fast particle contribution to the pressure is omitted. EFIT++ uses a complicated interactive loop to obtain the equilibria. A functional representation, such as polynomials of some order, is chosen for the derivatives $p'(\psi)$ and $FF'(\psi)$ in Eq. (2.55). Then one starts with an initial 'guess' of the plasma shape (flux surfaces) and finds the coefficients for the representations of $p'(\psi)$ and $FF'(\psi)$ which best fit all the data given this current shape. Profiles of $p(\psi)$ and $F(\psi)$ can be calculated and the GS equation is re-solved to obtain a new plasma shape. This process is iterated to convergence. The components of the magnetic field are derived as given in Eq. (2.43), (2.44) and (2.51) after interpolating the values of ψ . Fig. 2.4 is an example of the equilibrium profile for a discharge on MAST reconstructed by EFIT++ [72]. The contours are the normalised poloidal flux function ψ_n which is calculated by

$$\psi_n = \frac{\psi - \psi_{\text{axis}}}{\psi_{\text{wall}} - \psi_{\text{axis}}}, \quad (2.56)$$

where ψ_{axis} and ψ_{wall} are boundary values in the simulation. Therefore ψ_n is in the range $0 \leq \psi_n \leq 1$. $\psi_n = 0$ and $\psi_n = 1$ indicate the locations of the magnetic axis and the last closed flux surface (LCFS), respectively.

2.4 MHD instability

For a given MHD equilibrium, it is necessary to examine whether the equilibrium is MHD stable or not. This is crucial for the experimental operation of a tokamak as massive instabilities could result in the whole plasma hitting the

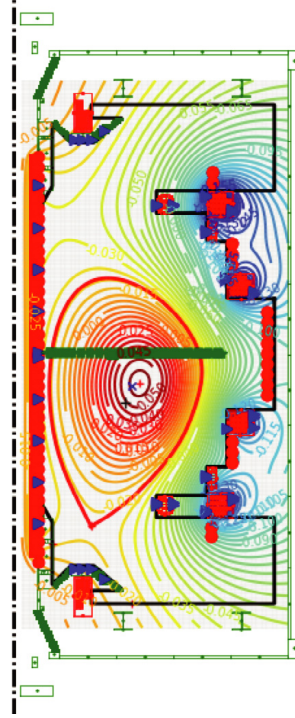


Figure 2.4: A typical MHD equilibrium profile for a MAST discharge reconstructed by EFIT/EFIT++. The LCFS is labelled with red solid line and the magnetic axis is marked with a red cross ‘+’ (taken from [72]).

wall or change the magnetic configuration, enhance particle and energy transport, and ultimately reduce plasma confinement and terminate reactions. In a plasma, either pressure or electromagnetic field could provide a restoring force when there is a small perturbation. If this perturbation only oscillates near its equilibrium position or decays to zero, then the system is considered stable. However, if the amplitude of the perturbation can grow, the system is unstable.

2.4.1 Linearisation

Under a small perturbation, a physical quantity $Q(\mathbf{r}, t)$ can be expanded about its equilibrium value $Q_0(\mathbf{r})$,

$$Q(\mathbf{r}, t) = Q_0(\mathbf{r}) + Q_1(\mathbf{r}, t), \quad (2.57)$$

where Q_0 is time-independent and Q_1 is the first order linear perturbation. Considering an ideal MHD fluid satisfying

$$\begin{aligned}
\frac{\partial \rho}{\partial t} + \nabla \cdot (\rho \mathbf{u}) &= 0, \\
\rho \frac{d\mathbf{u}}{dt} &= -\nabla p + \mathbf{j} \times \mathbf{B}, \\
\nabla \times (\mathbf{u} \times \mathbf{B}) &= \frac{\partial \mathbf{B}}{\partial t}, \\
\nabla \times \mathbf{B} &= \mu_0 \mathbf{j}, \\
p\rho^{-\gamma} &= \text{const.}
\end{aligned} \tag{2.58}$$

The linear expansion formulation is written as

$$\begin{aligned}
\mathbf{B} &= \mathbf{B}_0(\mathbf{r}) + \mathbf{B}_1(\mathbf{r}, t), \\
\rho &= \rho_0(\mathbf{r}) + \rho_1(\mathbf{r}, t), \\
\mathbf{j} &= \mathbf{j}_0(\mathbf{r}) + \mathbf{j}_1(\mathbf{r}, t), \\
p &= p_0(\mathbf{r}) + p_1(\mathbf{r}, t), \\
\mathbf{u} &= \mathbf{u}_1(\mathbf{r}, t).
\end{aligned} \tag{2.59}$$

Here, a static equilibrium plasma with $\mathbf{u}_0 = 0$ is considered. Substituting these expressions into the MHD equations and cancelling all the equilibrium quantities yields

$$\begin{aligned}
\rho_1 &= -\nabla \cdot (\rho_0 \boldsymbol{\xi}), \\
p_1 &= -\boldsymbol{\xi} \cdot \nabla p_0 - \gamma p_0 \nabla \cdot \boldsymbol{\xi}, \\
\mathbf{B}_1 &= \nabla \times (\boldsymbol{\xi} \times \mathbf{B}_0),
\end{aligned} \tag{2.60}$$

where the vector $\boldsymbol{\xi}$ is defined via $\mathbf{u}_1 = \partial \boldsymbol{\xi} / \partial t$ representing the displacement that the plasma is away from its equilibrium position. The momentum equation becomes

$$\rho_0 \frac{\partial^2 \boldsymbol{\xi}}{\partial t^2} = \mathbf{F}(\boldsymbol{\xi}) \tag{2.61}$$

and $\mathbf{F}(\boldsymbol{\xi})$ is the force operator given by

$$\begin{aligned}\mathbf{F}(\boldsymbol{\xi}) &= \mathbf{j}_0 \times \mathbf{B}_1 + \mathbf{j}_1 \times \mathbf{B}_0 - \nabla p_1 \\ &= \frac{1}{\mu_0}(\nabla \times \mathbf{B}_0) \times \mathbf{B}_1 + \frac{1}{\mu_0}(\nabla \times \mathbf{B}_1) \times \mathbf{B}_0 + \nabla(\boldsymbol{\xi} \cdot \nabla p_0 + \gamma p_0 \nabla \cdot \boldsymbol{\xi}).\end{aligned}\tag{2.62}$$

2.4.2 Normal mode formulation

Assume all the perturbed quantities have the form of a normal mode:

$$\tilde{Q}_1(\mathbf{r}, t) = Q_1(\mathbf{r}) \exp(-i\omega t).\tag{2.63}$$

The linearised momentum equation (2.61) can be written as

$$-\omega^2 \rho_0 \boldsymbol{\xi} = \mathbf{F}(\boldsymbol{\xi})\tag{2.64}$$

where \mathbf{F} is given in Eq. (2.62). The force operator \mathbf{F} is self-adjoint, that is, for any two arbitrary vectors $\boldsymbol{\xi}(\mathbf{r})$ and $\boldsymbol{\eta}(\mathbf{r})$ both satisfying eigenfunctions of \mathbf{F} as described by Eq. (2.64), the following relation holds

$$\int \boldsymbol{\eta} \cdot \mathbf{F}(\boldsymbol{\xi}) d\mathbf{r} = \int \boldsymbol{\xi} \cdot \mathbf{F}(\boldsymbol{\eta}) d\mathbf{r}.\tag{2.65}$$

It is straightforward to define the stability of a mode by making use of the self-adjoint property of the force operator. Taking the dot product of $\boldsymbol{\xi}^*$ on Eq. (2.64) and integrating over the entire volume lead to

$$-\omega^2 \int \rho_0 |\boldsymbol{\xi}|^2 d\mathbf{r} = \int \boldsymbol{\xi}^* \cdot \mathbf{F}(\boldsymbol{\xi}) d\mathbf{r},\tag{2.66}$$

with $\boldsymbol{\xi}^*$ being the complex conjugate of $\boldsymbol{\xi}$. Then taking dot product of $\boldsymbol{\xi}$ on the conjugate of Eq. (2.64) and performing the volume integration give

$$-(\omega^2)^* \int \rho_0 |\boldsymbol{\xi}|^2 d\mathbf{r} = \int \boldsymbol{\xi} \cdot \mathbf{F}(\boldsymbol{\xi}^*) d\mathbf{r}.\tag{2.67}$$

\mathbf{F} is self-adjoint implying the right-hand sides of Eq. (2.66) and (2.67) are equal. Then we have $\omega^2 = (\omega^2)^*$ where $(\omega^2)^*$ is the complex conjugate of ω^2 . To conclude, the self-adjointness of \mathbf{F} ensures that ω^2 is purely real.

The stability of a mode can be defined via the mode frequency ω when ω^2 is a real number:

$$\begin{cases} \omega^2 > 0 & \text{oscillatory stability} \\ \omega^2 < 0 & \text{unstable} \end{cases} \quad (2.68)$$

The positive ω^2 implies $\text{Im}(\omega) = 0$ and $\text{Re}(\omega) \neq 0$. This corresponds a stable mode that simply oscillates near its equilibrium position. For a mode with $\omega^2 < 0$, one branch with $\text{Im}(\omega) > 0$ exponentially grows with time and thus is unstable. The stable-unstable transition takes place at $\omega = 0$.

A further consequence of $\mathbf{F}(\boldsymbol{\xi})$ being self-adjoint is that the discrete normal modes are orthogonal to each other,

$$\int \rho_0 \boldsymbol{\xi}_m \cdot \boldsymbol{\xi}_n d\mathbf{r} = \delta_{mn}, \quad (2.69)$$

where $\boldsymbol{\xi}_m$ and $\boldsymbol{\xi}_n$ are two solutions to Eq. (2.64). The orthogonal eigenfunctions can be used to span a linear space and thus any small perturbation of a system can be described by the combination of these basis functions, $\boldsymbol{\xi}(t) = \sum_{n=1}^{\infty} a_n \boldsymbol{\xi}_n \exp(-i\omega_n t)$ with a_n being the expansion coefficient.

2.4.3 Homogeneous plasmas

A perturbed plasma in an infinite homogeneous field can excite multiple oscillatory waves. Without loss in generality, the one-dimensional equilibrium field $\mathbf{B} = B_0 \mathbf{e}_z$ is assumed to be along the \mathbf{e}_z direction. Using the Fourier representation, the perturbation can be written in a more general form, $\tilde{Q}_1(\mathbf{r}, t) = Q_1 \exp[-i(\omega t - \mathbf{k} \cdot \mathbf{r})]$, with wave vector $\mathbf{k} = k_{\perp} \mathbf{e}_y + k_{\parallel} \mathbf{e}_z$. By replacing $\partial/\partial t \rightarrow -i\omega$ and $\nabla \rightarrow i\mathbf{k}$, the linearised momentum equation (2.61)

reduces to

$$\omega^2 \rho_0 \boldsymbol{\xi} + \gamma p_0 (\mathbf{k} \cdot \boldsymbol{\xi}) \mathbf{k} + \frac{1}{\mu_0} \{ \mathbf{k} \times [\mathbf{k} \times (\boldsymbol{\xi} \times \mathbf{B}_0)] \} \times \mathbf{B}_0 = 0, \quad (2.70)$$

where ρ_0 and p_0 are equilibrium density and pressure, respectively. Equivalently, Eq. (2.70) can be written as the following scalar equations:

$$(\omega^2 - k_{\parallel}^2 v_A^2) \xi_x = 0, \quad (2.71)$$

$$(\omega^2 - k_{\perp}^2 v_s^2 - k_{\parallel}^2 v_A^2) \xi_y - (k_{\perp} k_{\parallel} v_s^2) \xi_z = 0, \quad (2.72)$$

$$-(k_{\perp} k_{\parallel} v_s^2) \xi_y + (\omega^2 - k_{\parallel}^2 v_s^2) \xi_z = 0, \quad (2.73)$$

where $v_A = \sqrt{B_0^2 / \mu_0 \rho_0}$ is the Alfvén speed, $v_s = \sqrt{\gamma p_0 / \rho_0}$ is the adiabatic sound speed and $k^2 = k_{\perp}^2 + k_{\parallel}^2$. Non-trivial solutions of $\boldsymbol{\xi}$ require the determinant of this system be zero, giving the dispersion relation

$$\begin{aligned} \omega^2 &= k_{\parallel}^2 v_A^2 && \text{Alfvén wave,} \\ \omega^2 &= \frac{1}{2} k^2 (v_A^2 + v_s^2) (1 \pm \sqrt{1 - \alpha^2}) && \text{fast and slow magnetosonic waves,} \end{aligned} \quad (2.74)$$

with

$$\alpha^2 = 4 \frac{k_{\parallel}^2}{k^2} \frac{v_A^2 v_s^2}{(v_A^2 + v_s^2)^2}. \quad (2.75)$$

The first solution $\omega^2 = k_{\parallel}^2 v_A^2$ corresponds to the shear Alfvén wave and is independent of k_{\perp} . The Alfvén waves were first proposed by H. Alfvén when he studied the coronal heating problem in 1942 [54]. These are transverse waves with both \mathbf{u}_1 and \mathbf{B}_1 perpendicular to \mathbf{B}_0 and \mathbf{k} . The bending field line provides a restoring force so the plasma oscillates with the field line, leading to an energy transformation between the perpendicular plasma kinetic energy and the magnetic energy. The positive and negative sign in the dispersion relation (2.74) describes the fast and slow magnetosonic waves, respectively. They are compressional waves producing fluctuations in plasma pressure and density. Each solution of ω represents a mode of the oscillatory

waves. Since $0 \leq \alpha^2 \leq 1$ all ω^2 are positive, implying that plasma waves in the homogeneous field are stable modes. In more realistic geometries, one retains the general features of compressional and shear Alfvén waves as well as combinations thereof but that the eigenfunctions become considerably more complicated and are obtained using linear stability codes such as MISHKA [76].

2.4.4 Landau damping

Landau damping [65, 77] describes a resonant process of the wave-particle interaction. This process is collisionless but involves energy transfer between waves and particles in the plasma. Consider an infinite homogeneous magnetic field $\mathbf{B} = B_0 \mathbf{e}_z$ and a small electrostatic perturbation $\mathbf{E} = E \cos(kz - \omega t) \mathbf{e}_z$. The perturbed field is assumed to be parallel to the magnetic field line and to propagate along the z direction. The drift motion of a charged particle in such electromagnetic field is governed by the following equations:

$$\begin{aligned} \frac{dv}{dt} &= \frac{q}{m} E \cos(\omega t - kz), \\ \frac{dz}{dt} &= v, \end{aligned} \tag{2.76}$$

with initial conditions $v(0) = v_i$ and $z(0) = z_i$.

Since the amplitude of the perturbation is small, the solution to Eq. (2.76) can be approximated by the unperturbed term and the first order correction: $v = v_0 + v_1$ and $z = z_0 + z_1$. The leading unperturbed solution corresponds to a free streaming motion along the magnetic field, given by $v_0 = v_{\parallel}$ and $z_0(t) = v_{\parallel}t + z_i$. v_1 and z_1 satisfy the following equations

$$\begin{aligned} \frac{dv_1}{dt} &= \frac{q}{m} E \cos(\omega t - kv_{\parallel}t - kz_i), \\ \frac{dz_1}{dt} &= v_1, \end{aligned} \tag{2.77}$$

with initial conditions $v_1(0) = 0$ and $z_1(0) = 0$. The first order solution is given by

$$\begin{aligned} v_1 &= \frac{qE}{m\alpha} [\sin(\alpha t - kz_i) + \sin kz_i], \\ z_1 &= \frac{qE}{m\alpha} \left[-\frac{\cos(\alpha t - kz_i) + \cos kz_i}{\alpha} + t \sin kz_i \right], \end{aligned} \quad (2.78)$$

with $\alpha = \omega - kv_{\parallel}$.

The change in particle energy per unit time due to the wave is given by

$$\begin{aligned} \frac{dW}{dt} &= \frac{d}{dt} \left(\frac{1}{2} m v^2 \right) = q \mathbf{v} \cdot \mathbf{E} \\ \frac{dW}{dt} &= q \left[v_0 E_1(z_0, t) + v_0 \frac{\partial E_1(z_0, t)}{\partial z_0} z_1 + v_1 E_1(z_0, t) \right] \end{aligned} \quad (2.79)$$

where the second order correction is included. Averaging over all the initial positions within one wavelength gives an averaged change in particle energy,

$$\begin{aligned} \left\langle \frac{dW}{dt} \right\rangle_{z_i} &= \frac{k}{2\pi} \int_0^{2\pi/k} \frac{dW}{dt} dz_i, \\ \left\langle \frac{dW}{dt} \right\rangle_{z_i} &= \frac{q^2 E^2}{2m} \left(\frac{\omega}{\alpha^2} \sin \alpha t - \frac{\omega t}{\alpha} \cos \alpha t + t \cos \alpha t \right). \end{aligned} \quad (2.80)$$

Now consider the distribution of the particle velocity $f_0(v_{\parallel}, v_{\perp})$. Taking an average over the entire velocity space distribution and integrating by parts yields

$$\begin{aligned} \left\langle \frac{dW}{dt} \right\rangle_{z_i, v_{\parallel}} &= \int_{-\infty}^{+\infty} f_0 \cdot \left\langle \frac{dW}{dt} \right\rangle_{z_i} dv_{\parallel}, \\ \left\langle \frac{dW}{dt} \right\rangle_{z_i, v_{\parallel}} &= -\frac{q^2 E^2 n_0}{2mk} \int_{-\infty}^{+\infty} \left(\frac{\omega \sin \alpha t}{\alpha} - \sin \alpha t \right) \frac{\partial f_{\parallel}}{\partial v_{\parallel}} dv_{\parallel}, \end{aligned} \quad (2.81)$$

where $f_{\parallel} = (2\pi/n_0) \int f_0 v_{\perp} dv_{\perp}$. For $t \rightarrow \infty$, particles with $\alpha \approx 0$, that is $v_{\parallel} \approx \omega/k$, contribute to the integral. These particles are resonant particles. When $\alpha \neq 0$, the integration vanishes because of the oscillating integrand.

The resulting power gained by all the particles is given by

$$\left\langle \frac{dW}{dt} \right\rangle_{z_i, v_{\parallel}} = -\frac{\pi q^2 E^2 n_0 \omega}{2mk^2} \left(\frac{\partial f_{\parallel}}{\partial v_{\parallel}} \right)_{\omega/k}, \quad (2.82)$$

The conclusion is that the resonant particles have wave phase velocity $v_{\parallel} \approx \omega/k$. The resonant particles absorb energy from the wave when $\partial f_{\parallel} / \partial v_{\parallel} < 0$.

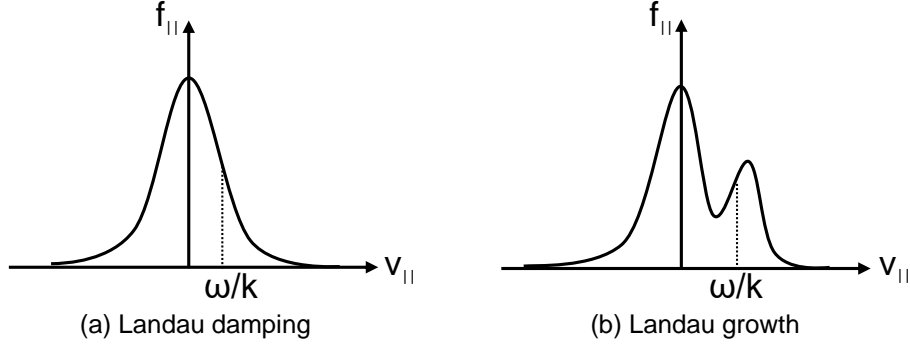


Figure 2.5: Particles with velocity above resonance gain energy from waves and lose energy to waves when below resonance. Landau damping occurs when $\frac{\partial f_{\parallel}}{\partial v_{\parallel}} < 0$ indicating more particles gain energy than lose energy which leads to a net growth in particle energy and damping in wave energy. Landau growth corresponds to a opposite situation.

Conversely, when $\partial f_{\parallel}/\partial v_{\parallel} > 0$, the wave can grow because it gains energy from the resonant particles.

At a small region where $v_{\parallel} \approx \omega/k$, particles with velocity $v_{\parallel} > \omega/k$ can give away their energy to the wave lowering the average velocity to the phase velocity; slower particles with $v_{\parallel} < \omega/k$ can gain energy from the wave increasing the average velocity to the phase velocity. As shown in Fig. (2.5)(a), $\partial f_{\parallel}/\partial v_{\parallel} < 0$ at $v_{\parallel} = \omega/k$, there are more particles taking energy from the wave than those losing energy to the wave. The net particles energy increases leading to the wave damping. Fig. (2.5)(b) is the case where $\partial f_{\parallel}/\partial v_{\parallel} > 0$ at $v_{\parallel} = \omega/k$, less particles absorb energy from the wave so the wave can grow.

2.5 Kinetic-MHD model

This section reviews the expression for the linear perturbation to a guiding centre distribution function due to interaction with a mode field. From this expression it can be seen that a necessary but not sufficient condition for large power transfer between the wave and particle populations is that the

particles satisfy a resonance condition. This section is reproduced mostly unaltered from [66].

2.5.1 Guiding centre theory

As discussed in section 2.1.1, the motion of the guiding centre can be decomposed into parallel streaming $v_{\parallel} \mathbf{b}$, and perpendicular drift motions including the ∇B drift, the curvature drift, and $\mathbf{E} \times \mathbf{B}$ drift:

$$\begin{aligned} \dot{\mathbf{X}} &= v_{\parallel} \mathbf{b} + \mathbf{v}_{\nabla B} + \mathbf{v}_{\kappa} + \mathbf{v}_{E \times B} \\ &= v_{\parallel} \mathbf{b} + \frac{1}{m\omega_c} \mathbf{b} \times (\mu \nabla B + mv_{\parallel}^2 \boldsymbol{\kappa} - Ze\mathbf{E}), \end{aligned} \quad (2.83)$$

where \mathbf{X} denotes the guiding centre position. $\omega_c = ZeB/m$ is the particle gyro frequency and $\mathbf{b} = \mathbf{B}/|\mathbf{B}|$. $\boldsymbol{\kappa} = (\mathbf{b} \cdot \nabla) \mathbf{b}$ is the curvature vector. The parallel momentum equation is given by

$$m\dot{v}_{\parallel} = -\mu \mathbf{b} \cdot \nabla B + Ze \mathbf{b} \cdot \mathbf{E} + mv_{\parallel} \boldsymbol{\kappa} \cdot \dot{\mathbf{X}} \quad (2.84)$$

The Lagrangian of the guiding centre is written as

$$\mathcal{L} = (Ze\mathbf{A} + mv_{\parallel} \mathbf{b}) \cdot \dot{\mathbf{X}} + \frac{1}{\omega_c} y \dot{\alpha} - \frac{1}{2} mv_{\parallel}^2 - y - Ze\Phi \quad (2.85)$$

where α is the gyro phase angle, and $y = \mu B$ is the perpendicular kinetic energy. The Lagrangian is regarded as a function of the new variables in the phase space, $\mathcal{L} = \mathcal{L}(\mathbf{X}, v_{\parallel}, y, \alpha; \dot{\mathbf{X}}, \dot{v}_{\parallel}, \dot{y}, \dot{\alpha}; t)$. Substituting \mathcal{L} in the Euler-Lagrange equations of motion for each component:

$$\frac{d}{dt} \left(\frac{\partial \mathcal{L}}{\partial \dot{y}} \right) - \frac{\partial \mathcal{L}}{\partial y} = 0 \implies \dot{\alpha} = \omega_c, \quad (2.86)$$

$$\frac{d}{dt} \left(\frac{\partial \mathcal{L}}{\partial \dot{\alpha}} \right) - \frac{\partial \mathcal{L}}{\partial \alpha} = 0 \implies \frac{d}{dt} \left(\frac{y}{\omega_c} \right) = 0 \implies \mu = \text{constant}, \quad (2.87)$$

$$\frac{d}{dt} \left(\frac{\partial \mathcal{L}}{\partial \dot{v}_{\parallel}} \right) - \frac{\partial \mathcal{L}}{\partial v_{\parallel}} = 0 \implies v_{\parallel} = \mathbf{b} \cdot \dot{\mathbf{X}}, \quad (2.88)$$

$$\frac{d}{dt} \left(\frac{\partial \mathcal{L}}{\partial \dot{\mathbf{X}}} \right) - \frac{\partial \mathcal{L}}{\partial \mathbf{X}} = 0 \implies Ze(\mathbf{E}^* + \frac{1}{c} \dot{\mathbf{X}} \times \mathbf{B}^*) = \mu \nabla B + m\dot{v}_{\parallel} \mathbf{b}, \quad (2.89)$$

where

$$\mathbf{E}^* = -\nabla\Phi - \frac{1}{c} \frac{\partial \mathbf{A}^*}{\partial t}, \quad (2.90)$$

$$\mathbf{A}^* = \mathbf{A} + \frac{mv}{Ze} v_{\parallel} \mathbf{b}, \quad (2.91)$$

$$\mathbf{B}^* = \nabla \times \mathbf{A}^* = \mathbf{B} + \frac{mc}{Ze} v_{\parallel} \nabla \times \mathbf{b}. \quad (2.92)$$

Eq. (2.86) and (2.88) correspond to the definition of the gyro frequency and the parallel velocity of a charged particle, respectively. Eq. (2.87) shows that the magnetic moment μ is an adiabatic invariant. The \mathbf{X} component of equation (2.89) is consistent with the equations of motions (2.83) and (2.84). This consistency justifies the choice of the Lagrangian \mathcal{L} as stated in Eq. (2.85).

The particle energy consists of the kinetic contributions and the electric potential energy $\epsilon = mv_{\parallel}^2/2 + \mu B + Ze\Phi$ and the expression for $\dot{\epsilon}$ is written as

$$\begin{aligned} \dot{\epsilon} &= mv_{\parallel} \dot{v}_{\parallel} + \mu \dot{B} + Ze \dot{\Phi} \\ \dot{\epsilon} &= - \left(Ze \frac{\partial \mathbf{A}}{\partial t} + mv_{\parallel} \frac{\partial \mathbf{b}}{\partial t} \right) \cdot \dot{\mathbf{X}} + \mu \frac{\partial B}{\partial t} + Ze \frac{\partial \Phi}{\partial t} \end{aligned} \quad (2.93)$$

where $\partial/\partial t = d/dt - \dot{\mathbf{X}} \cdot \nabla$. The first term $mv_{\parallel} \dot{v}_{\parallel}$ is given by dotting $\dot{\mathbf{X}}$ on Eq. (2.89):

$$\begin{aligned} Ze \mathbf{E}^* \cdot \dot{\mathbf{X}} &= \mu \dot{\mathbf{X}} \cdot \nabla B + mv_{\parallel} \mathbf{b} \cdot \dot{\mathbf{X}} \implies \\ mv_{\parallel} \dot{v}_{\parallel} &= - \left(Ze \nabla \Phi + \frac{Ze}{c} \frac{\partial \mathbf{A}}{\partial t} + mv_{\parallel} \frac{\partial \mathbf{b}}{\partial t} + \mu \nabla B \right) \cdot \dot{\mathbf{X}}, \end{aligned} \quad (2.94)$$

For an axisymmetric equilibrium, i.e. $\partial/\partial\phi = 0$ the toroidal canonical momentum of a guiding centre is a constant given by

$$\begin{aligned} P_{\phi} &= \frac{\partial \mathcal{L}}{\partial \dot{\phi}} = \frac{\partial}{\partial \dot{\phi}} \left[\left(Ze \mathbf{A} + mv_{\parallel} \mathbf{b} \right) \cdot \dot{\mathbf{X}} \right] \\ P_{\phi} &= \left(Ze \mathbf{A} + mv_{\parallel} \mathbf{b} \right) \cdot \frac{\partial \dot{\mathbf{X}}}{\partial \dot{\phi}} \\ P_{\phi} &= q A_{\phi} R + mv_{\parallel} \frac{RB_{\phi}}{B} = Ze \psi_p / 2\pi + mv_{\parallel} \frac{RB_{\phi}}{B}, \end{aligned} \quad (2.95)$$

where the covariant component is $\partial \mathbf{X} / \partial \phi = \partial \dot{\mathbf{X}} / \partial \dot{\phi} = R \mathbf{e}_\phi$ and ψ_p is the poloidal flux surface function.

The Vlasov equation (the kinetic equation neglecting collisions) is given by

$$\frac{\partial f}{\partial t} + \sum_{i=1}^n \dot{x}_i \frac{\partial f}{\partial x_i} = 0 \quad (2.96)$$

where $f(x_i; t)$ is the particle distribution function and $x_i, i = 1, n$ denote the phase space variables. Along the guiding centre trajectory and choosing the guiding centre variables $(\mathbf{X}, v_\parallel, y)$ as the phase space variables, the Vlasov equation becomes

$$\frac{\partial f}{\partial t} + \dot{\mathbf{X}} \cdot \nabla f + \dot{v}_\parallel \frac{\partial f}{\partial v_\parallel} + \dot{y} \frac{\partial f}{\partial y} = 0 \quad (2.97)$$

where f is assumed to be independent of α . $\dot{\mathbf{X}}$ and \dot{v}_\parallel are given in Eq. (2.83) and (2.84), and $\dot{y} = y(\dot{B} + \dot{\mathbf{X}} \cdot \nabla B)/B$.

2.5.2 Linear perturbation theory

Assume that an electromagnetic perturbation has caused a small variation in the particle distribution function f and we can write $f(\mathbf{X}, v_\parallel, y; t)$ as a linear combination of the equilibrium quantity f_0 and the first order perturbation f_1 : $f = f_0 + f_1$. The phase variables are also expanded as follows: $\dot{\mathbf{X}} = \dot{\mathbf{X}}_0 + \dot{\mathbf{X}}_1$, $\dot{v}_\parallel = \dot{v}_{\parallel 0} + \dot{v}_{\parallel 1}$ and $\dot{y} = \dot{y}_0 + \dot{y}_1$. The linearised drift-kinetic equation is written as

$$\frac{df_1}{dt} = -(\dot{\mathbf{X}}_1 \cdot \nabla f_0 + \dot{v}_{\parallel 1} \cdot \frac{\partial f_0}{\partial v_\parallel} + \dot{y}_1 \cdot \frac{\partial f_0}{\partial y}), \quad (2.98)$$

where the total derivative of f_1 is

$$\frac{df_1}{dt} = \frac{\partial f_1}{\partial t} + \dot{\mathbf{X}}_0 \cdot \nabla f_1 + \dot{v}_{\parallel 0} \cdot \frac{\partial f_1}{\partial v_\parallel} + \dot{y}_0 \cdot \frac{\partial f_1}{\partial y}. \quad (2.99)$$

We transform the right hand side of Eq. (2.98) to derivatives with respect to the constants of motion $\epsilon = mv_\parallel^2/2 + y + Ze\Phi$, μ and P_ϕ where $f_0 =$

$f_0(\epsilon, \mu, P_\phi; t)$:

$$\dot{\mathbf{X}}_1 \cdot \nabla f_0 = \dot{\mathbf{X}}_1 \cdot \left(\frac{\partial f_0}{\partial \epsilon} \nabla \epsilon + \frac{\partial f_0}{\partial \mu} \nabla \mu + \frac{\partial f_0}{\partial P_\phi} \nabla P_\phi \right), \quad (2.100)$$

$$\dot{v}_{\parallel 1} \cdot \frac{\partial f_0}{\partial v_{\parallel}} = \dot{v}_{\parallel 1} \cdot \left(\frac{\partial f_0}{\partial \epsilon} \frac{\partial \epsilon}{\partial v_{\parallel}} + \frac{\partial f_0}{\partial \mu} \frac{\partial \mu}{\partial v_{\parallel}} + \frac{\partial f_0}{\partial P_\phi} \frac{\partial P_\phi}{\partial v_{\parallel}} \right), \quad (2.101)$$

$$\dot{y}_1 \cdot \frac{\partial f_0}{\partial y} = \dot{y}_1 \cdot \left(\frac{\partial f_0}{\partial \epsilon} \frac{\partial \epsilon}{\partial y} + \frac{\partial f_0}{\partial \mu} \frac{\partial \mu}{\partial y} + \frac{\partial f_0}{\partial P_\phi} \frac{\partial P_\phi}{\partial y} \right), \quad (2.102)$$

where $\nabla \epsilon = Ze \nabla \Phi$, $\nabla \mu = -(y/B^2) \nabla B$, and $\nabla v_{\parallel} = \nabla y = 0$ because \mathbf{X} , v_{\parallel} and y are independent variables in phase space. Then Eq. (2.99) becomes

$$\begin{aligned} \frac{df_1}{dt} = & - \left[\left(\frac{\dot{y}_1}{B} - \frac{y}{B^2} \dot{\mathbf{X}}_1 \cdot \nabla B \right) \frac{\partial f_0}{\partial \mu} \right. \\ & + \left(\dot{\mathbf{X}}_1 \cdot \nabla P_\phi + \dot{v}_{\parallel 1} \frac{\partial P_\phi}{\partial v_{\parallel}} \right) \frac{\partial f_0}{\partial P_\phi} \\ & \left. + \left(Ze \dot{\mathbf{X}}_1 \cdot \nabla \Phi_0 + mv_{\parallel} \dot{v}_{\parallel 1} + \dot{y}_1 \right) \frac{\partial f_0}{\partial \epsilon} \right] \end{aligned} \quad (2.103)$$

We need to express the $\partial f_0/\partial \epsilon$, $\partial f_0/\partial \mu$ and $\partial f_0/\partial P_\phi$ terms with respect to the linearly perturbed Lagrangian $\mathcal{L}^{(1)}$.

Recall that the $\dot{\epsilon}$ expression is given in Eq. (2.93). The first-order corrections to the $\dot{\epsilon}$ equation can be used to evaluate the coefficient of the $\partial f_0/\partial \epsilon$ term in Eq. (2.103):

$$mv_{\parallel} \dot{v}_{\parallel 1} + \mu \dot{B}_1 + Ze \dot{\Phi}_1 = - \left(\frac{Ze}{c} \frac{\partial \mathbf{A}_1}{\partial t} + mv_{\parallel} \frac{\partial \mathbf{b}_1}{\partial t} \right) \cdot \dot{\mathbf{X}}_0, \quad (2.104)$$

$$mv_{\parallel} \dot{v}_{\parallel 1} + \dot{y}_1 + Ze \dot{\mathbf{X}}_1 \cdot \nabla \Phi_0 = -L_t^{(1)} - Ze \frac{D\Phi_1}{Dt}, \quad (2.105)$$

where the convective derivative along the unperturbed particle trajectory $D\Phi_1/Dt$ is found by the total derivative of the perturbed scalar potential Φ_1

$$\begin{aligned} \dot{\Phi}_1 &= \frac{d\Phi_1}{dt} = \left(\frac{\partial \Phi}{\partial t} + \dot{\mathbf{X}} \cdot \nabla \Phi \right)^{(1)} \\ \dot{\Phi}_1 &= \frac{\partial \Phi_1}{\partial t} + \dot{\mathbf{X}}_0 \cdot \nabla \Phi_1 + \dot{\mathbf{X}}_1 \cdot \nabla \Phi_0 \\ \dot{\Phi}_1 &= \frac{D\Phi_1}{Dt} + \dot{\mathbf{X}}_1 \cdot \nabla \Phi_0 \end{aligned} \quad (2.106)$$

and the term $L_t^{(1)}$ is defined by

$$-L_t^{(1)} = - \left(\frac{Ze}{c} \frac{\partial \mathbf{A}_1}{\partial t} + mv_{\parallel} \frac{\partial \mathbf{b}_1}{\partial t} \right) \cdot \dot{\mathbf{X}}_0 + \mu \frac{\partial B_1}{\partial t} + Ze \frac{\partial \Phi_1}{\partial t}. \quad (2.107)$$

Now we need to calculate the $\partial f_0/\partial P_\phi$ term in Eq. (2.103). P_ϕ is given in Eq. (2.95) and the time derivative of P_ϕ is written as

$$\dot{P}_\phi = \frac{\partial P_\phi}{\partial t} + \dot{\mathbf{X}} \cdot \nabla P_\phi + \dot{v}_\parallel \frac{\partial P_\phi}{\partial v_\parallel} \quad (2.108)$$

We have shown that P_ϕ is conserved along an unperturbed trajectory as $\dot{P}_\phi = \partial \mathcal{L}/\partial \phi = 0$. For a small perturbation, $\dot{P}_\phi^{(1)}$ is given by

$$\begin{aligned} \dot{P}_\phi^{(1)} &= \left(\dot{\mathbf{X}}_1 \cdot \nabla P_\phi^{(0)} + \dot{v}_{\parallel 1} \frac{\partial P_\phi^{(0)}}{\partial v_\parallel} \right) + \left(\frac{\partial P_\phi^{(1)}}{\partial t} + \dot{\mathbf{X}}_0 \cdot \nabla P_\phi^{(1)} + \dot{v}_{\parallel 0} \frac{\partial P_\phi^{(1)}}{\partial v_\parallel} \right) \\ \dot{P}_\phi^{(1)} &= \left(\dot{\mathbf{X}}_1 \cdot \nabla P_\phi^{(0)} + \dot{v}_{\parallel 1} \frac{\partial P_\phi^{(0)}}{\partial v_\parallel} \right) + \frac{DP_\phi^{(1)}}{Dt} = \left(\frac{\partial \mathcal{L}}{\partial \phi} \right)^{(1)}. \end{aligned} \quad (2.109)$$

Here, the terms in the first bracket appear in the $\partial f_0/\partial P_\phi$ term in Eq. (2.103) and can be determined by $(\partial \mathcal{L}/\partial \phi)^{(1)} - DP_\phi^{(1)}/Dt$:

$$\frac{DP_\phi^{(1)}}{Dt} = \frac{\partial P_\phi^{(1)}}{\partial t} + \dot{\mathbf{X}}_0 \cdot \nabla P_\phi^{(1)} + \dot{v}_{\parallel 0} \frac{\partial P_\phi^{(1)}}{\partial v_\parallel} \quad (2.110)$$

$$\begin{aligned} \left(\frac{\partial \mathcal{L}}{\partial \phi} \right)^{(1)} &= \left[\frac{Ze}{c} \left(\frac{\partial A_R^{(1)}}{\partial \phi} \mathbf{e}_R + \frac{\partial A_\phi^{(1)}}{\partial \phi} \mathbf{e}_\phi + \frac{\partial A_Z^{(1)}}{\partial \phi} \mathbf{e}_Z \right) \right. \\ &\quad \left. + mv_\parallel \left(\frac{\partial b_R^{(1)}}{\partial \phi} \mathbf{e}_R + \frac{\partial b_\phi^{(1)}}{\partial \phi} \mathbf{e}_\phi + \frac{\partial b_Z^{(1)}}{\partial \phi} \mathbf{e}_Z \right) \right] \cdot \dot{\mathbf{X}}_0 \\ &\quad - \mu \frac{\partial B_1}{\partial \phi} - Ze \frac{\partial \Phi_1}{\partial \phi} \end{aligned} \quad (2.111)$$

The time derivative of perpendicular kinetic energy \dot{y} is given by

$$\dot{y} = \mu \dot{B} = \mu \left(\frac{\partial B}{\partial t} + \dot{\mathbf{X}} \cdot \nabla B \right). \quad (2.112)$$

Then the perturbed forms of \dot{y} can be written as

$$\dot{y}_1 = \mu^{(0)} \left(\frac{\partial B_1}{\partial t} + \dot{\mathbf{X}}_0 \cdot \nabla B_1 + \dot{\mathbf{X}}_1 \cdot \nabla B_0 \right) + \mu^{(1)} \dot{\mathbf{X}}_0 \cdot \nabla B_0, \quad (2.113)$$

where $\mu^{(1)} = y_0 B_1 / B_0^2$. The $\partial f_0 / \partial \mu$ term in Eq. (2.103) can be obtained by constructing \dot{y}_1 / B_0

$$\frac{\dot{y}_1}{B_0} = \frac{y_0}{B_0} \left(\frac{\partial(B_1/B_0)}{\partial t} + \dot{\mathbf{X}}_0 \cdot \frac{1}{B_0} \nabla B_1 + \frac{1}{B_0} \dot{\mathbf{X}}_1 \cdot \nabla B_0 \right) - \frac{y_0}{B_0^2} B_1 \dot{\mathbf{X}}_0 \cdot \frac{1}{B_0} \nabla B_0, \quad (2.114)$$

$$\frac{\dot{y}_1}{B_0} - \frac{y}{B_0^2} \dot{\mathbf{X}}_1 \cdot \nabla B_0 = \mu^{(0)} \left(\frac{\partial(B_1/B_0)}{\partial t} + \dot{\mathbf{X}}_0 \cdot \nabla(B_1/B_0) \right) = \mu^{(0)} \frac{D}{Dt} \left(\frac{B_1}{B_0} \right) \quad (2.115)$$

Now we can substitute Eq. (2.105), (2.109) and (2.115) into Eq. (2.103) leading to

$$\begin{aligned} \frac{df_1}{dt} = & - \left\{ \left[\left(\frac{\partial \mathcal{L}}{\partial \phi} \right)^{(1)} - \frac{DP_\phi^{(1)}}{Dt} \right] \frac{\partial f_0}{\partial P_\phi^{(0)}} + \left(-L_t^{(1)} - Ze \frac{D\Phi_1}{Dt} \right) \frac{\partial f_0}{\partial \epsilon_0} \right. \\ & \left. + \mu^{(0)} \frac{D}{Dt} \left(\frac{B_1}{B_0} \right) \frac{\partial f_0}{\partial \mu^{(0)}} \right\} \end{aligned} \quad (2.116)$$

The solution to the perturbed distribution function f_1 can be separated into two parts

$$f_1 = P_\phi^{(1)} \frac{\partial f_0}{\partial P_\phi^{(0)}} + Ze \Phi \frac{\partial f_0}{\partial \epsilon_0} - \mu^{(0)} \frac{B_1}{B_0} \frac{\partial f_0}{\partial \mu^{(0)}} + h_1 \quad (2.117)$$

where h_1 is determined by

$$\frac{dh_1}{dt} = - \left(\frac{\partial \mathcal{L}}{\partial \phi} \right)^{(1)} \frac{\partial f_0}{\partial P_\phi^{(0)}} + L_t^{(1)} \frac{\partial f_0}{\partial \epsilon_0} \quad (2.118)$$

Note that the first order perturbed Lagrangian can be written as

$$\mathcal{L}^{(1)} = \left(\frac{Ze}{c} \mathbf{A}_1 + mv_{\parallel} \mathbf{b}_1 \right) \cdot \dot{\mathbf{X}}_0 - \mu^{(0)} B_1 - Ze \Phi_1. \quad (2.119)$$

We assume that perturbations have the form

$$\mathcal{L}^{(1)} = \hat{\mathcal{L}}^{(1)}(\psi, \theta) \exp(-i\omega t - in\phi) \quad (2.120)$$

where ψ is the equilibrium magnetic flux surface function, ϕ is the toroidal angle used in the cylindrical coordinates and θ is a generalised poloidal angle

defined by $\nabla\theta = \nabla\psi \times \nabla\phi$ which are discussed in detail in section 2.3. Consider a single harmonic and we have

$$\left(\frac{\partial\mathcal{L}}{\partial\phi}\right)^{(1)} = -in\mathcal{L}^{(1)} \quad (2.121)$$

$$\left(\frac{\partial\mathcal{L}}{\partial t}\right)^{(1)} = -i\omega\mathcal{L}^{(1)} = -i\omega L_t^{(1)} \quad (2.122)$$

$$\frac{dh_1}{dt} = -i(\omega - n\omega_*)\frac{\partial f_0}{\partial\epsilon_0}\mathcal{L}^{(1)} \quad (2.123)$$

where $L_t^{(1)}$ is given in Eq. (2.107) and ω_* is defined as

$$\omega_* = \frac{\partial f_0/\partial P_\phi^{(0)}}{\partial f_0/\partial\epsilon_0}. \quad (2.124)$$

We can separate $\phi(t)$ into a constant part and an oscillating part $\phi(t) = \langle\dot{\phi}\rangle t + \tilde{\phi}(t)$ where the constant part $\langle\dot{\phi}\rangle$ is averaged over bounce period τ_b . Hence the periodic part in $\mathcal{L}^{(1)}$ can be expanded in Fourier series

$$\tilde{\mathcal{L}}^{(1)} = \hat{\mathcal{L}}^{(1)} \exp(-in\tilde{\phi}) = \sum_{p=-\infty}^{+\infty} Y_p \exp(-ip\omega_b t), \quad (2.125)$$

where the Fourier coefficients Y_p are determined by

$$Y_p = \frac{1}{\tau_b} \oint \tilde{\mathcal{L}}^{(1)} \exp(-ip\omega_b t) dt \quad (2.126)$$

where $\omega_b = 2\pi/\tau_b$.

Substitution of Eq. (2.125) into Eq. (2.123) and integration over time give the solution of the non-adiabatic part of the perturbed distribution function h_1

$$h_1 = (\omega - n\omega_*)\frac{\partial f_0}{\partial\epsilon_0} \sum_{p=-\infty}^{+\infty} Y_p \times \frac{\exp\left[-i(\omega + n\langle\dot{\phi}\rangle + p\omega_b)t\right]}{\omega + n\langle\dot{\phi}\rangle + p\omega_b}. \quad (2.127)$$

2.5.3 Resonance condition

We consider an axisymmetric toroidal plasma consisting of the thermal and the hot components with $n_{th} \gg n_h$ and $T_{th} \ll T_h$. The linearised equilibrium

equation is obtained by considering these two components

$$(\mathbf{j} \times \mathbf{B})^{(1)} = \nabla p_{\text{th}}^{(1)} + \nabla p_{\text{h}}^{(1)}, \quad (2.128)$$

where the total current density \mathbf{j} consists of both the bulk and the energetic contributions, the thermal plasma pressure p_{th} is assumed to be isotropic and the hot plasma pressure p_{h} anisotropic. We can construct the quadratic form in presence of the energetic contribution

$$\delta W = \delta W_{\text{MHD}} + \delta W_{\text{hot}}. \quad (2.129)$$

Here, the low energy bulk plasmas are described by the ideal MHD fluid model and the MHD perturbed energy is given by

$$\begin{aligned} \delta W_{\text{MHD}} &= -\frac{1}{2} \int \boldsymbol{\xi}^* \cdot \mathbf{F}(\boldsymbol{\xi}) d^3x \\ &= -\frac{1}{2} \int [\boldsymbol{\xi}_{\perp}^* \cdot (\mathbf{j} \times \mathbf{B})^{(1)} - \boldsymbol{\xi}_{\perp}^* \cdot \nabla p_{\text{th}}^{(1)}] d^3x \end{aligned} \quad (2.130)$$

and the energetic component is

$$\delta W_{\text{hot}} = \frac{1}{2} \int \boldsymbol{\xi}_{\perp}^* \cdot \nabla p_{\text{h}}^{(1)} d^3x, \quad (2.131)$$

where the pressure $p_{\text{h}}^{(1)}$ consists of anisotropic perpendicular and parallel components determined by the perturbed distribution function f_1

$$\begin{pmatrix} p_{\parallel}^{(1)} \\ p_{\perp}^{(1)} \end{pmatrix} = \int d^3v \begin{pmatrix} mv_{\parallel}^2 \\ \mu B \end{pmatrix} f_1. \quad (2.132)$$

Recall that the force operator for the ideal MHD plasma is given in Eq. (2.64)

$$\mathbf{F}(\boldsymbol{\xi}) = -\omega^2 \rho_0 \boldsymbol{\xi}, \quad (2.64)$$

where $\mathbf{F}(\boldsymbol{\xi})$ is self-adjoint and ω^2 is purely real. Thus the MHD potential energy δW_{MHD} can be measured by the kinetic energy of the perturbation

$$\delta W_{\text{MHD}} = \omega^2 E_k, \quad (2.133)$$

where

$$E_k = \int \rho_0 \xi^2 d^3x. \quad (2.134)$$

As compared to the bulk plasma, the energetic perturbation is small, i.e. $\delta W_{\text{hot}} \ll \delta W_{\text{MHD}}$. Thus, δW_{hot} can be treated as a linear correction to the total potential energy. δW could include an imaginary part as the force operator is no longer self-adjoint in presence of the energetic contribution. The perturbed quadratic form can be written as

$$(\omega_r + i\omega_i)^2 E_k = \delta W_{\text{MHD}} + \delta W_{\text{hot}} \quad (2.135)$$

and the growth rate of the mode γ is given by

$$\frac{\gamma}{\omega} = \frac{\omega_i}{\omega_r} = \frac{\text{Im}[\delta W_{\text{hot}}]}{2\omega_r^2 E_k}, \quad (2.136)$$

where δW_{hot} is determined by the perturbed distribution function f_1 . Recall that the expression for f_1 has a singular point in the h_1 term as shown in Eq. (2.127). The integration of the singular point can produce an imaginary part and thus contribute to the growth of the mode when

$$\Gamma = \omega + n\langle\dot{\phi}\rangle + p\omega_b = 0. \quad (2.137)$$

Eq. (2.137) is also known as the resonance condition. Here, $\omega_\phi = \langle\dot{\phi}\rangle$ is defined as the toroidal precession frequency averaged over one bounce period and p is an arbitrary integer. The resonance takes place between energetic particles and MHD modes. Particles whose orbital frequencies satisfy this relation could potentially exchange energies with the mode with a frequency ω . The appearance of the resonance condition shows that large changes in the distribution function can occur when it is satisfied. The resonance condition is a necessary but not sufficient condition for large energy transfer between the particle and the waves as this also depends on the factors Y_p in Eq. (2.127) for the orbit in question.

An intuitive interpretation of the wave-particle resonance condition is described as follows. Suppose a particle on a bounce orbit starts at a position and completes a bounce orbit in time $T_b = 2\pi/\omega_b$. The representation of a wave harmonic is given by $\tilde{Q}(r, \theta, \phi, t) = \exp(-i\omega t + in\phi) \sum_m Q_m(r)(-im\theta)$. In this time, the phase of the wave advances by an amount $\Delta\zeta = \omega T_b$. The particle has also moved forwards by a toroidal angle $\Delta\phi = \omega_\phi T_b$. The total wave phase change the particle experiences after its bounce orbit is the sum of both, therefore $\Delta\zeta = \omega T_b + n\omega_\phi T_b$. For a resonance, this should be some multiple of 2π , that is, $\Delta\zeta = \omega T_b + n\omega_\phi T_b = -2p\pi$. Replacing the bounce period with $2\pi/\omega_b$ leads to the resonance condition $\omega + n\omega_\phi + p\omega_b = 0$, where p indicates the wave periods that the particle has advanced with respect to the wave over one bounce period. The resonance condition suggests that resonant particles are those which return to the same wave phase after a poloidal bounce orbit. We will use these results in Chapters 3 and 4 to identify and study the resonant particles in experimental MAST plasma discharges.

Particle tracking in electromagnetic fields

Single particle motion is the fundamental process underlying the behaviour of a plasma in a magnetic confinement fusion device. Understanding more complex plasma processes such as wave-particle interaction, plasma heating and fast ion transport often requires a detailed understanding of the behaviour of individual particles in electromagnetic fields. In a toroidal confinement device, the helical magnetic field is characterised by the safety factor q and is a complex function of position. The motion of a charged particle in such field will be determined by the numerical solutions to the equations of motion. In many situations, particles need to be tracked for a very long time in the simulation code because the gyro motion is fast and the excursion of the orbit is small compared to the geometry of the experimental device. These problems can be alleviated by numerically solving the equations of motion of the guiding centre when the variations of the field are negligible over the gyro motion and the Larmor radii r_c satisfies $r_c \ll L_c$ with length scale $L_c = B/|\nabla B|$. The guiding centre simulation deals with gyro averaged quantities

and puts emphasis on the drift motions so the computation time can be significantly reduced.

In MAST, particles produced by deuterium beam injection or alpha particles released from the nuclear reactions are highly energetic. For simulating these energetic particles, two facts prevent the guiding centre simulation being a good approximation of the full orbit calculation. Firstly, MAST is designed to confine plasmas in an equilibrium with high $\beta = 2p/\mu B^2$ and relatively low field. The toroidal field at the magnetic axis $B_T \sim 0.5$ T, as compared with 3.6 T in JET. These configurations of MAST can produce a very large gyro radii for fast ions. On the other hand, MAST is configured with a tight aspect ratio meaning the gradient and curvature of the field are prominent throughout and cannot be neglected within the timescale and length scale of gyro motion. Because of these reasons, the condition $r_c \ll L_c$ will not always be satisfied by MAST fast particles and thus a stable and accurate full orbit simulation becomes necessary.

The wave-particle resonance condition Eq. (2.137) is derived in the previous chapter, one would like to know which particles will resonate with a mode in order to help understand the dynamics of wave particle interactions. Therefore, a code is developed to evaluate the relevant bounce and precession frequencies. This chapter focuses on this code development and is organised as follows. Section 3.1 outlines the Boris Leapfrog solver which provides an efficient and accurate method for tracking particles. Section 3.2 presents the coordinate transformation of the magnetic field between the cylindrical coordinates commonly used to represent fields in axisymmetric tokamaks and the Cartesian coordinates needed to implement the Boris solver. The initialisation of the particle pushing code and the workflow of the code are described in sections 3.3 and 3.4. The code is validated with an analytical solution as

shown in section 3.5. As an important application of the code, orbits and motion frequencies of the plasma in MAST are calculated in sections 3.6 and 3.7.

3.1 The Boris solver

The magnetic field in a tokamak primarily consists of toroidal components generated by external coils and poloidal components produced by plasma currents. The solutions to the equations of motion for a charged particle in such a complex electromagnetic configuration can only be obtained numerically. One common numerical approach is to use finite difference methods [78]. There are two categories of finite difference methods, explicit and implicit, depending upon if the new time points are used to evaluate the spatial derivatives. The explicit methods need only old time points to advance spatial locations so they are fast. However, these methods often suffer stability problems and have requirements on the time intervals. The implicit methods need new time points to evaluate some spatial derivatives so the spatial locations are updated iteratively. The implicit methods thus require more computational effort but they are more stable and allow larger time intervals. For the particle motion problem, either explicit or implicit methods use the velocity at time point n to push particles from location n to next location $n + 1$. A leapfrog method uses the average velocity at time point $v_{n+1/2}$ to move x_n to x_{n+1} as shown in Fig. 3.1, where the initial velocity is given a $1/2$ time step behind the initial position. It is a time-centred difference algorithm and possesses good global stability specially for computing orbital dynamics.

The Boris algorithm [79] is an explicit leapfrog method which is commonly

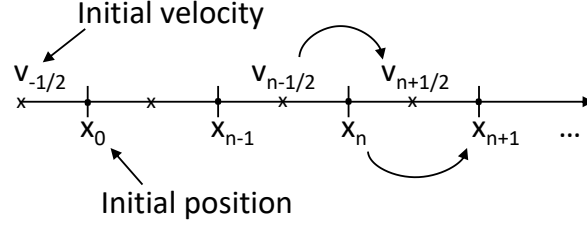


Figure 3.1: Leapfrog scheme. The initial velocity and position are given and updated in a staggered way. The velocity $v_{n-1/2}$ is advanced to $v_{n+1/2}$ after a time interval and the position x_n is updated to x_{n+1} using $v_{n+1/2}$.

used for advancing a charged particle in a realistic electromagnetic field for its speed and stability. It is a second order method and conserves phase space volume which suggests it should have good long term fidelity [80]. Using the leapfrog scheme, the discretised form of Eq. (2.1) is written as:

$$\frac{\mathbf{x}_{n+1} - \mathbf{x}_n}{\Delta t} = \mathbf{v}_{n+1/2}, \quad (3.1)$$

$$\frac{\mathbf{v}_{n+1/2} - \mathbf{v}_{n-1/2}}{\Delta t} = \frac{q}{m}(\mathbf{E}_n + \frac{\mathbf{v}_{n+1/2} + \mathbf{v}_{n-1/2}}{2} \times \mathbf{B}_n). \quad (3.2)$$

Here, the electromagnetic fields \mathbf{B}_n and \mathbf{E}_n are evaluated at x_n . Then \mathbf{E}_n can be cancelled out by introducing new variables \mathbf{v}^- and \mathbf{v}^+ :

$$\mathbf{v}_{n-1/2} = \mathbf{v}^- - \frac{q\mathbf{E}_n}{m} \frac{\Delta t}{2}, \quad (3.3)$$

$$\mathbf{v}_{n+1/2} = \mathbf{v}^+ + \frac{q\mathbf{E}_n}{m} \frac{\Delta t}{2}, \quad (3.4)$$

Substituting these expressions into Eq. (3.2) yields

$$\frac{\mathbf{v}^+ - \mathbf{v}^-}{\Delta t} = \frac{q}{2m}(\mathbf{v}^+ + \mathbf{v}^-) \times \mathbf{B}_n. \quad (3.5)$$

\mathbf{x}_n is updated to \mathbf{x}_{n+1} by the velocity at the last half time step $\mathbf{v}_{n+1/2}$:

$$\mathbf{x}_{n+1} = \mathbf{v}_{n+1/2}\Delta t + \mathbf{x}_n \quad (3.6)$$

$$= (\mathbf{v}^+ + \frac{q\mathbf{E}_n}{m} \frac{\Delta t}{2})\Delta t + \mathbf{x}_n. \quad (3.7)$$

Despite \mathbf{v}^+ appearing on both sides of Eq. (3.5), this is explicit and \mathbf{v}^+ is given by

$$\mathbf{v}^+ = \mathbf{v}^- + \mathbf{v}' \times \mathbf{s} \quad (3.8)$$

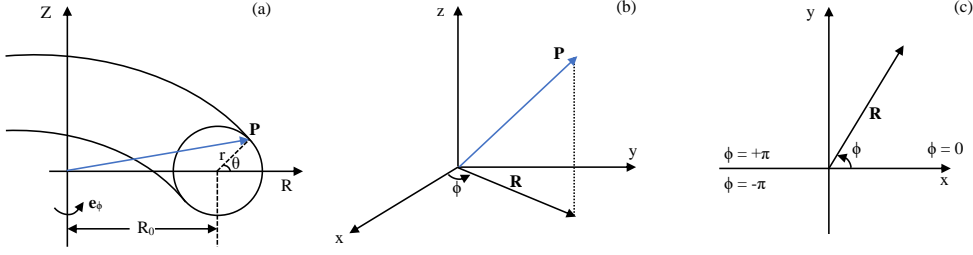


Figure 3.2: (a) Two-dimensional tokamak geometry with a circular cross section where R_0 is known as the major radius and r the minor radius. (b) A position vector $\mathbf{P}(x, y, z)$ is projected on the x - y plane giving the radial component \mathbf{R} and the toroidal angle ϕ ; (c) Relationships between the position components: $x = R \cos \phi$, $y = R \sin \phi$ and $z = Z$ with $\phi \in [-\pi, \pi]$.

with

$$\mathbf{v}' = \mathbf{v}^- + \mathbf{v}^- \times \mathbf{t}, \quad (3.9)$$

$$\mathbf{t} = \frac{q\mathbf{B}_n}{m} \frac{\Delta t}{2}, \quad (3.10)$$

$$\mathbf{s} = \frac{2\mathbf{t}}{1 + t^2}. \quad (3.11)$$

3.2 Coordinate transformations

The Boris scheme has been introduced using Cartesian coordinates which can be represented by unit vectors \mathbf{e}_x , \mathbf{e}_y , and \mathbf{e}_z . For following the single particle motion in a toroidal device, the electromagnetic field is often given in terms of cylindrical coordinates. Because of the axisymmetry of the field, it is convenient to use cylindrical coordinates so that the system is independent of the azimuth angle. A right handed cylindrical coordinate system formed by unit vectors \mathbf{e}_R , \mathbf{e}_ϕ and \mathbf{e}_Z is illustrated in Fig. 3.2, where R is the radial position, Z the vertical position and ϕ the toroidal angle. The mathematics thus can be greatly simplified in the analysis and derivations of the equations. ϕ is periodic with period 2π ranging from $-\pi$ to $+\pi$. A position vector \mathbf{P} can be expressed in terms of the Cartesian and cylindrical coordinate systems,

respectively,

$$\mathbf{P} = x\mathbf{e}_x + y\mathbf{e}_y + z\mathbf{e}_z = R\mathbf{e}_R + Z\mathbf{e}_Z, \quad (3.12)$$

where each component is related by

$$\begin{cases} x = R \cos \phi, \\ y = R \sin \phi, \\ z = Z. \end{cases} \quad (3.13)$$

Here the vertical components z and Z are identical in these two coordinate systems.

The simulation also requires the coordinate transformations for the other vectors such as particle velocity and magnetic field. The transformations can be generalised by using a Jacobian matrix. The Jacobian J of the transformations from the x, y, z coordinates to the R, ϕ, Z coordinates depends only on ϕ and the derivations are presented as follows.

In cylindrical system, the basis vectors \mathbf{e}_R , \mathbf{e}_ϕ , and \mathbf{e}_Z are orthogonal to each other, defined by

$$\begin{bmatrix} \mathbf{e}_R \\ \mathbf{e}_\phi \\ \mathbf{e}_Z \end{bmatrix} = \begin{bmatrix} \frac{\partial x}{\partial R} & \frac{\partial y}{\partial R} & \frac{\partial z}{\partial R} \\ \frac{\partial x}{\partial \phi} & \frac{\partial y}{\partial \phi} & \frac{\partial z}{\partial \phi} \\ \frac{\partial x}{\partial Z} & \frac{\partial y}{\partial Z} & \frac{\partial z}{\partial Z} \end{bmatrix} \begin{bmatrix} \mathbf{e}_x \\ \mathbf{e}_y \\ \mathbf{e}_z \end{bmatrix} = \begin{bmatrix} \cos \phi & \sin \phi & 0 \\ -R \sin \phi & R \cos \phi & 0 \\ 0 & 0 & 1 \end{bmatrix} \begin{bmatrix} \mathbf{e}_x \\ \mathbf{e}_y \\ \mathbf{e}_z \end{bmatrix}, \quad (3.14)$$

where the expression (3.13) is used to evaluate the partial derivatives. To convert from covariant to unit basis vectors \mathbf{e}_ϕ is normalised by dividing by R . Going forwards \mathbf{e}_R , \mathbf{e}_ϕ , and \mathbf{e}_Z represent the unit basis vectors in the cylindrical system given by

$$\begin{bmatrix} \mathbf{e}_R \\ \mathbf{e}_\phi \\ \mathbf{e}_Z \end{bmatrix} = \mathbf{J} \begin{bmatrix} \mathbf{e}_x \\ \mathbf{e}_y \\ \mathbf{e}_z \end{bmatrix}, \quad (3.15)$$

with Jacobian matrix

$$\mathbf{J} = \begin{bmatrix} \cos \phi & \sin \phi & 0 \\ -\sin \phi & \cos \phi & 0 \\ 0 & 0 & 1 \end{bmatrix}. \quad (3.16)$$

Similarly, the inverse transformation can be realised and the inverse Jacobian matrix J^{-1} is given by

$$\begin{bmatrix} \mathbf{e}_x \\ \mathbf{e}_y \\ \mathbf{e}_z \end{bmatrix} = \begin{bmatrix} \cos \phi & -\sin \phi & 0 \\ \sin \phi & \cos \phi & 0 \\ 0 & 0 & 1 \end{bmatrix} \begin{bmatrix} \mathbf{e}_R \\ \mathbf{e}_\phi \\ \mathbf{e}_Z \end{bmatrix} = \mathbf{J}^{-1} \begin{bmatrix} \mathbf{e}_R \\ \mathbf{e}_\phi \\ \mathbf{e}_Z \end{bmatrix}. \quad (3.17)$$

Combining Eq. (3.15) and Eq. (3.17) gives the inner product of the unit vectors

$$\begin{bmatrix} \mathbf{e}_R \mathbf{e}_x & \mathbf{e}_\phi \mathbf{e}_x & \mathbf{e}_Z \mathbf{e}_x \\ \mathbf{e}_R \mathbf{e}_y & \mathbf{e}_\phi \mathbf{e}_y & \mathbf{e}_Z \mathbf{e}_y \\ \mathbf{e}_R \mathbf{e}_z & \mathbf{e}_\phi \mathbf{e}_z & \mathbf{e}_Z \mathbf{e}_z \end{bmatrix} = \begin{bmatrix} \cos \phi & -\sin \phi & 0 \\ \sin \phi & \cos \phi & 0 \\ 0 & 0 & 1 \end{bmatrix}. \quad (3.18)$$

An arbitrary vector \mathbf{B} can be expressed in terms of a unit basis in either coordinate system:

$$\mathbf{B} = B_x \mathbf{e}_x + B_y \mathbf{e}_y + B_z \mathbf{e}_z = B_R \mathbf{e}_R + B_\phi \mathbf{e}_\phi + B_Z \mathbf{e}_Z. \quad (3.19)$$

Taking the dot product of the unit vectors \mathbf{e}_R , \mathbf{e}_ϕ and \mathbf{e}_Z in turn on vector \mathbf{B} gives the relations of the components of two system:

$$\mathbf{e}_R \cdot \mathbf{B} = B_R = (B_x \mathbf{e}_x + B_y \mathbf{e}_y + B_z \mathbf{e}_z) \mathbf{e}_R = B_x \cos \phi + B_y \sin \phi, \quad (3.20)$$

$$\mathbf{e}_\phi \cdot \mathbf{B} = B_\phi = (B_x \mathbf{e}_x + B_y \mathbf{e}_y + B_z \mathbf{e}_z) \mathbf{e}_\phi = -B_x \sin \phi + B_y \cos \phi, \quad (3.21)$$

$$\mathbf{e}_Z \cdot \mathbf{B} = B_Z = (B_x \mathbf{e}_x + B_y \mathbf{e}_y + B_z \mathbf{e}_z) \mathbf{e}_Z = B_z. \quad (3.22)$$

The coordinate transformations are completed by writing Eq.(3.20) - (3.22)

in a compact form

$$\begin{bmatrix} B_R \\ B_\phi \\ B_Z \end{bmatrix} = \begin{bmatrix} \cos \phi & \sin \phi & 0 \\ -\sin \phi & \cos \phi & 0 \\ 0 & 0 & 1 \end{bmatrix} \begin{bmatrix} B_x \\ B_y \\ B_z \end{bmatrix} = \mathbf{J} \begin{bmatrix} B_x \\ B_y \\ B_z \end{bmatrix}, \quad (3.23)$$

and

$$\begin{bmatrix} B_x \\ B_y \\ B_z \end{bmatrix} = \begin{bmatrix} \cos \phi & -\sin \phi & 0 \\ \sin \phi & \cos \phi & 0 \\ 0 & 0 & 1 \end{bmatrix} \begin{bmatrix} B_R \\ B_\phi \\ B_Z \end{bmatrix} = \mathbf{J}^{-1} \begin{bmatrix} B_R \\ B_\phi \\ B_Z \end{bmatrix} \quad (3.24)$$

with determinant $\det(\mathbf{J}) \neq 0$. As one typically stores fields in coordinates, these transformations allow us to convert the field components into a Cartesian system. Then the Boris solver can be easily implemented by simply calling these prescribed transformation matrices in the program.

3.3 Initialisation

The initial conditions required for solving the Lorentz motion of a charged particle are the position $\mathbf{P}_0(x_0, y_0, z_0)$ and the velocity $\mathbf{V}_0(v_{x0}, v_{y0}, v_{z0})$ regardless of which coordinate system is taken. It is also common that the initial conditions are expressed in terms of energy E , pitch $\lambda = v_{\parallel}/v$ and position $\mathbf{P}_0(R, \phi, Z)$ in order to intuitively describe the particles. Now we just need one last coordinate, the gyrophase angle α , to initialise the simulation. The particle velocity will be determined by using $(E, \lambda, R, \phi, Z, \alpha)$, together with a prescribed equilibrium field for the given location \mathbf{P}_0 . The procedure for obtaining the velocity is as follows.

The equilibrium field is expressed in terms of cylindrical unit vectors $B = B_R \mathbf{e}_R + B_\phi \mathbf{e}_\phi + B_Z \mathbf{e}_Z$. The magnetic vector \mathbf{b}_{\parallel} is defined by $\mathbf{b}_{\parallel} = \mathbf{B}/|\mathbf{B}|$.

One of the perpendicular basis vectors can be chosen as

$$\mathbf{b}_{\perp 1} = \frac{1}{\sqrt{B_Z^2 + B_R^2}}(-B_Z \mathbf{e}_R + B_R \mathbf{e}_Z). \quad (3.25)$$

Here the toroidal component is set to zero. The radial and vertical components of \mathbf{B} are swapped and cast into the radial and vertical components of $\mathbf{b}_{\perp 1}$ in order to satisfy $\mathbf{b}_{\perp 1} \cdot \mathbf{b}_{\parallel} = 0$. $\mathbf{b}_{\perp 1}$ is corrected by $(B_Z^2 + B_R^2)^{1/2}$ so that $|\mathbf{b}_{\perp 1}| = 1$ is a unit vector. Another perpendicular basis vector can be determined by the cross product of $\mathbf{b}_{\perp 1}$ and \mathbf{b}_{\parallel} given by $\mathbf{b}_{\perp 2} = \mathbf{b}_{\perp 1} \times \mathbf{b}_{\parallel}$. The total perpendicular basis vector is written as $\mathbf{b}_{\perp} = \cos \alpha \mathbf{b}_{\perp 1} + \sin \alpha \mathbf{b}_{\perp 2}$. Here, the gyrophase α describes the initial particle position on the gyro plane which is perpendicular to the field line.

As shown in Fig. 3.1, the velocity is half a time step back as the leapfrog scheme is staggered. The integrator is initialised by the position at the “0” time step and the velocity at the “-1/2” time step.

Using vector basis \mathbf{b}_{\parallel} and \mathbf{b}_{\perp} , the initial velocity can be written as $\mathbf{V} = v_{\parallel} \mathbf{b}_{\parallel} + v_{\perp} \mathbf{b}_{\perp}$ with v_{\parallel} and v_{\perp} to be determined. The total velocity is given by the particle kinetic energy $v = \sqrt{2mE}$ and the parallel component is given by the initial pitch $\lambda = v_{\parallel}/v$. Consequently, the particle velocity is expressed in terms of initial E and λ , $\mathbf{V} = \sqrt{2mE}(\lambda \mathbf{b}_{\parallel} + \sqrt{1 - \lambda^2} \mathbf{b}_{\perp})$ with m the particle mass.

3.4 Workflow of the particle pushing code

It is straightforward and convenient to generate simulation markers by means of seed values $(R, \phi, Z, E, \lambda, \alpha)$, which intuitively describe a particle’s physical location in the fusion device, type (passing or trapped) and energy of interest. As discussed in section 3.2 and 3.3, they are converted to the position and velocity in Cartesian coordinates (X, Y, Z, v_x, v_y, v_z) which are required by

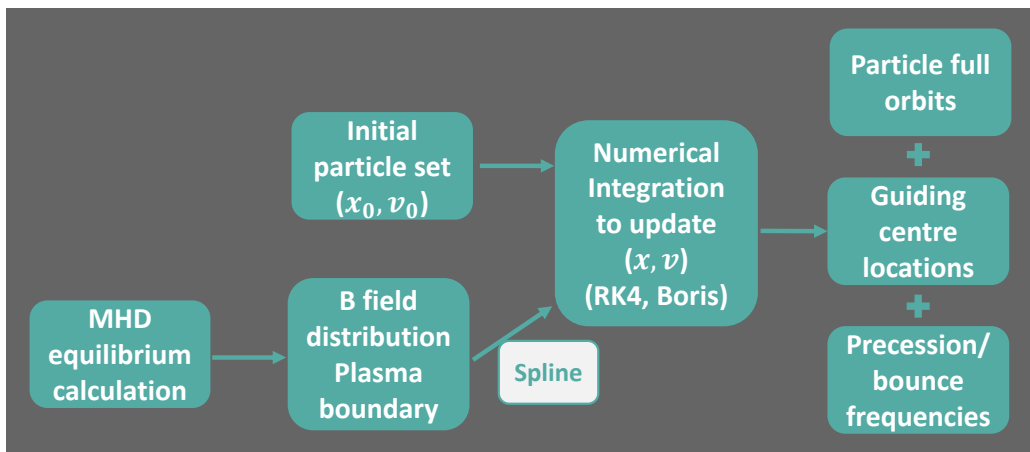


Figure 3.3: Flowchart to summarise the steps of solving the Lorentz equations of a charged particle in an equilibrium magnetic field.

the numerical integration with the Boris method. A spline **FORTRAN** library [81] is used to interpolate the data of the poloidal flux surface function ψ reconstructed by the **EFIT++** code and the equilibrium magnetic field for a given location. The interpolation is realised by a set of cubic polynomials between knots and the coefficients of the polynomials are determined by the continuity conditions of the first and second order derivatives at the knots. Fig. 3.3 is a flowchart to summarise the steps of the particle pushing code. The full orbit simulations can produce a series of particle information, including particle trajectories, temporal evolution of the velocities, guiding centre locations, poloidal and toroidal motion frequencies etc.

3.5 Code validation

The numerical code is validated by following the exact orbit of a test particle in a uniform magnetic field. This classical model of the single particle motion has been discussed in detail in section 2.1.1 so the analytical solutions are at hand and can be used as a benchmark of the numerical results.

The parameters used in the calculation are chosen to be of the same

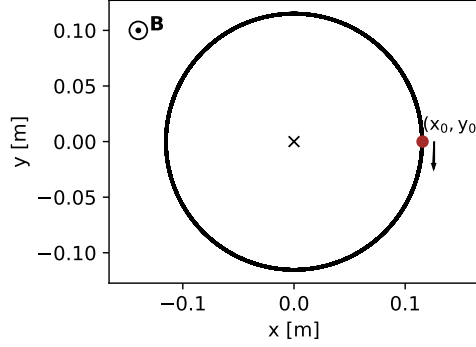


Figure 3.4: The constant \mathbf{B} field is along the z direction and the computational trajectory of a deuterium ion on $x - y$ plane is a closed circle.

order as given by the MAST operation. First, the constant magnetic field $B = B_z = 0.5$ T is set be along the z direction where general Cartesian coordinates x, y, z are considered. Here the strength of the field of 0.5 Tesla is a typical value of the toroidal magnetic field at the magnetic axis in MAST. Then, a deuterium ion is launched with an energy of 80 keV corresponding to the highest injection energy of the beam on MAST. The initial velocity is given by assuming that the energy comes from one perpendicular dimension \mathbf{e}_y only for simplicity and we have $v_{y0} = -2.77 \times 10^6$ m·s⁻² and $v_{x0} = v_{z0} = 0$ with a deuterium mass $m_D = 3.3435 \times 10^{-27}$ kg. The gyro radius can be obtained by $r_c = m|v_\perp|/qB \approx 0.116$ m. We then set the initial location of the particle as $x_0 = r_c$ and $y_0 = z_0 = 0$. Because the rotation is in the diamagnetic direction, the trajectory of the test marker on the perpendicular plane should be a perfect circle whose the centre is located at $x = 0$ and $y = 0$.

The simulation results are illustrated in Fig. 3.4 and 3.5 showing a good agreement with the theoretical predictions just presented. In Fig. 3.4 the particle full orbit is projected on the $x - y$ plane where the direction of \mathbf{B} is along the outward normal to the plane. The particle starts from the location

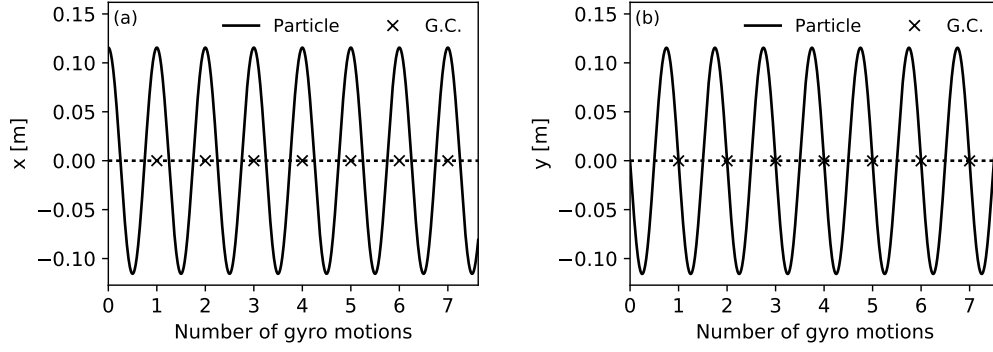


Figure 3.5: (a) x and (b) y dimension of the circular gyro orbit.

(x_0, y_0) and rotates clockwise around the origin with a constant radius. Fig. 3.5 shows the motions in x and y dimensions. The oscillations of the curves separately obey the expected sine and cosine functions. Here the number of gyro motions N_{gyro} that the particle has completed can be deduced from the number of the sine or cosine waves k during the tracking time, specifically, $N_{\text{gyro}} = k$.

The estimated location of the guiding centre (G.C.) \mathbf{r}_{gc} is numerically evaluated by averaging the particle position \mathbf{r}_i over one gyro period T :

$$\mathbf{r}_{gc} = \frac{1}{T} \int_0^T \mathbf{r} dt \approx \frac{1}{T} \sum_{i=1}^n \frac{(\mathbf{r}_i + \mathbf{r}_{i+1})}{2} \Delta t, \quad (3.26)$$

where the trapezoidal rule is applied for approximating the integration. As shown in Fig. 3.5, \mathbf{r}_{gc} is well maintained at $x_c = 0$ and $y_c = 0$ as expected for the average of sine or cosine functions. The evaluation can be extended to find the G.C. of the orbit in a magnetic field that is not analytically defined. In such cases, the gyro motion can still be decomposed into harmonic motions but the amplitude of the oscillation is normally a function of time and space because of drift motions.

The stability of the numerical code is tested by examining the conservation of the particle kinetic energy E_k . The test marker has been tracked for 5 ms corresponding to 5×10^7 iterations in the program with time step

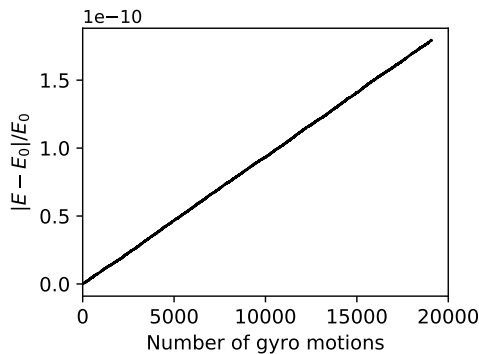


Figure 3.6: Negligible energy variation during the particle tracking.

$dt = 1 \times 10^{-10}$ s. As can be seen in Fig. 3.6, the variation in E_k is only on the order of 10^{-10} after 15,000 gyro motions. The double precision data type is used so that rounding errors can be reduced in the numerical results.

3.6 Calculations of particle orbits in MAST

The motivation for the particle pushing code is to calculate the particle orbits in MAST with a toroidal magnetic configuration. The equilibrium field reconstructed by the EFIT++ code for the experiment discharge #29210 is used throughout this section to demonstrate the typical orbits in MAST. Test markers are deuterium ions with energy of 15 keV, toroidal angle $\phi = 0$, and gyro angle $\alpha = 0$ and the specification of the test particle initial conditions (R, Z, λ) will be declared separately for each case developed.

In general, particles that can be confined in a tokamak fall into two categories: passing and trapped particles. Trapped particles are particles that are mirror trapped on the outboard side of a tokamak and oscillate between bounce tips where $v_{\parallel} = 0$. A trapped particle orbit is also commonly referred to as a banana orbit due to the fact that the poloidal projection of the orbit resembles a banana shape. Particles whose v_{\parallel} is never zero along

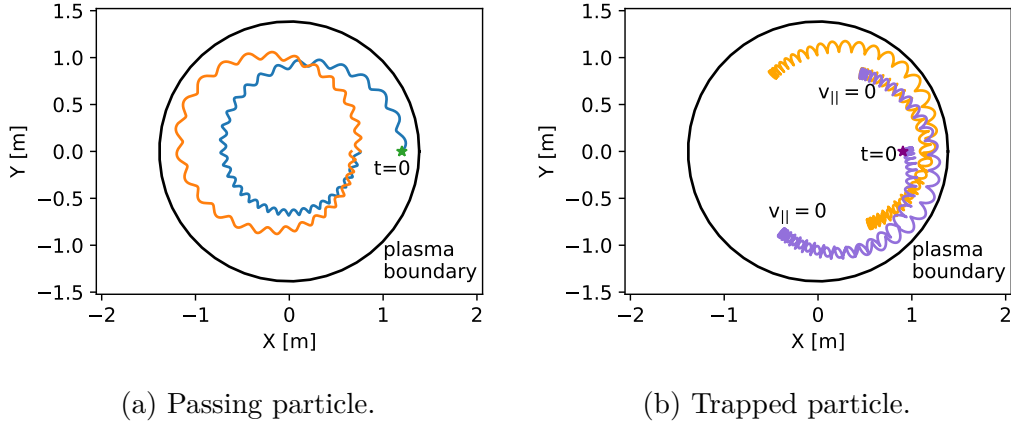
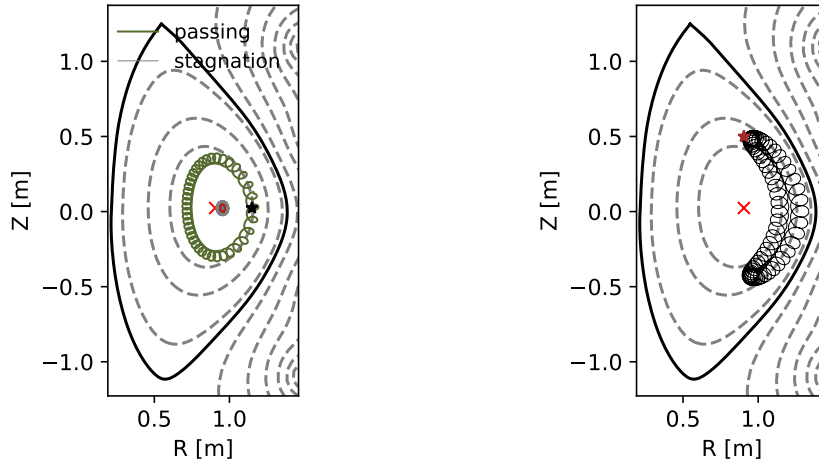


Figure 3.7: Top view of the tokamak showing the toroidal projections of different types of particle orbits, where $X = R \cos \phi$ and $Y = R \sin \phi$.

the trajectory are denoted as passing particles. The toroidal projections of these two kinds of particles are shown in Fig. 3.7. Recall that $\mu = E_{\perp}/B$ is an adiabatic invariant. The trapped particle gains E_{\perp} from E_{\parallel} to maintain the conservation of μ as well as the total energy as it approaches a high field region. When E_{\parallel} is completely transferred to E_{\perp} , the motion along the field line is reversed so the particle behaves as if it is trapped in these two fixed locations where the magnetic field achieves a maximum value B_{\max} and $v_{\parallel} = 0$.

The poloidal projection of a passing particle orbit with $|\lambda| = 1$ is shown in Fig. 3.8a. The orbit encircles the magnetic axis labelled with a red cross and completes a circular-like trajectory almost aligned with the shape of the flux surface. The deviation is due to the cross field drift velocities discussed in section 2.1.3 and 2.1.4. Fig. 3.8a depicts poloidal projections of passing particle orbits. The equilibrium flux surfaces are denoted with dashed lines while the LCFS is marked with a solid black line. In Fig. 3.8b the trapped particle with $|\lambda| = 0$ traces out a banana-shaped orbit. In contrast to the passing particle, the trapped particle stays on one side of the magnetic axis.

A non-standard passing orbit referred to as a stagnation orbit [82] is



(a) Passing particle and stagnation orbit.

(b) Trapped particle.

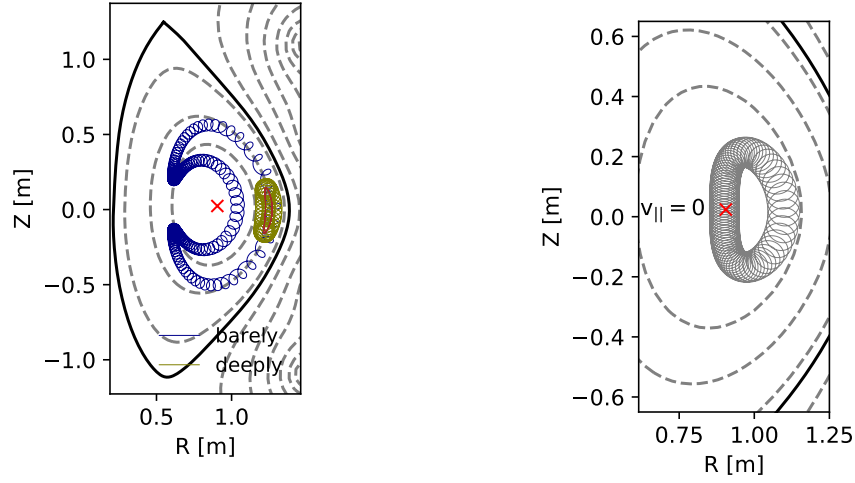
 Figure 3.8: Poloidal projections of particle orbits. Markers \star show the initial particle positions.

also illustrated in Fig. 3.8a. The particle is resident near the magnetic axis and orbits the torus centre. From the poloidal view, it appears to stop at a single point on the cross section. This is because the magnetic field is purely toroidal at the magnetic axis so both the ∇B and curvature drift motions of this particle are nearly vertical. The vertical drifts can be cancelled out because of the symmetry in the equatorial plane, which leads to a stagnation orbit.

Particles that are trapped in a small and narrow region at the low field side are referred to as deeply trapped particles. The orbit of a deeply trapped particle is shown in Fig. 3.9a. Two bounce points are close to the initial location of the particle so $B_{\max} \approx B_{\min}$, the poloidal angle $\theta \approx 0$ and $\sin \theta \approx 0$, where θ is given by

$$\tan \theta = \frac{Z}{\sqrt{R^2 - Z^2 - R_0}}. \quad (3.27)$$

Those particles that can travel a longer distance and nearly complete a closed circle in the poloidal plane before changing the direction of the parallel motion are generally called barely trapped particles. An example is plotted in blue



(a) Barely (blue) and deeply trapped (green) particles.

(b) Potato orbit.

Figure 3.9: (a) Deeply and barely trapped particle orbits. Both the full orbit and the G.C. orbit of the deeply trapped particles are illustrated. (b) A potato orbit whose bounce point is on the magnetic axis marked with the symbol \times .

line in Fig. 3.9a .

Potato particles are trapped particles with a broader orbit. Fig. 3.9b shows a potato orbit passing through the magnetic axis at a parallel velocity $v_{||} = 0$. After leaving the magnetic axis, the particle moves to the low field region without changing the sign of $v_{||} = 0$. Potato particles can be considered as the transitions between passing particles and trapped particles.

Both trapped and passing particles are confined in the tokamak. Those that cannot be confined by the magnetic field are referred to as lost particles. The confined-lost domain is defined by the LCFS in the simulation. If a particle travels outside the LCFS, mathematically when the normalised poloidal flux function $\psi_n > 1$, it will be considered lost. Fig. 3.10a shows an example of a lost particle. The guiding centre locations of this particle remain inside of the LCFS but it has reached the boundary at the low field side. Therefore, the particle is classified as a lost particle. The full orbit simulation

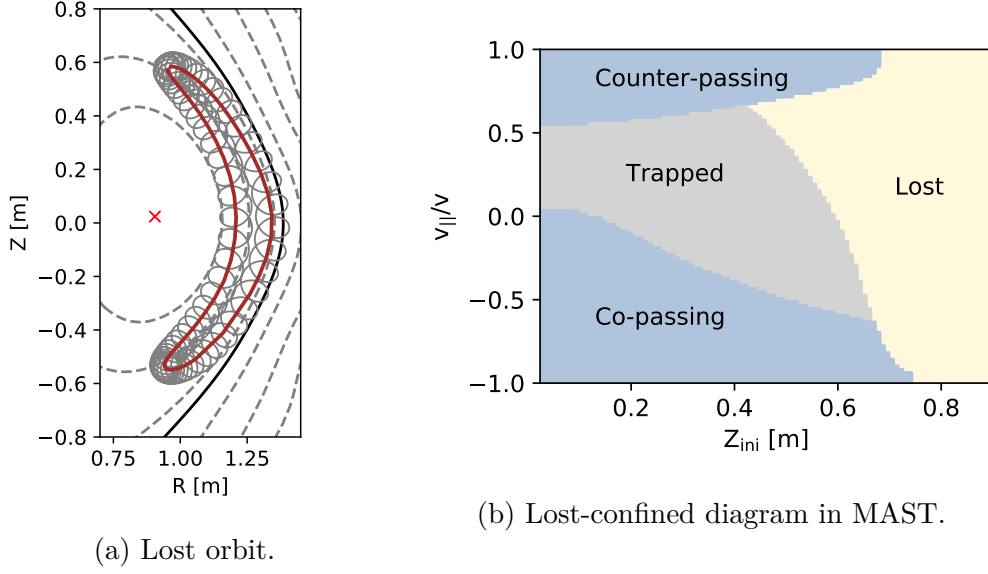
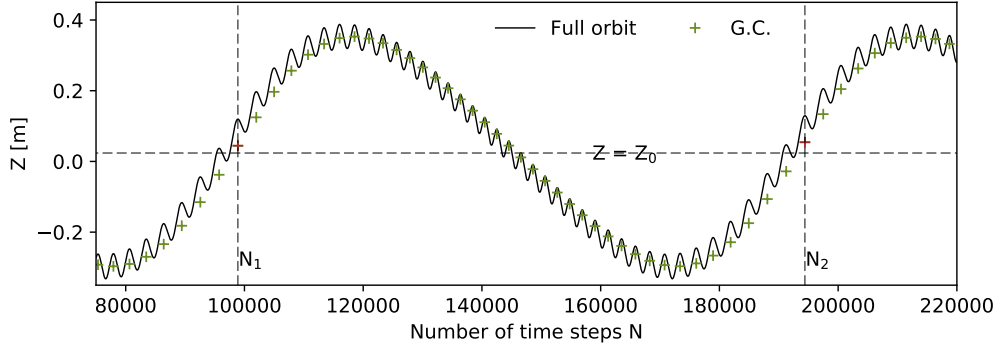


Figure 3.10: (a) An example of a lost orbit whose the G.C. position maintains confined but the full orbit is beyond the confined boundary; in the simulation, the lost boundary is defined as $\psi_n = 1$ corresponding to the black solid line. (b) Plane of Z_{ini} , $\lambda = v_{\parallel}/v$ with $E = 15$ keV, showing domains of confined and lost particles in MAST.

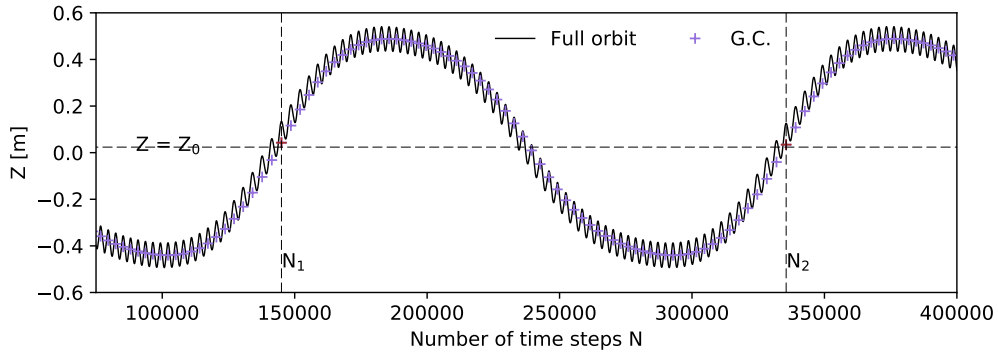
places a more strict condition to confine a particle and hence increase the lost domain. Fig. 3.10b demonstrates a computed lost-confined region for MAST plasmas. In the MAST convention, the toroidal component of the magnetic field is in the counter-current direction so passing particles with $v_{\parallel} > 0$ and $v_{\parallel} < 0$ are referred to as counter- and co-passing particle, respectively.

3.7 Calculations of motion frequencies

Charged particles in a tokamak undergo periodic motions both in the poloidal and toroidal dimensions. The motion frequencies can be computed while particles are tracked in the program. In the poloidal direction, the motion period is calculated by timing when the particle passing through the vertical position of the magnetic axis $Z = Z_0$. As shown in Fig. 3.11, the particle oscillates around the $Z = Z_0$ plane in the full orbit simulation, which makes



(a) Passing particle



(b) Trapped particle

Figure 3.11: Calculations of the poloidal frequencies f_θ by timing a particle passing through the $Z = Z_0$ plane. f_θ is given by $f_\theta = 1/(\Delta N dt)$ where dt is the time interval.

it difficult to track the accurate time when it actually arrives/leaves this location. However, the guiding centre of the particle passes the $Z = Z_0$ plane only twice (inboard and outboard) to complete a poloidal circle and hence can be used to compute the poloidal motion frequency f_θ , given by

$$f_\theta = \frac{1}{\Delta N dt}, \quad (3.28)$$

where dt is the time interval. $\Delta N = N_2 - N_1$, N_1 and N_2 are the number of time steps when the particle makes its first and second passes through the $Z = Z_0$ plane, respectively.

As a passing particle transits around the torus, its toroidal angle coordinate ϕ varies between $-\pi$ and π as shown in Fig. 3.12a. The toroidal

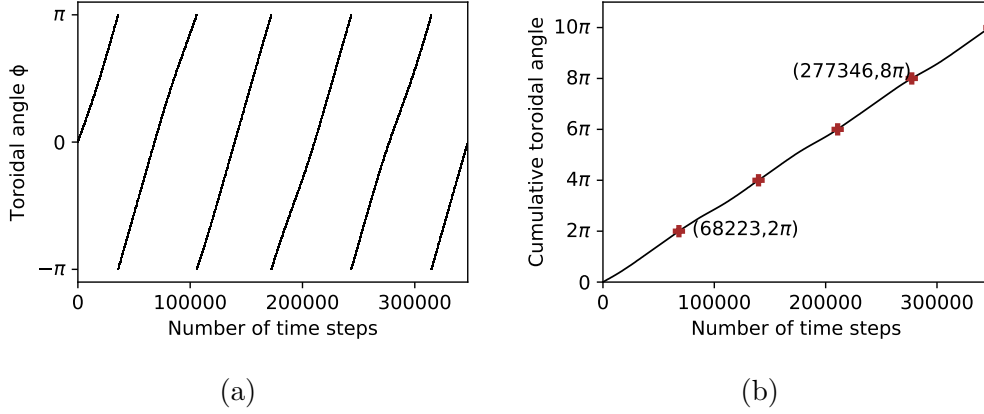


Figure 3.12: (a) Temporal evolution of the toroidal angle ϕ of a passing particle; ϕ periodically changes between $-\pi$ to π . (b) Cumulative toroidal angle derived from ϕ is a monotonic function of time.

motion frequency f_ϕ can be obtained by constructing a monotonically increasing quantity, the cumulative toroidal angle φ , given by $\varphi = \phi - \phi_0$, where ϕ_0 is the particle initial toroidal angle. φ is corrected by 2π every time the particle passes through the discontinuous boundary, that is,

$$\begin{cases} \varphi = \varphi + 2\pi, & +\pi \rightarrow -\pi; \\ \varphi = \varphi - 2\pi, & -\pi \rightarrow +\pi. \end{cases} \quad (3.29)$$

The temporal evolution of φ derived from ϕ is illustrated in 3.12b. The toroidal frequency f_ϕ is given by

$$f_\phi = \frac{\varphi}{2\pi N dt}, \quad (3.30)$$

where dt is the time step and N the number of time steps. N is recorded when φ passes a multiple of 2π as illustrated in table 3.1. The full orbit calculation leads to an error of up to one gyro period in the estimation of the toroidal motion period. Therefore, f_ϕ is averaged over multiple complete toroidal motions and the variation of f_ϕ reduces as the tracking time increases.

This method of calculating f_ϕ is especially necessary for trapped particles. The profiles of the toroidal angle ϕ and the cumulative toroidal angle φ of

| φ | N | f_ϕ [kHz] |
|-----------|--------|----------------|
| 2π | 68223 | 146.58 |
| 4π | 139722 | 143.14 |
| 6π | 210800 | 142.31 |
| 8π | 277346 | 144.22 |
| 10π | 347153 | 144.03 |

Table 3.1: Data from the simulation results used to calculate the toroidal motion frequency f_ϕ of a passing particle (time step $dt = 1 \times 10^{-10}$).

the trapped particle in Fig. 3.8b are demonstrated in Fig. 3.13. Because a trapped particle will change the direction of $v_{||}$ in one bounce motion, the toroidal coordinate ϕ may oscillate near the $\pm\pi$ boundary multiple times so ϕ cannot be used in the calculations of f_ϕ . However, the precession angle can be calculated by constructing the functions of the cumulative toroidal angle φ similar to those of passing particles. Trapped particles may only occupy a small part of the torus in many situations since the precession is cancelled out by the opposite motion along the field line in one bounce motion. f_ϕ for a trapped particle is therefore defined by

$$f_\phi = \frac{\Delta\varphi}{2\pi\Delta t}, \quad (3.31)$$

where $\Delta\varphi$ is the precession angle within one or several bounce motions and Δt is the elapsed time. As shown in Fig. 3.13b, data of N and φ are collected when the particle passes through the $Z = Z_0$ plane which allows the precession angle $\Delta\varphi = \varphi_2 - \varphi_1$ and precession frequency f_ϕ to be calculable.

The approaches used to calculate the poloidal and toroidal motion frequencies can be extended to non-standard orbits. Stagnation orbits are classified as passing orbit types as they can rapidly travel around the torus. Potato orbits are considered as trapped orbits because of the reversed parallel motions.

Stochastic errors of up to one gyro period are introduced into the calcu-

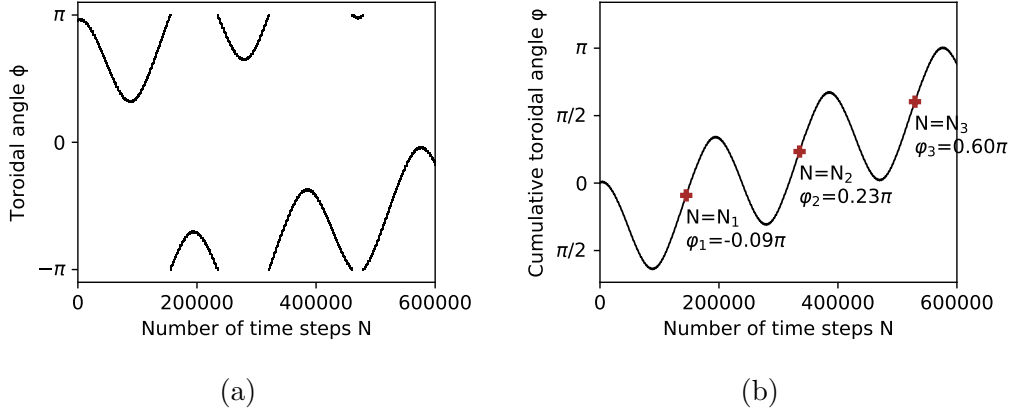


Figure 3.13: (a) Temporal evolution of the toroidal angle ϕ of a trapped particle; (b) Cumulative toroidal angle derived from ϕ . Toroidal frequency $f_\phi \approx (\phi_2 - \phi_1)/[2\pi(N_2 - N_1)dt] \approx (\phi_3 - \phi_1)/[2\pi(N_3 - N_1)dt]$.

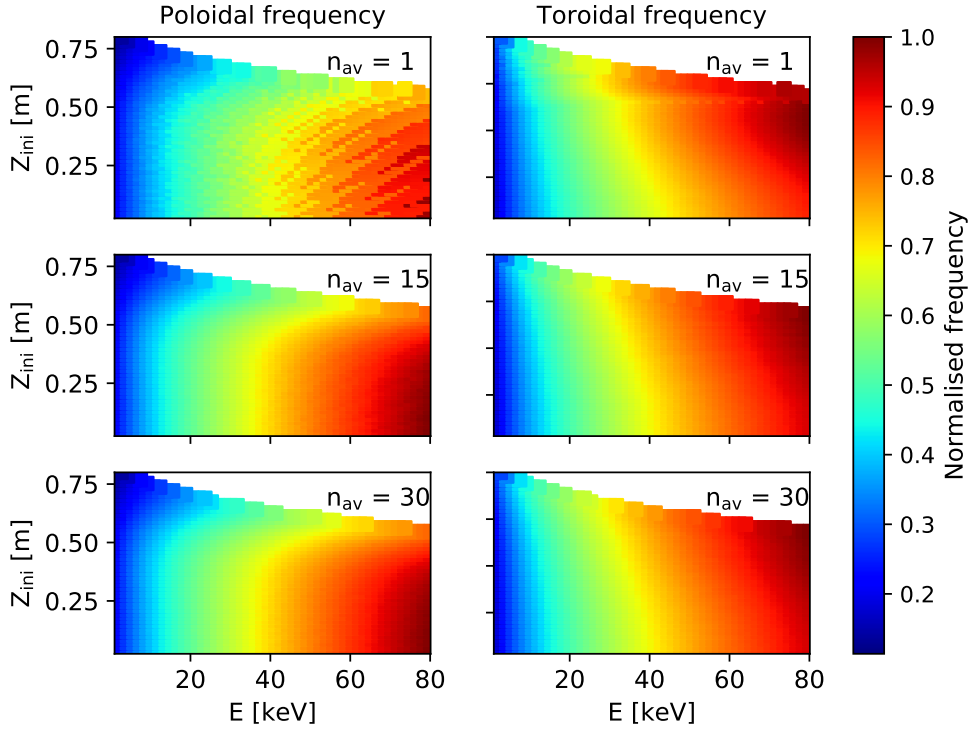


Figure 3.14: Orbit averaging in the calculations of poloidal and toroidal frequencies. The computational noise reduces as the number of orbit averaging increases.

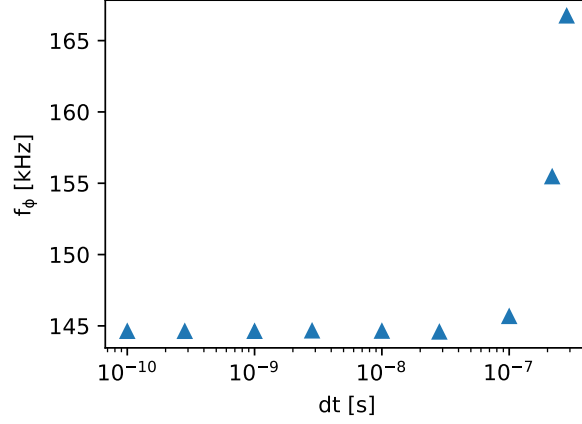


Figure 3.15: The toroidal frequency of a passing particle converges as dt reduces. The particle with $\lambda = 0.75$ is launched from $R = 1.0$ m and $Z = Z_0$.

lations of f_θ and f_ϕ because of the full orbit simulations and gyro averaging. As can be seen in Fig. 3.14, simulation results for frequencies are messy and unstructured with stochastic errors when only considering one complete poloidal or toroidal orbit corresponding $n_{av} = 1$. As the number of orbit averaging n_{av} increases, the profiles of f_θ and f_ϕ are smoothed out as they converge and regress to the mean.

The Boris algorithm is second-order accurate [80], and the choice of the integration time step is often a trade-off between computational time and accuracy. It is convenient to choose the time step as a fraction of the gyro-periods of particles in the simulation. In Fig. 3.15, the toroidal motion frequency of a passing particle is computed using Eq. 3.31 with different time steps where the particle with $\lambda = 0.75$ is launched from $R = 1.0$ m and $Z = Z_0$. The toroidal motion frequency f_ϕ is converged to 144 kHz as the time step dt reduces. For the particle trajectories demonstrated in this chapter, dt is set to be 10^{-10} s so that particles with short gyro periods which require small time steps can be simulated correctly.

3.8 Summary

A full orbit particle pushing code has been developed using the Boris method. The coordinate transformations between the Cartesian and commonly used cylindrical system are discussed. The transform matrices are obtained and implemented in the code. The code is validated against an analytic solution of the gyro-motion of a charged particle in a constant magnetic field. The code is then extended to calculate the particle trajectory in a realistic magnetic field. A method is found to efficiently evaluate the poloidal and toroidal motion frequencies as the full orbits of particles are followed. Since the particle periodic frequencies can be determined numerically, the resonant particles will be easily found based on the wave-particle resonance condition. In the next chapter, the code is used to evaluate the resonance condition for particles in MAST experiments with MHD modes.

Fast-ion driven modes

We have shown in the previous chapter how to determine the particle motion frequencies in a realistic magnetic field. We will now use the calculated frequencies to derive resonance maps for the interaction of wave fields in plasmas with fast particle populations. Such maps can aid greatly in the interpretation of the underlying fast particle transport mechanisms in plasmas with waves and instabilities. As a demonstration of this, in this chapter we focus on MAST shot #29210 which exhibits large chirping TAEs, fishbones and a long-lived mode. We will show that resonance maps for this shot can provide valuable insights into the physics of these processes which can aid interpretation of experimental results. We begin by presenting the experimental discharge for analysis.

4.1 Plasma scenarios

A set of discharges [61, 62] have been performed to excite instabilities and study the consequent fast ion behaviour affected by these MHD events on MAST by means of the NBI. The NBI is primarily responsible for heating and driving current so that the plasma temperature and current can be raised

to expected levels. The applied deuterium beams have energies of up to 75 keV (equivalently, 2.7×10^6 m/s) and they are super-Alfvénic. The Alfvén speed $v_A = B/\sqrt{\mu_0(m_i n_i + m_e n_e)} \sim 7.7 \times 10^5$ m/s where B is the magnetic field strength on the magnetic axis, typically $B_0 \sim 0.5$ T and the number density $n_i = n_e \sim 10^{20}$ m $^{-3}$ for MAST plasmas. Therefore, the NBI is also the source of the energetic population providing free energy so the plasmas are destabilised. The discharge #29210 is one of the experiments which investigated Alfvénic instabilities using this approach. Fig. 4.1 demonstrates the time trace of key parameters of this discharge. The SS beam is turned on at 50 ms for a total time of 400 ms while the SW beam is switched on at $t = 180$ ms. The two beam injectors are capable of delivering heating at separate energies. The SS and SW beam powers are 2.0 MW and 1.5 MW, respectively. The plasma current I_p ramps up to 0.9 MA with the beam injection and maintains a stable state for 100 ms before it disrupts. The periodic bursts in Mirnov coil signals indicate a series of MHD activities take place. The data from the Mirnov coils are then analysed by means of Fourier decomposition as shown in the spectrogram in Fig. 4.2. Throughout the discharge, MHD modes with frequencies in the range of 0-150 kHz are observed. The mode analysis is given in Fig. 4.2 (b), showing the toroidal mode number for each individual harmonic and dominant modes with $n = 1 \sim 3$ are identified. At 140 ms, $n = 1$ TAEs with strong down chirping frequencies near 80 kHz are excited. They later develop into stronger $n = 1$ fishbone oscillations at lower frequencies around 40 kHz after 180 ms. The discharge ends up with discrete saturated kink modes with constant frequency until it quenches.

Such instabilities could induce large particle losses across the field lines and greatly degrade the heating efficiency of the beams. These can be first identified from the estimations given by the EFIT++ simulation results. As

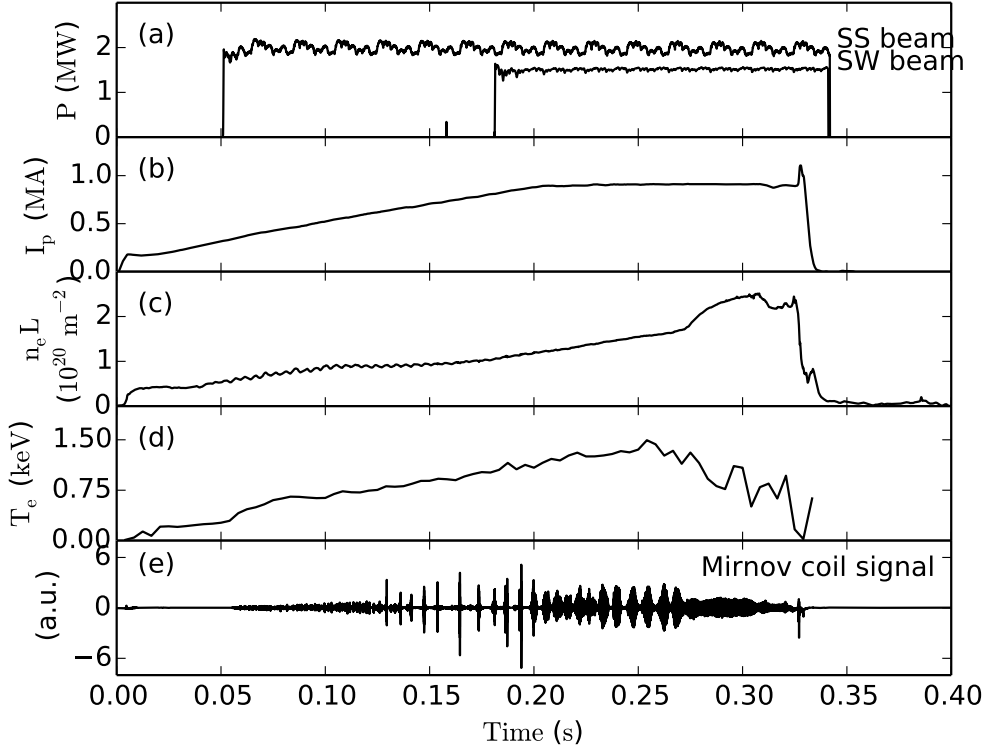


Figure 4.1: Time trace for MAST discharge #29210. (a) NBI power, (b) plasma current, (c) line integrated electron density, (d) electron temperature at core, (e) Mirnov coil signals for instability analysis.

discussed in section 2.3, the EFIT ++ code can reconstruct the plasma equilibrium which both satisfies the GS equations (2.55) and experimental constraints. As shown in Fig. 4.3, the pressure estimated by the EFIT++ increases with the beam injection but grows with the beam power disproportionately. As the addition of the SW beam raises the total beam power by approximately 75% ($2 \text{ MW} \rightarrow 3.5 \text{ MW}$), the normalised on-axis pressure p_0/p_{atm} goes up by $\sim 50\%$ ($0.12 \rightarrow 0.18$).

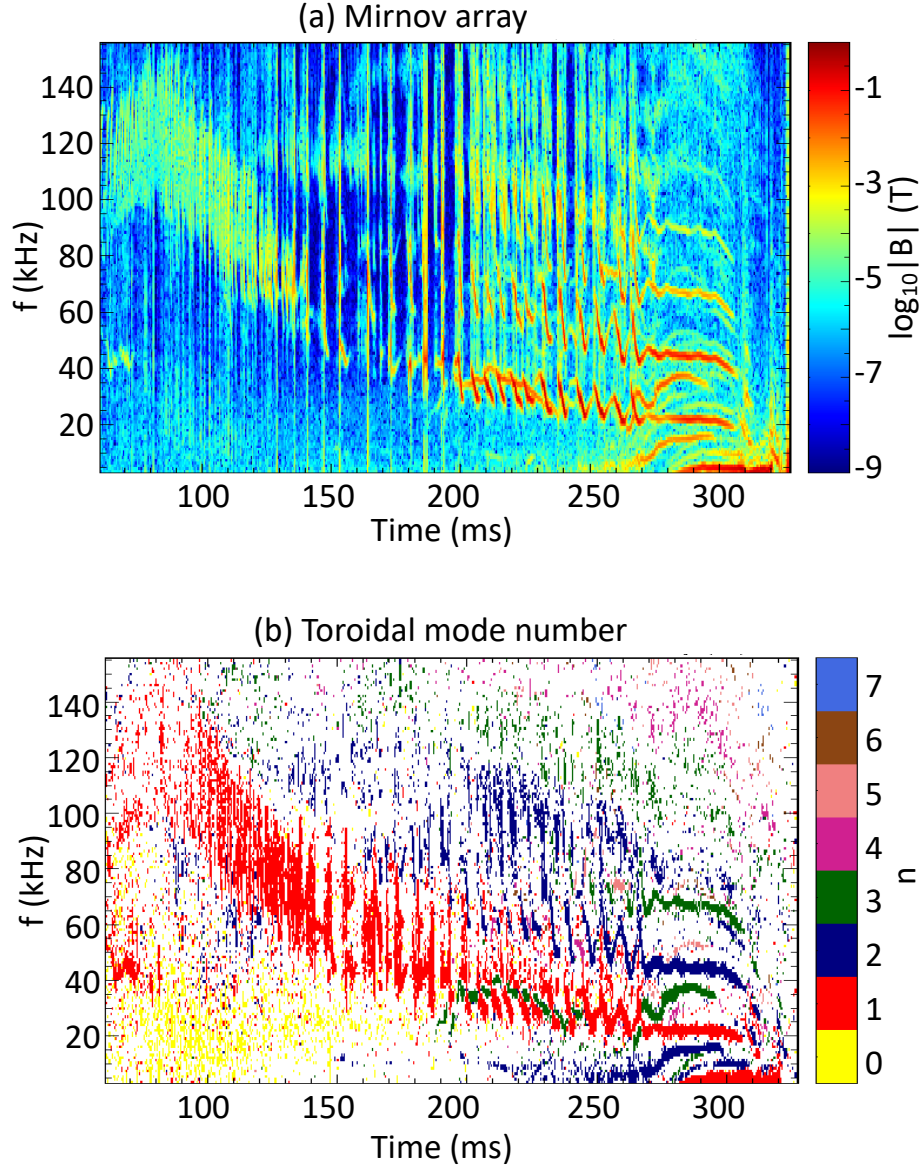


Figure 4.2: (a) The frequencies of MHD bursts and (b) toroidal mode number of the chirping modes are given in the spectrum of the magnetic perturbations during beam injection.

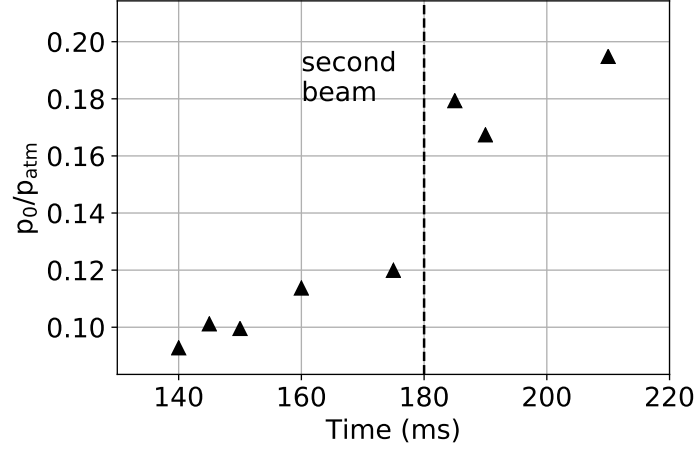


Figure 4.3: On-axis pressure p_0 evaluated using EFIT++ show the changes in plasma equilibria as the second beam is turned on. p_0 is normalised by the atmospheric pressure p_{atm} .

4.2 FIDA diagnostics

Experimentally, the radially resolved information about the fast ion density and its distribution can be inferred by a fast-ion deuterium alpha (FIDA) spectrometer[83]. A diagram illustrating the geometry of this diagnostic on MAST is shown in Fig. 4.4. On MAST, the FIDA shares the viewing optics of the charge exchange recombination spectroscopy which is used for the ion temperature and flow measurements. As a fast ion in the plasma captures an electron from a beam neutral, the resulting fast neutral can be in an excited state which then radiates D_α photons and this is what the toroidal (tangential) and vertical (perpendicular) FIDA fiber arrays measure. The light from the fast neutral is Doppler shifted based on the speed of the fast neutral along the line of sight of the diagnostic and this gives velocity space information. The fast ion distribution function $f(E, \lambda, R, Z)$ is linked with FIDA measured signals S via a constructed weight function $w(E, \lambda, R, Z)$ [84,

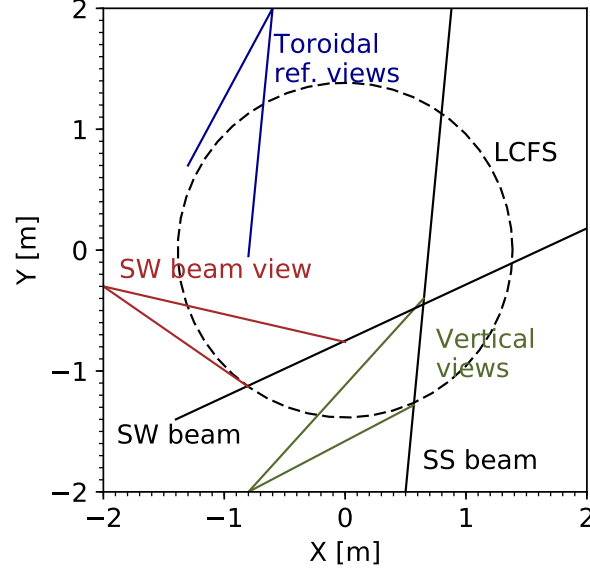


Figure 4.4: Top view of the MAST showing the toroidal projections of the FIDA vertical and toroidal reference views, together with the NBI beamlines [83].

85]:

$$S = \int (w \times f) dE d\lambda dR dZ. \quad (4.1)$$

Fig. 4.5 shows the dependence of the weight function on radial position R for the toroidal line of sight FIDA diagnostic. The system is sensitive to particles above 45 keV with a peak in the weight function located at $|\lambda| \sim 1$ for all energies.

Experimental FIDA measurements are illustrated in Fig. 4.6 for discharge #29210. D_α emission from the mid-plane is integrated over (E, λ) space giving the temporal evolution of the radial profile of the radiance. Integrated signals have shown that at $R \sim 107$ cm, observed reductions in FIDA signal intensity are strongly correlated with the MHD bursts during 140 - 210 ms. Sudden increases in signal intensity from edge views are also detected after each massive reduction in the core. The lost fast ion signal is produced by the interaction with edge neutrals. This appears in both the active and passive

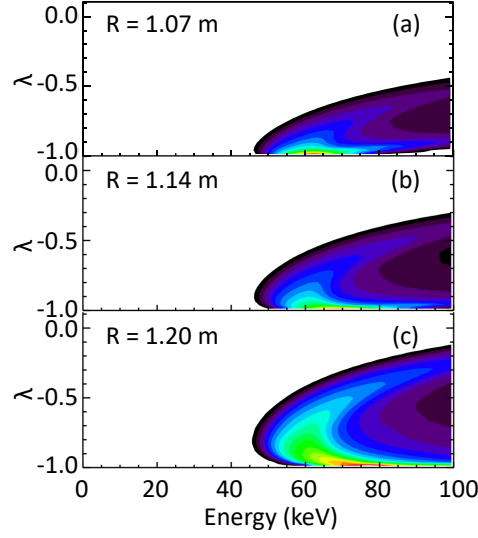


Figure 4.5: Weight function of the toroidal line of sight FIDA system at three locations: $R = 1.07$, 1.14 and 1.20 m, where the minimum energy $E_{\min} = 45$ keV. Only ions in the coloured region in velocity space can contribute to the measured FIDA signal. The brightness of the colour scales the sensitivity of particles to the FIDA diagnostic, implying that a charge exchange reaction is more likely to take place at $\lambda = -1$.

views. In principle, it should be possible to subtract this out, however a small error in the relative calibration of an active channel and its corresponding passive channel, by a small amount, e.g. 10%, could lead to a significant residual "unsubtracted" component of this lost fast ion/edge neutral emission. This edge passive emission is present in all channels, but is weaker for channels viewing closer to the core, because the amount is weighted by the angle between the line of sight and the flux surface. For core viewing channels, the line-of-sight intersects edge flux surfaces with a large angle, whereas the edge channels intersect the surfaces more tangentially, i.e. at a smaller angle. This results in a smaller contribution to the total signal intensity from lost fast ions, and thus a more reliable signal for the core channels than the edge channels. These measurements suggest that fast ions with minimum energy $E_{\min} = 45$ keV could be expelled due to the chirping modes. We will next

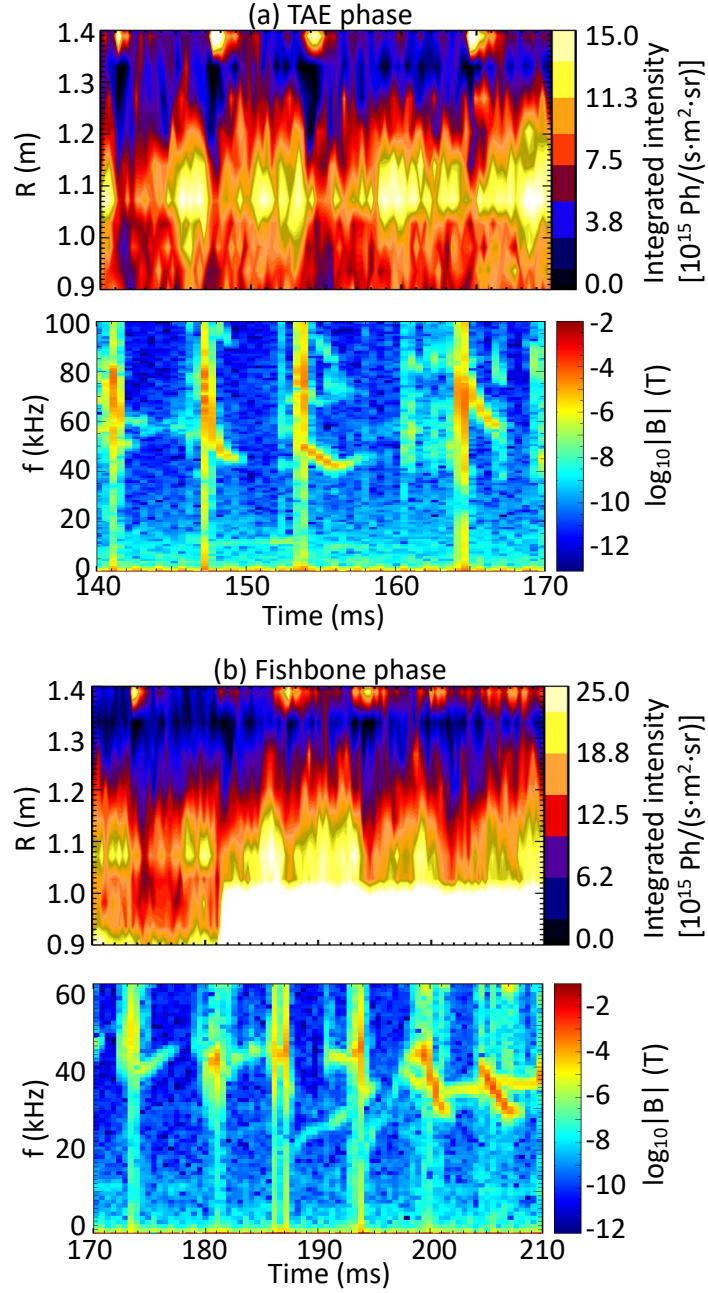


Figure 4.6: Marked drops in FIDA radiance are correlated with visible MHD bursts at 140 ms, 147 ms, 155ms, 173ms, 194 ms and 200 ms.

investigate the behaviour and transport of the fast ions that are responsible for driving the MHD modes.

4.3 Calculations of resonance maps

We now perform full orbit tracking by solving the exact equations of motion in an equilibrium magnetic field calculated using EFIT++ as discussed in chapter 3. Full orbit equations provide more accurate calculations of the motion frequencies than the guiding centre equations due to the large Larmor radii of fast particles in the low toroidal field of the spherical tokamak. It is for this reason that guiding centre codes cannot be expected to correctly track particles with high energies in MAST. A comparison between guiding centre and full orbit schemes for MAST spherical tokamak has been made in previous studies [86, 87] showing that an overestimate in the neutron rate arises when guiding centre calculations are used.

Test particles are populated on uniform energy E and pitch $\lambda = v_{\parallel}/v$ grids at $R = 107$ cm and $Z = 0$ corresponding to the location where large particle losses are seen in the FIDA signal. The poloidal and toroidal orbit frequencies of the test particles are estimated as they are tracked in the simulation and substituted into Eq. (2.137) to identify the resonant particles. The linear resonance condition is investigated for varying mode frequency as observed during a chirp. Resonance maps between $n = 1$ chirping modes and particles are presented in Fig. 4.7. Shot times $t = 150$ and 205 ms are chosen such that TAEs and fishbones respectively are dominant and produce transport of fast ions. The chirping modes to be excited are in the range 60-30 kHz and 40-10 kHz for 150 and 205 ms, respectively. This is consistent with what has been observed in Fig. 4.2. Passing particles with energies up to 80 keV can interact with the mode via the $p = -1$ resonance. The fishbone is expected to have dominant poloidal mode number $= -1$, implying that this choice of p resonance where FIDA is sensitive, also corresponds to $k_{\parallel} \cdot v_{\parallel} \sim \omega$.

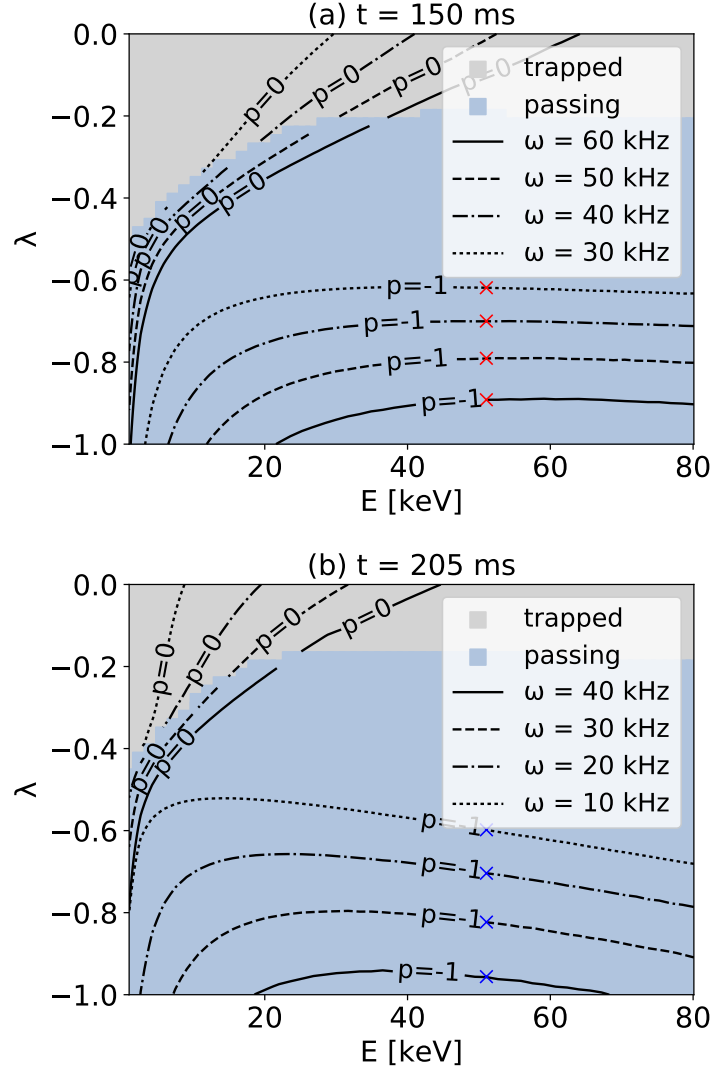


Figure 4.7: Resonance maps identifying particles that can interact with $n = 1$ chirping modes at (a) $t = 150$ and (b) $t = 205$ ms. 100×100 test markers are populated at $R = 107$ cm and $Z = 0$ cm. Chirping frequencies are sampled within the range observed. Possible mathematical solutions to the resonance condition are illustrated in the graphs. Passing and trapped particles are plotted but there are no lost particles since the initial location is close to the core.

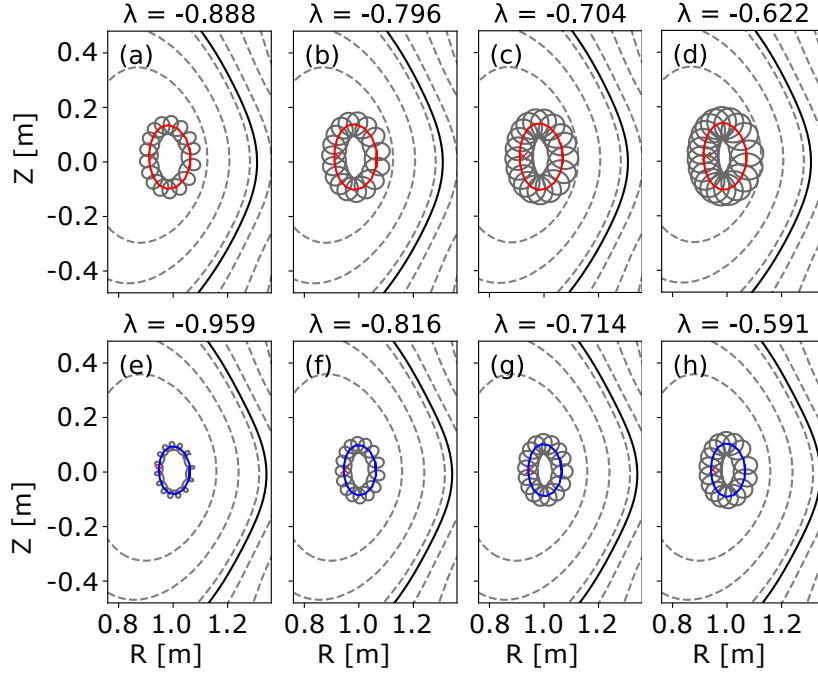


Figure 4.8: Orbits of the resonant particles labelled with red and blue crosses in the resonance map showing in Fig. 4.7 at $E = 50$ keV.

As the mode frequency decreases, the $p = -1$ resonance moves towards lower values of $|\lambda|$. Particles at 50 keV marked with red and blue crosses in Fig. 4.7 are chosen as examples to demonstrate the dependency of the particle orbit on pitch. As illustrated in Fig. 4.8 (a) - (h), the orbits of the resonant particles tend to expand outwards and Larmor radius ρ rises with decreasing $|\lambda|$, which is consistent with the relation

$$\rho \sim (1 - \lambda^2)^{1/2} \cdot (2mE)^{1/2}/qB, \quad (4.2)$$

which is derived from the definition of the magnetic moment $\mu = mv_{\perp}^2/2B$.

The strength of the wave-particle interaction is a function of p and $p = -1$ gives resonances that lie within the region of the fast ion phase space accessible with the FIDA diagnostic. Trial values of p ranging from -100 to 100 have been examined in the simulation and another branch of resonance, $p = 0$, can be found as shown in Fig. 4.7. The $p = 0$ resonance represents the particles

for which the toroidal precession frequency matches the mode frequency for the $n = 1$ mode. These resonant particles consist of both passing particles with low energy and trapped particles. Even though these resonant particles make no contribution to the losses that have been seen in the FIDA signal, they also can be lost or redistributed in the presence of the mode.

4.4 Resonant transport

As discussed in the previous section, the resonance map is used to identify resonant particles. The behaviour of those particles affected by modes can be easily understood by examining their perturbed trajectories. Each particle trajectory can be specified in terms of constants of motion (E, μ, P_ϕ) and $\sigma = \text{sign}(v_\parallel)$. When there is a fluctuation at a frequency ω and toroidal mode number n , the toroidal canonical angular momentum P_ϕ of a particle is no longer conserved as the axisymmetry of the magnetic field is broken. In this situation, $K = P_\phi - (n/\omega)E$ is still constant for a single mode. The small mode frequency corresponds to smaller variation in energy as $dP_\phi = n dE/\omega$. Test markers are populated to represent this feature, that is, P_ϕ is varying while energy E and magnetic moment μ remain nearly constant as a result of the frequency being small. In Fig. 4.9, particles are localised at the magnetic axis $R = R_0$. The energy of these markers are $E = 50$ keV which is chosen to be in the area where the FIDA diagnostic is capable of responding. Pitch $\lambda = v_\parallel/v$ and the initial vertical location Z_{ini} respectively are functions of μ and P_ϕ , allowing both variables to vary implicitly. It is often difficult to determine the domain of μ and P_ϕ so this is a common way to generate markers for the computation with different μ and P_ϕ using intuitive coordinates.

As discussed in the previous section, once both toroidal and poloidal

motion frequencies (f_t, f_p) of particles are calculated by tracking their trajectories, the pair (f_t, f_p) can be substituted into the resonance condition Eq. (2.137) and then simulations are iterated over a series of integers for the value of p . In the Fig. 4.9 (a), $p = -1$ resonance is the unique solution found for Eq. (2.137). The corresponding resonance map on (μ, P_ϕ) space is obtained by calculating the values of (μ, P_ϕ) for each test particle in Fig. 4.9 (a) and then the contours of $\Gamma = 0$ are projected on a 2D graph in which the axes are normalised (μ, P_ϕ) , respectively. The resonant region in terms of (μ, P_ϕ) dimensions are shown in Fig. 4.9 (b). Typical markers sharing the same μ and E on each resonant line are selected for investigating the effect of perturbed P_ϕ due to chirping mode on particle orbits. The orbits of particles (a) - (d) resonant with modes at frequencies $\omega = 60 - 30$ kHz are plotted in Fig. 4.10. It allows us to consider which particles are resonant over the duration of a chirp and how a particular particle would have to evolve in terms of its orbit and P_ϕ to remain resonant over the course of the chirp and thus be coherently transported. Combining Fig. 4.9 (b) and Fig. 4.10, it can be seen that the perpendicular drift of a particle weakens with the chirp and the size of the poloidal orbit shrinks. These indicate that the particle travels a shorter distance in the poloidal dimension and hence the poloidal frequency ω_p increases and gets close to its transit frequency ω_t . The decreasing difference between ω_t and ω_p allows the particle to stay in resonance with the chirping mode since the resonance condition becomes $\omega = \omega_t - \omega_p$ where $n = 1$ and $p = -1$.

Berk et al. [88] have studied the spontaneous formation of a hole-clump pair in phase space in the presence of frequency sweeping phenomena and pointed out that clumps (an excess of particles) and holes (a deletion of particles) correspond to up and down chirping frequency, respectively. Now as only downward chirping is seen experimentally, the hole and clump creation

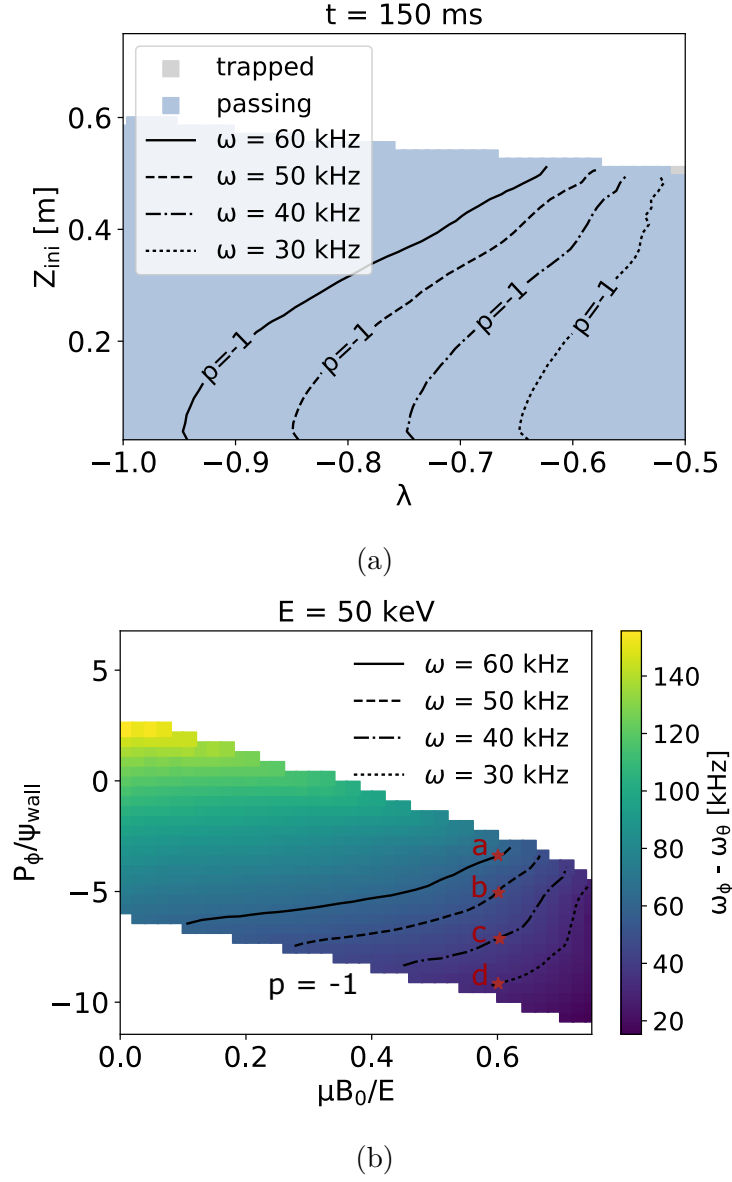


Figure 4.9: (a) Resonance map for 100×100 particles at $R = R_0$ and $E = 50 \text{ keV}$ at $t = 150 \text{ ms}$; (b) mapping resonance map of (λ, Z_{ini}) onto normalised (μ, P_ϕ) phase space. The colours represent the difference between the toroidal and poloidal motion frequencies.

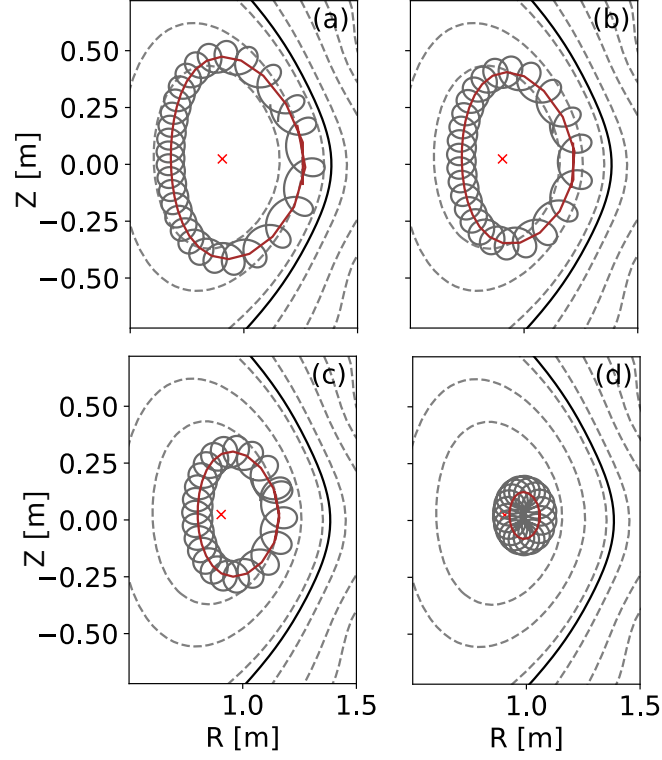


Figure 4.10: Orbits of resonant particles with varying P_ϕ .

could be asymmetric, indicating that holes are generated and move inwards as a consequence of losing particle from the core to the edge. As the chirp progresses downwards in frequency, resonant particles are localised more towards the core of the plasma. A coherent structure is formed in the particle distribution in response to the nonlinear travelling wave. A possible evolution of the particle distribution is demonstrated in Fig. 4.11. During the background dissipation, holes are created near the resonance and then propagate with the new resonance, suggesting that the convection of clumps outwards cannot explain the observed FIDA signals as the resonance region transports towards the centre.

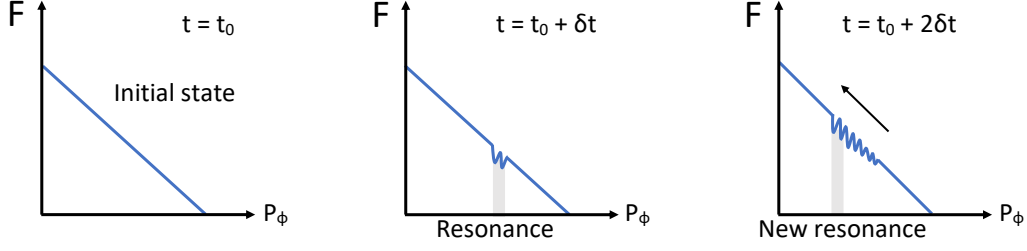


Figure 4.11: Speculative formation and evolution of structures in the particle distribution F based on the resonance maps.

4.5 Summary

Using the code developed in Chapter 3 and calculating particle orbital frequencies as described in the previous chapters, a method is found to determine resonant particles based on the wave-particle resonance condition presented in Eq. (2.137). A MAST experimental discharge #29210 has been analysed by examining the behaviours of these resonant particles. In this discharge, TAEs and fishbones are destabilised by means of two powerful neutral beam injectors. Spectrograms obtained from Mirnov coil measurements have shown that the perturbations are dominated by the $n = 1$ toroidal harmonic with strongly chirping frequency. As calculated in EFIT++, heating efficiency largely decreases when the transition from TAEs to fishbones takes place. Meanwhile, it has been found that the magnetic perturbations are closely correlated with the reduction in integrated FIDA radiance. Changes in D_α emission suggest that fast ions have been ejected from the plasma centre during on-axis neutral beam injection. Based on the wave-particle resonance condition, we identify resonant particles at a location where significant particle losses have been measured with FIDA. Full orbit calculations have resolved two branches of resonance corresponding to $p = 0$ and $p = -1$. The chirping mode frequency enhances the population of the particles that can be affected by the

instabilities and hence has the potential to increase the resonant losses. By examining the trajectories of the typical resonant particles, it is found that the resonance shifts inwards with chirping frequencies, which excludes the outward convective motion of clumps as a reason for fast ion losses observed in FIDA emissions. In the next chapter, attempts will be made to quantify particle transport in the presence of these modes using the **HALO** code which investigates the nonlinear interaction between waves and particles.

Fast ion transport due to chirping modes

5.1 Introduction

In the previous chapter, we have shown experimental observations of fast ion redistribution induced by the perturbed electromagnetic waves present in MAST plasma discharges with Toroidal Alfvén Eigenmodes (TAEs) or fishbone oscillations. Resonance maps have been used to explore the potential impact of chirping modes on fast particle redistribution. In this chapter, we take some initial steps towards quantitative modelling of these processes using the **HALO** code. **HALO** [89] is built on the **HAGIS** code [90] and the **LOCUST** code [91]. **HAGIS** is an existing code that uses guiding centre tracking to nonlinearly evolve modes. It uses flux coordinates and so cannot track particles outside the separatrix. **LOCUST** is a full orbit code that uses realistic geometries and graphics processing units (GPUs) to rapidly track the trajectories of beam particles and evaluate power deposition on wall components. **HALO** adds the nonlinear wave evolution capability of **HAGIS** into **LOCUST** resulting

in a GPU code which can rapidly model the non-linear response of a set of eigenmodes to a particle population using full orbit tracking.

We develop a simple case where fusion alpha particles drive an $n = 6$ TAE in a near cylindrical geometry tokamak and use the **HALO** code to explore the impact that an ad-hoc addition of mode chirping has on the alpha particle redistribution. A fixed amplitude mode and a frequency chirping behaviour similar to that observed in experiment are prescribed. This model can help us gain insight into whether the inclusion of chirping is important for understanding the redistribution and loss of fast particles in reactors. This is important as previous work studying losses of fast particles in fusion reactors have considered mode fields with fixed amplitude and frequency [52].

The material of this chapter is organised as follows. Section 5.2 presents an overview of the **HALO** model. Section 5.3 outlines how we implement the simulation. Plasma scenario is described in section 5.4. Modelling results on the particle transport due to chirping modes are discussed in section 5.5. A summary is given in section 5.6.

5.2 The **HALO** model

5.2.1 Wave-particle energy transfer

Alfvén eigenmodes can be driven unstable in the presence of a fast particle population in which case the wave fields will evolve in response to the particle motion. The **HALO** code is developed to self-consistently calculate the evolution of the MHD modes. A mode with frequency ω_i and toroidal mode number n_i is represented using a complex electric field with amplitude $A_i(t)$

and eigenfunction $\mathbf{e}_i(\mathbf{r})$:

$$\mathbf{E}_i(\mathbf{r}, t) = A_i(t) \mathbf{e}_i(\mathbf{r}) e^{i(n_i \phi - \omega_i t)}. \quad (5.1)$$

The evolution of $A_i(t)$ is related to the power transfer between the particle population and the wave [89]:

$$A'_i(t) = -\frac{1}{2\delta W_{MHD}} \frac{1}{A_i^*} \int \mathbf{E}_i^+ \cdot \mathbf{J} dV. \quad (5.2)$$

Here, δW_{MHD} is the mode energy contained in the eigenfunction \mathbf{e}_i :

$$2\delta W_{MHD} = \frac{1}{\mu_0} \int \frac{\mathbf{e}_i^+ \cdot \mathbf{e}_i}{v_A^2} dV, \quad (5.3)$$

where v_A is the Alfvén velocity. The current density \mathbf{J} is computed from the motion of the particle population and significantly contributed by the resonant particles. To compute the current density the fast particle population is represented by a set of marker particles thus allowing the above equations to be discretised. The discretised form of Eq. (5.2) is written as

$$A'_i(t) = -\frac{1}{2\delta W_{MHD}} \frac{1}{A_i^*} q \sum_j \mathbf{E}_i^+(\mathbf{x}_j) \cdot \mathbf{v}_j f(\mathbf{x}_j, \mathbf{v}_j) \Delta x^3 \Delta v^3, \quad (5.4)$$

where the sum is over a set of marker particles which are tracked by the code. f is the fast particle distribution function and $\Delta x^3 \Delta v^3$ is the volume in phase space that each marker inhabits. The update of A_i proceeds as follows. Let $G(\mathbf{x}_j, \mathbf{v}_j)$ be

$$G(\mathbf{x}_j, \mathbf{v}_j) = \frac{q}{2\delta W_{MHD}} E_i^+(\mathbf{x}_j) \mathbf{v}_j f(\mathbf{x}_j, \mathbf{v}_j) \Delta x^3 \Delta v^3. \quad (5.5)$$

Then $A'_i(t)$ becomes

$$A'_i(t) = \frac{1}{A_i^*} \sum_j G(\mathbf{x}_j, \mathbf{v}_j) \quad (5.6)$$

and

$$\frac{A'_i(t)}{A_i(t)} = \frac{1}{|A_i^2|} \sum_j G(\mathbf{x}_j, \mathbf{v}_j). \quad (5.7)$$

Assume that the variation of A_i over an integration timestep is small, then one can integrate using an approximate analytic formula:

$$A_i(t + \Delta t) = A_i(t) \exp \left(\frac{1}{|A_i(t)|^2} \sum_j \int_t^{t+\Delta t} G(\mathbf{x}_j, \mathbf{v}_j) dt \right). \quad (5.8)$$

The integral in the exponent is evaluated by following particles along their trajectories for one wave update timestep Δt and usually $\Delta t \gg dt$ where dt is the integrator timestep. Typically $dt \sim 10^{-9}$ whereas $\Delta t \sim 10^{-7}$ although there is some flexibility.

5.2.2 Monte-Carlo modelling

The HALO code evaluates the evolution of modes in Eq. (5.4) by determining the power transfer between the modes and a set of particles being tracked in the presence of the mode fields. The marker particles are uniformly distributed in spatial positions x, y, z , velocity v , pitch λ and gyro-angle α where $\lambda = v_{\parallel}/v$ and weighted according to the distribution function. A quasi Monte-Carlo loading scheme, the Hammersley set [92, 93] is applied to drop particles over the whole phase space. The loading is uniform (i.e. roughly constant density of points) but irregular. The Hammersley sequence gives low noise for the Monte-Carlo simulations and is determined based on the following principles. Any non-negative integer k can be expressed in terms of a prime base p :

$$k = a_0 + a_1 p + a_2 p^2 + \cdots + a_r p^r, \quad (5.9)$$

where the coefficient a_i is an integer between 0 and $p-1$. Then a Hammersley point Φ_p is given by a_i and p

$$\Phi_p = \frac{a_0}{p} + \frac{a_1}{p^2} + \frac{a_2}{p^3} + \cdots + \frac{a_r}{p^{r+1}}. \quad (5.10)$$

Φ_p is a point between 0 and 1 and can be used to scale a coordinate value for a particular dimension, i.e., $x = x_{\min} + \Phi_p(x_{\max} - x_{\min})$ where x_{\max} and x_{\min}

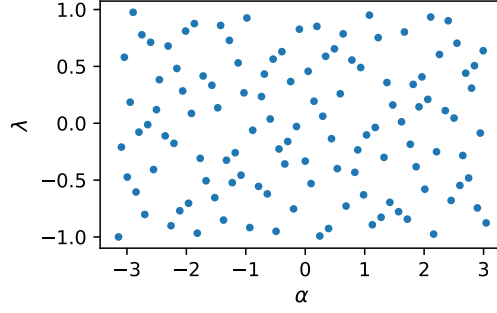


Figure 5.1: 2D Hammersley set generated by using prime base of 2 and 3. A total size of 120 markers are distributed uniformly but irregularly in the space of gyro angle $\alpha \in [-\pi, \pi]$ and pitch $\lambda = v_{\parallel}/v \in [-1, 1]$.

are the upper and lower limits of the coordinate x , respectively. Six prime bases 2, 3, 5, 7, 11 and 13 are used to generate particle initial states in **HALO**. For each particle with ID k we can generate a set of coordinate values by finding Φ_p for $p = 2, 3, 5, \dots$ and scaling this by the range of the coordinate. Each dimension in phase space is assigned a different prime base and this results in a uniform but highly irregular loading of the space with good noise properties. In Fig. 5.1, a 2D Hammersley set is generated on gyro angle α and pitch λ space. The prime bases are 2 and 3 for α and λ . Particle markers are distributed uniformly but highly irregularly in the domain of $[-\pi, \pi]$ and $[-1, 1]$.

5.2.3 Noise reduction

The prescription above requires large numbers of markers to converge well. One way **HALO** achieves this is via the use of GPUs to track the full orbits of particles in electromagnetic fields. GPU cards are designed for parallel processing and can be used for scientific simulations and processing a large volume of physics/mathematical calculations simultaneously. GPUs are capable of tracking large numbers of particles rapidly but are less efficient than

CPU's if there is only a few particles as it takes more machine time to launch a GPU task than a CPU task. Thus the more GPU tasks are requested at one time, the less machine time each GPU consumes on average.

A second method used in HALO to reduce Monte-Carlo noise is to employ a delta-f scheme. The delta-f approach is developed to solve the evolution of the distribution function f which is perturbed via the interaction between particles and waves in plasmas. f is decomposed into the an equilibrium and a perturbed part:

$$f(\Gamma, t) = \underbrace{f_0(\Gamma, t)}_{\text{steady}} + \underbrace{df(\Gamma, t)}_{\text{markers}} \quad (5.11)$$

where Γ represents an arbitrary coordinate in phase space. The equilibrium f_0 is a steady state solution of the Vlasov equation and df is represented by following the orbits of particles in the simulation. The power transfer to the wave calculated in Eq. (5.4) can be split into two parts by using Eq. (5.11) and reduces to

$$A'_i(t) = -\frac{1}{2\delta W_{MHD}} \frac{1}{A_i^*} q \sum_i \mathbf{E}_i^+(\mathbf{x}_i) \cdot \mathbf{v}_i(f_0 + df) \Delta x^3 \Delta v^3, \quad (5.12)$$

The cancellation of f_0 in Eq. (5.12) is due to the axisymmetric equilibrium, that is, the contribution from the first term to the integral vanishes because it is proportional to $\int d\phi \cos n\phi = 0$. Therefore the noise from the evaluation of the f_0 term can be also avoided.

5.2.4 Inputs for HALO

To quantify the fast ion transport, a series of codes which solve different problems is required. The workflow required to perform a HALO simulation is shown in Fig. 5.2. The plasma equilibrium is reconstructed by EFIT and the linear MHD stability code MISHKA is then used to determine the mode

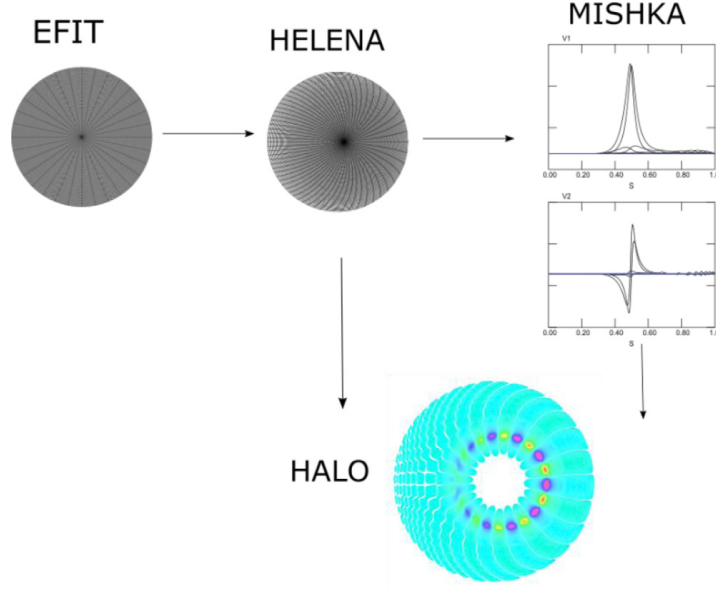


Figure 5.2: Workflow of HALO. A plasma equilibrium is provided by EFIT. Mode eigenfunctions and frequencies are calculated for this equilibrium by the linear MHD code MISHKA in straight field line coordinates and then converted to cylindrical coordinates. (image taken from ref. [89].)

eigenfunctions and frequencies for this equilibrium in a straight field line system. HELENA provides coordinate transformation maps from straight field line coordinates to cylindrical coordinates used by HALO. Then HALO can evolve the mode amplitude along with the perturbed particle distribution function. A list of plasma parameters, equilibrium profiles, and eigenfunctions used for the problem of fast ion transport to be discussed in this chapter is as follows.

Equilibrium An MHD equilibrium is required to start the calculation, providing zero order quantities related to fluid and field, such as the poloidal flux function, 2D magnetic geometry, and q profile, etc. The equilibrium magnetic field also contains the instability information of the bulk plasma.

Steady state fast ion distribution function HALO requires a distribution function f_0 in constants of motion space. This is because the evolution of df for each particle requires knowledge of the local gradients of f_0 with

respect to E and P_ϕ . f_0 could be a beam slowing down distribution function, a distribution caused by ICRF heating, or from fusion alphas as in the case we will study.

Eigenmode function MHD instabilities are described by the ideal MHD equations as shown in section 2.4. For an equilibrium of interest, precise solutions to these equations can be computed by numerical codes, such as *MISHKA* [76]. The *HALO* code will investigate the nonlinear interaction between the prescribed eigenmodes and particles. As shown in Ref. [89, 94], the eigenmode functions are obtained by representing the time dependence of the perturbation in an exponential form $\exp \lambda t$. The perturbed magnetic and electric fields are given by

$$\begin{aligned} J\delta B^1 &= -i \left(m \left(\frac{d\psi}{ds} \hat{A}_2 \right) + n \left(\frac{d\psi}{ds} q \hat{A}_2 \right) \right) \\ J\delta B^2 &= inA_1 + \frac{\partial}{\partial s} \left(\frac{d\psi}{ds} \hat{A}_2 \right) \\ J\delta B^3 &= \frac{\partial}{\partial s} \left(\frac{d\psi}{ds} q \hat{A}_2 \right) - imA_1 \\ \delta E_i &= -\frac{\lambda A_i}{c} \end{aligned} \tag{5.13}$$

where the Jacobian is $J = \frac{d\psi}{ds} \frac{qR^2}{RB_\phi}$ and the vector potential is related to two velocity variables (v_1, v_2)

$$\begin{aligned} A_1 &= \frac{-iv_2}{\lambda} \\ \frac{d\psi}{ds} q \hat{A}_2 &= -\frac{v_1}{\lambda} \\ \hat{A}_2 &\equiv [\mathbf{A} \times \mathbf{B}_0]^1 / B_0^2 \end{aligned} \tag{5.14}$$

and

$$\begin{aligned} v_1(s, \theta, \varphi) &= e^{\lambda t} e^{in\varphi} \sum_m e^{im\theta} \sum_{i=1}^N \left(v_{m,i}^1 H^1(s) + dv_{m,i}^1 H^2(s) \right) \\ v_2(s, \theta, \varphi) &= e^{\lambda t} e^{in\varphi} \sum_m e^{im\theta} \sum_{i=1}^N \left(v_{m,i}^2 h^1(s) + dv_{m,i}^2 h^2(s) \right) \end{aligned} \tag{5.15}$$

where $H^1(s)$, $H^2(s)$, $h^1(s)$ and $h^2(s)$ are Hermite quadratic or cubic polynomials. The calculation is carried out in the straight field-line coordinates (s, θ, ϕ) and then transformed to the conventional cylindrical coordinates using coordinate maps provided by the **HELENA** code [95].

5.3 Modelling chirping modes

As described in section 2.4.4 on one dimensional Landau damping, waves can either damp or grow as they interact with particles. The condition depends on the sign of the gradient of the particle parallel distribution function with respect to the particle parallel velocity in the vicinity of wave phase velocity, i.e., $G = (\frac{\partial f_{\parallel}}{\partial v_{\parallel}})_{\omega/k}$. For instance, when $G > 0$ waves can grow indicating that a free energy in particles drives the growth of the waves and G tends to be flattened as particles lose their kinetic energies. In the hybrid MHD-kinetic model, drive/damping is affected by both $\frac{\partial f_0}{\partial \epsilon_0}$ and $\frac{\partial f_0}{\partial P_{\phi}^{(0)}}$ with opposite sign as shown in Eq. (2.127) and (2.136). Both particle distribution and mode amplitude evolve in time interactively. The **HALO** model is consistent with both mechanisms and can explore the further nonlinear phase. Fig. 5.3 (taken from Ref. [89]) shows the evolution of the wave and particle energies and the mode amplitude for a full non-linear simulation of an $n = 6$ TAE interacting with an alpha particle slowing down distribution (the exact scenario is described in the following sections). The eigenmode of interest is a localised TAE mode which is numerically calculated with the cylindrical equilibrium. The values of geometry and field give a fast particle orbit width which is comparable to mode width of $n = 6$ modes so the power transfer between particles and modes is expected to be observable in the simulation. One can see that the energy grows exponentially during the linear phase from $t = 150$ to 300 wave

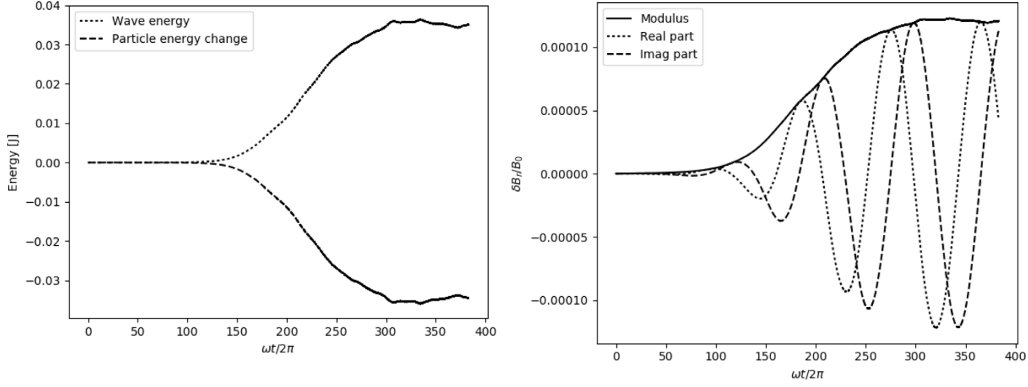


Figure 5.3: The energy-exchange occurring between the TAE and alpha particles (left) and non-linear growth of the TAE (right) (images taken from Ref. [89])

periods. Later in the non-linear phase, the rate of the energy-exchange slows down and energies of the particle and wave reach a saturated level lasting for 175 wave periods until the simulation ends. As the mode evolves with time, the particle distribution function $f = f_0 + df$ would change coherently, where f_0 is the equilibrium distribution function and assumed to be independent of time. Therefore it is only df that changes with time and we use df to evaluate the macroscopic particle transport induced by a mode.

In the previous chapter, strong and continuous chirping in time can be seen from the measured mode frequency (TAE and fishbone) whereas the ideal MHD model can only compute and predict a single and constant mode frequency. The chirping phenomena are widely observed in energetic beam injection experiments on various fusion devices. In HALO, we can simulate chirping by adding an ad-hoc damping but the behaviour does not match what is observed in experiment partly due to lack of collisions. To overcome this, we impose a chirping structure by hand that roughly matches the scale of chirping seen in experiment. This might not be physically correct but should still give us some insight into how important chirping is for particle redistribution for this case and whether HALO can potentially be used to

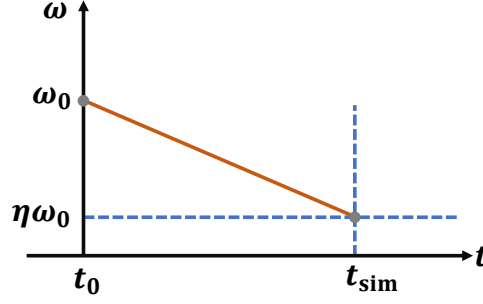


Figure 5.4: The mode frequency $\omega(t)$ is assumed to be a linear function of time. ω_0 is the eigen-frequency computed by the MISHKA code. The ad-hoc chirping frequency are realised by a coefficient η . $\eta < 1$ is for down chirping modes and $\eta > 1$ for up chirping modes.

model it.

On MAST, the mode frequency rapidly sweeps down in a nearly linear way as can be seen in Fig. 4.2. We therefore implement an ad-hoc frequency chirp by a linear function of time as shown in Fig. 5.4. The frequency function $\omega(t)$ is determined by two points (ω_0, t_0) and $(\eta\omega_0, t_{\text{sim}})$. Here, ω_0 is the eigenfrequency numerically obtained from MISHKA, $t_0 = 0$ is the initial time when the simulation starts and t_{sim} is the total simulation time. The mode frequency in the end is assumed to be a fraction of the eigen-frequency, defined by a coefficient η , that is, $\omega(t_{\text{sim}}) = \eta\omega_0$. The expression of a chirp frequency is written as

$$\omega(t) = \omega_0 \left(1 + \frac{(t - t_0)(\eta - 1)}{t_{\text{sim}} - t_0} \right) \quad (5.16)$$

In HALO, each marker represents a change in the local number of particles given by

$$dN = df \cdot J \cdot dV, \quad (5.17)$$

where J is the Jacobian and dV is the volume element in the hypercube used to perform the particle loading. For the loading scheme discussed above, the Jacobian is $J = v^2$ and $dV = dx dy dz dv d\lambda d\alpha$. The calculated df is binned

for each particle. In Fig. 5.8, $\langle df \rangle$ is the averaged df value obtained by the summation over the total number of particles in a bin and division by the total phase space volume:

$$\langle df \rangle = \frac{\sum_i (df_i J_i dV)}{\sum_i J_i dV} = \frac{\sum_i (df_i J_i)}{\sum_i J_i}, \quad (5.18)$$

where dV is cancelled out since it is a constant for each particle. $\langle df \rangle$ is used to estimate the particle redistribution in the presence of the modes.

5.4 Study scenario

A near cylindrical geometry tokamak configuration is considered. Fig. 5.5 shows the plasma equilibrium with a circular cross-section without elongation or triangularity. It is a relatively simple magnetic geometry used for validating the HALO code as presented in [89]. The parameters of this configuration are reasonably close to a typical tokamak with large aspect ratio. The major radius R_0 is at 3 m and the aspect ratio $a/R_0 = 0.25$. The toroidal magnetic field at $R_0 = 3$ is 3.0 T and q_0 is 1.82.

For this plasma equilibrium, eigenmodes with toroidal mode number $n = 6$ and mode frequency $\omega_0 = 481$ kHz are found by the MISHKA code as demonstrated in Fig. 5.6. From the poloidal cross-section, the perturbed electromagnetic components are aligned with the flux surface. The relative magnitude of the magnetic field components are comparable while the strength of the toroidal electric field E_ϕ and are much lower than that of the poloidal components E_R and E_Z . Both the radial and vertical components of the electric field are high in the low field side (LFS) compared to the high field side (HFS). However, the distribution is opposite for the poloidal magnetic fluctuations, that is, B_R and B_Z are relatively weak in the LFS.

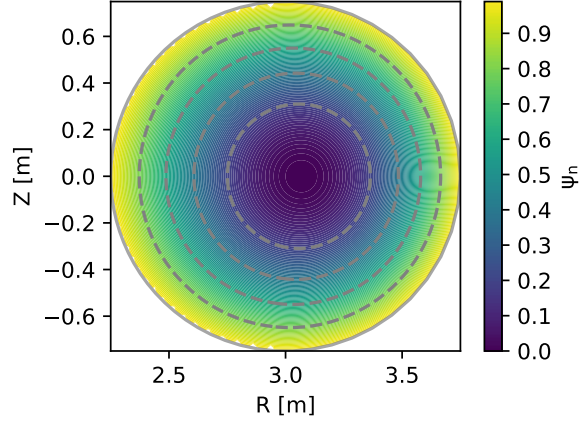


Figure 5.5: A circular equilibrium for benchmarking the HALO code. This equilibrium represents a simplified conventional tokamak configuration with a circular poloidal cross section. The magnetic axis is located at $R = 3$ m. ψ_n is the normalised flux surface function and in the range of $0 \leq \psi_n \leq 1$. This equilibrium is used for the calculations throughout this chapter.

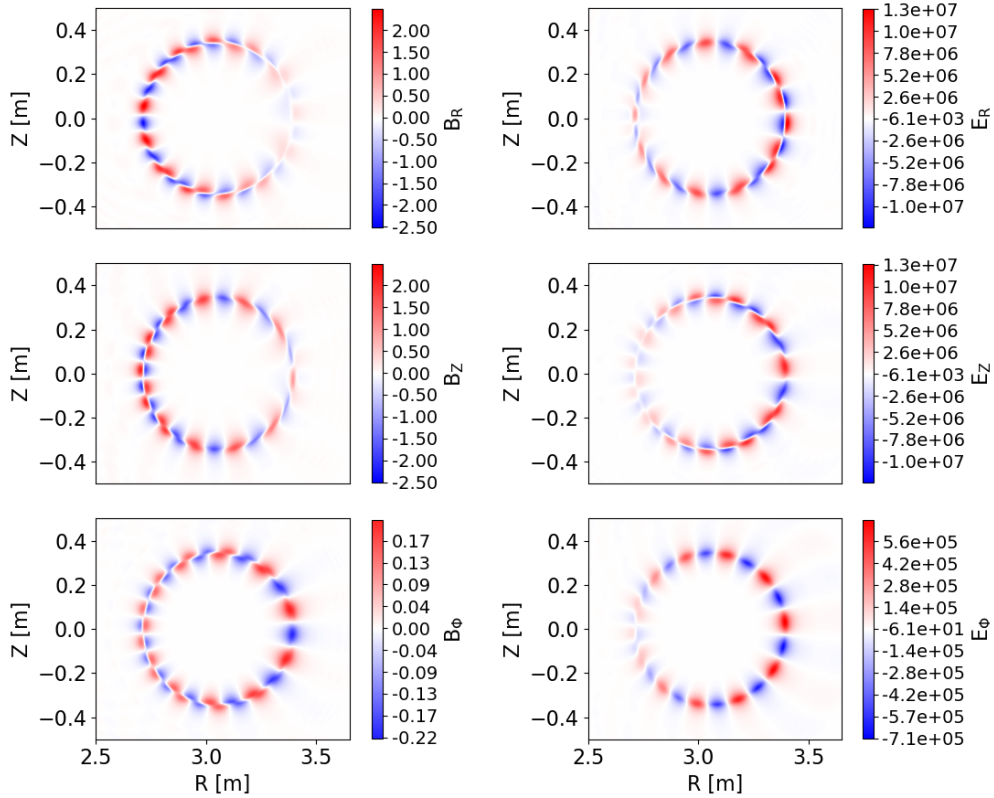


Figure 5.6: Solutions of eigenmodes found by MISHKA for the bulk plasma confined in the circular flux surface as described above.

The alpha particle distribution function takes a product form given by $f_0 = h_1(P_\phi)h_2(E)$ [52, 96]. Here, h_1 is sensitive to the plasma temperature and density profiles and is expressed in terms of $P_\phi(\psi_p)$: $h_1(P_\phi) = (1 - P_\phi^2)^{10}$. h_2 is related to alpha particle drag induced by collisions with thermal electrons and ions. In this case, we assume a fuel mixture 50:50 for D and T ions with same temperature at $T_i = 20$ eV and an analytical solution of the Fokker-Planck equation is written as

$$h_2 = \frac{1}{v^3 + v_c^3} \operatorname{erf} \left[\frac{E - 3.5 \text{ MeV}}{106 \times 10^3 \sqrt{T_i [\text{keV}]}} \right]. \quad (5.19)$$

Here, the error function is defined as

$$\operatorname{erf} z = \frac{2}{\sqrt{\pi}} \int_0^z e^{-t^2} dt, \quad (5.20)$$

and v_c is the *crossover* velocity approximately given by

$$v_c \equiv \left(3\sqrt{\pi} \frac{m_e Z_1}{4} \right)^{\frac{1}{3}} \sqrt{\frac{2T_e}{m_e}}, \quad (5.21)$$

where $Z_1 = \frac{0.5}{2m_p} + \frac{0.5}{3m_p}$. When the alpha particle velocity v equals v_c , the drag exerted by the thermal electrons on the alpha particles equals that of the thermal ions on the alpha particles. For alpha particle velocity below v_c , the ion drag dominates and for velocity above v_c the electron drag dominates.

5.5 Results

To simplify the problem, the mode amplitude $A = dB_r/B_0$ is assumed to be a constant when a frequency chirp is prescribed manually. Here, B_0 is the equilibrium magnetic field on axis and dB_r is the maximum radial mode field on the outboard mid-plane. In Fig. 5.8, $A = 1 \times 10^{-3}$ is set to be constant for the entire simulation time $t_{\text{sim}} = 6$ ms. The chirp coefficient is $\eta = 25\%$

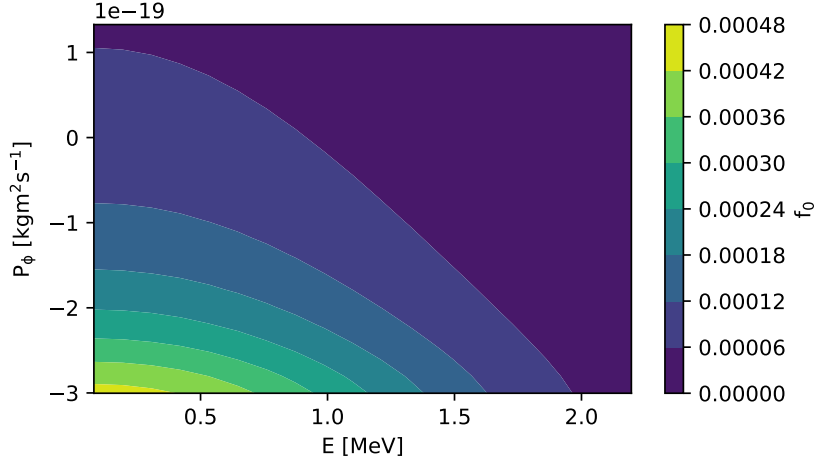


Figure 5.7: A mocked-up alpha particle distribution function $f_0(E, P_\phi)$ is used in the simulation. f_0 is constructed by a product form $f_0 = h_1(P_\phi)h_2(E)$. Here, the spatial dependence of f_0 is given by h_1 term and the collision drag from background ions and electrons on alpha particles is described in h_2 term.

representing a mode with frequency down sweeping in time. $\langle df \rangle$ is binned in R and Z coordinates. A negative $\langle df \rangle$ indicates that particles leave a region and cause a decrease in the particle number while a positive $\langle df \rangle$ corresponds to an opposite situation. There is a visible decrease in particle number in the core and an increase from mid-radius towards the edge. Particles are lost from where the eigenmode is located as shown in Fig. 5.6. As the simulation time elapses, particles are redistributed from the plasma centre. In the contour graph, the plotted data are restricted to ± 4 times of the standard deviation of $\langle df \rangle$ to get rid of outliers in the data and improve the resolution. By filtering a small section of the data, the transport structure can be seen more clearly. This is the reason that there are some blank areas in the image.

Particles are asymmetrically lost from the plasma centre and they eventually leave the confinement region from the outboard side as shown in Fig. 5.9, where the magnetic axis $R_0 = 3$ m and the outboard and inboard refer to the region with $R > R_0$ and $R < R_0$, respectively. The data is consistent with the mode moving particles from passing orbits in the core onto trapped

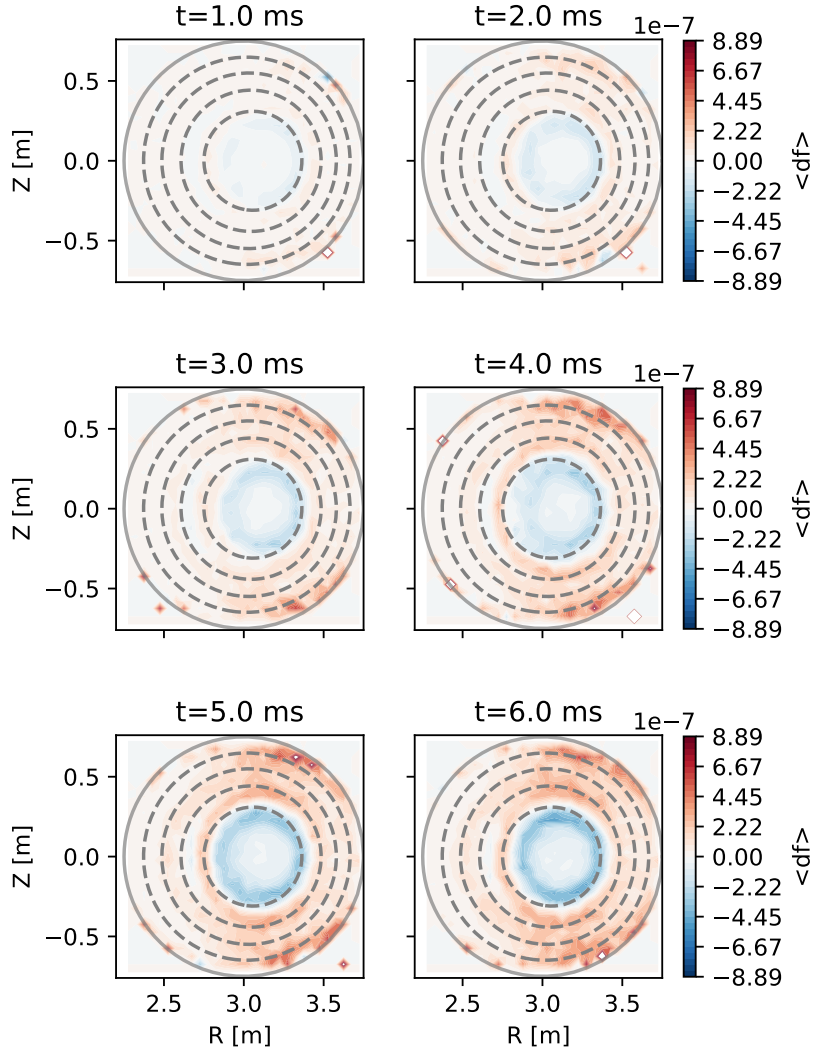


Figure 5.8: Time slices for $t = 1-6$ ms of particles being transported from the plasma centre (blue region) to edge (red region) due to a chirping mode. $\langle df \rangle$ is a quantity proportional to the change of the particle number. The mode amplitude $A_0 = 10^{-3}$ is fixed throughout the simulation and the chirp coefficient is $\eta = 0.25$ corresponds to a down chirping frequency. The grey contours are the poloidal flux function from the equilibrium data and the solid grey line labels the LCFS. The blank squares come from the data filtering of $\pm 4\sigma$, where σ is the standard deviation of $\langle df \rangle$.

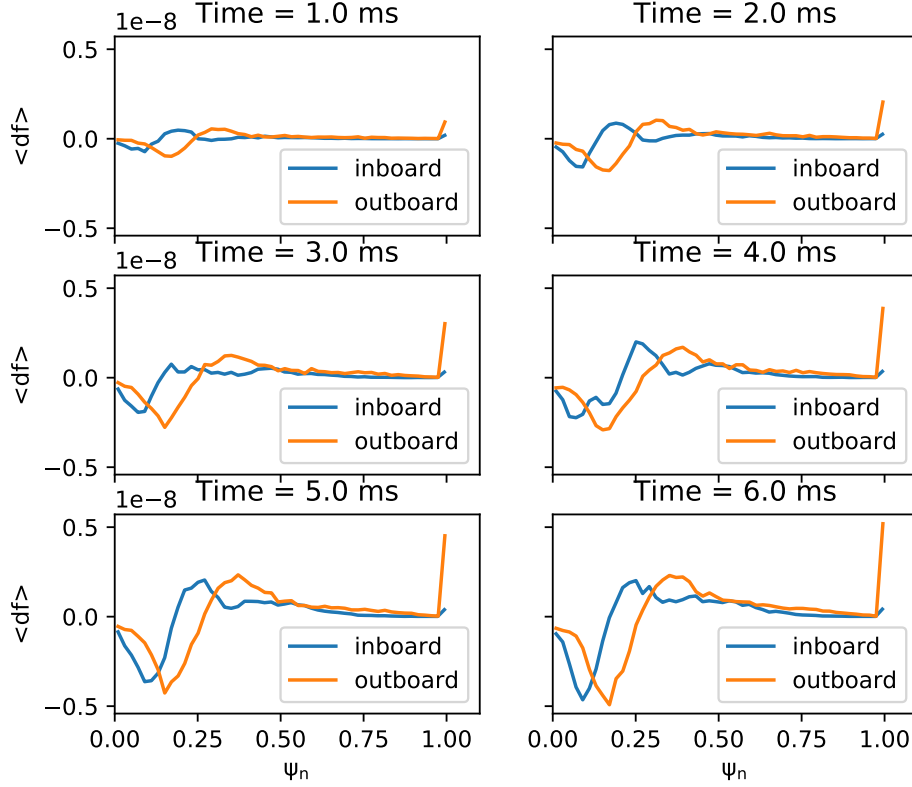


Figure 5.9: Asymmetric distribution of the redistributed particles. Inboard and outboard sides refer the radial location R relative to the magnetic axis R_0 .

and lost orbits.

As particles resonate with the mode, particle constants of motion would change. In Fig. 5.10, the relationship between $\langle df \rangle$, energy E and toroidal angular momentum is investigated. The expression of P_ϕ is given in Eq. (2.95) and repeated here: $P_\phi = Ze\psi_p/2\pi + mRv_\phi$. P_ϕ is a function of particle toroidal velocity v_ϕ and poloidal flux surface function ψ_p which shows the location of a particle. Significant particle transport can be seen in the P_ϕ dimension. Particles are lost from the region where P_ϕ is negative and accumulated at the region with $P_\phi > 0$. Changes in either ψ_p or v_ϕ in the expression of P_ϕ can cause particle redistribution in the P_ϕ space. In Fig. 5.11 (a-c), $\langle df \rangle$ is separately binned in terms of P_ϕ , v_ϕ and ψ_n . In the ψ_n dimension, particles

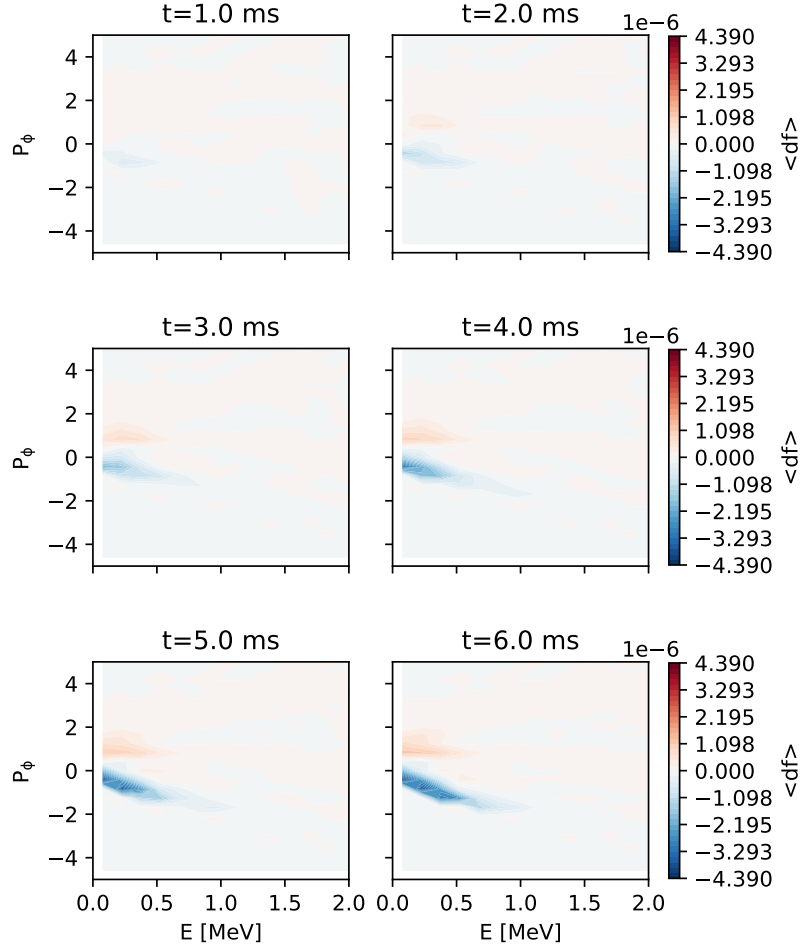


Figure 5.10: Time slices at 1-6 ms of $\langle df \rangle$ binned in E and P_ϕ space. P_ϕ is normalised by $e\psi_{\text{bry}}$ where ψ_{bry} is the poloidal flux at the boundary (LCFS). Most of resonant particles are at energy $E < 0.5$ MeV. A boundary between the particle loss and gain appears at $P_\phi = 0$ surface. Parameters of the simulation are the mode amplitude $A_0 = 10^{-3}$ and chirp coefficient $\eta = 0.25$.

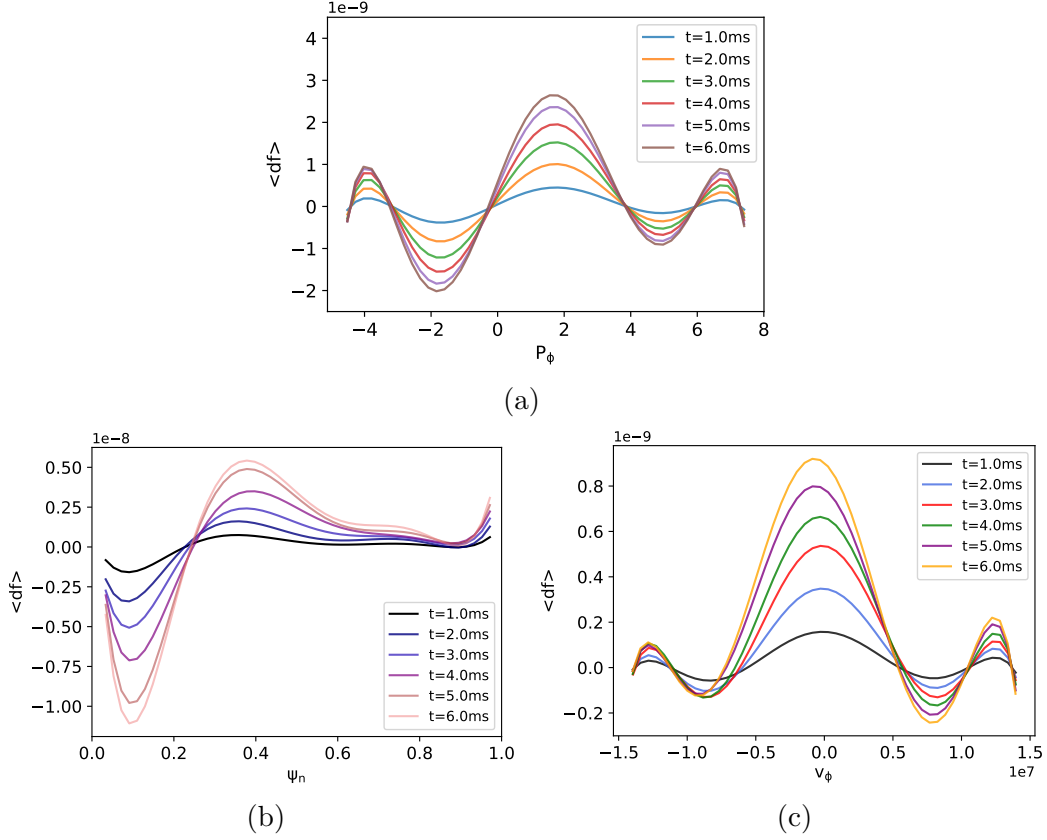


Figure 5.11: $\langle df \rangle$ is binned in one dimensional space (a) toroidal angular momentum P_ϕ ; (b) normalised poloidal flux ψ_n ; (c) particle toroidal velocity v_ϕ . P_ϕ is normalised by $e\psi_{\text{bry}}$ where ψ_{bry} is the poloidal flux surface function at the boundary (LCFS). Subplots (a) and (c) enjoy high degree of similarity and the change in v_ϕ is likely to be responsible for particle transport in P_ϕ space. Subplot (b) shows particles are transported from plasma centre $\psi_n = 0.1$ to outer region $\psi_n = 0.4$ and the LCFS $\psi_n = 1$. Eventually those particles escape the confinement region and hit on the facing wall.

move outwards from $\psi_n \sim 0.1$ to $\psi_n \sim 0.4$. Some particles cross the LCFS ($\psi_n \sim 1$) and then leave the confinement region. The change in particle toroidal velocity is qualitatively consistent with the change in P_ϕ . When v_ϕ increases/decreases, P_ϕ is changing in a consistent way based on the sign of v_ϕ in the equation for P_ϕ .

A visible particle redistribution has been identified by simulating a chirping mode with a constant mode amplitude $A = A_0$ in HALO. As a comparison, a case with a constant mode frequency and evolving mode amplitude $A = A(t)$

is considered. The mode linearly grows and eventually saturates. From $t = 1$ ms, particles can be found to leave the plasma centre and spread out reaching outer area or outside of the LCFS. However, the particle transport is relatively weak overall and the lost region is restricted to the outboard side, exhibiting different features to the chirping case as shown in Fig. 5.8 where the lost region is extended to the inboard side.

As discussed in the previous chapter, a chirping frequency would increase the resonance region, improve wave-particle interaction, and potentially enhance particle transport. For a single mode frequency, a certain group of particles can resonant with the mode. If the mode frequency is continuously changing with time, more particles will enter into the resonance region and exchange energy with the mode. To investigate this effect, we fix the mode amplitude to be $A = A_0 = 1e - 3$ and vary the chirp coefficient η in the linear equation of mode frequency $\omega(t)$ as defined in Eq. (5.16). A total time of 6 ms is simulated and the final particle state are shown in Fig. 5.13. Both up chirp and down chirp are considered, corresponding to $\eta > 1$ and $0 < \eta < 0$, respectively. Particle redistribution develops and more particles are shifted outwards as $|\eta - 1|$ increases. $\eta = 1$ represents a constant mode frequency. We have run two different non-chirp cases, one with a fixed mode amplitude and one with a time varying amplitude $A(t)$ which is solved in HALO. Particle transport in both cases are comparable and relatively weak compared to those affected by both up and down chirping modes.

For an eigenmode with constant mode frequency, it has been found the increasing mode amplitude does not significantly increase the particle transport. However, the situation is different for chirp modes. We have used a constant mode amplitude $A_0 = 10^{-3}$ to study how a down chirping mode affects the particle transport. Now we vary A_0 and a set of different mode

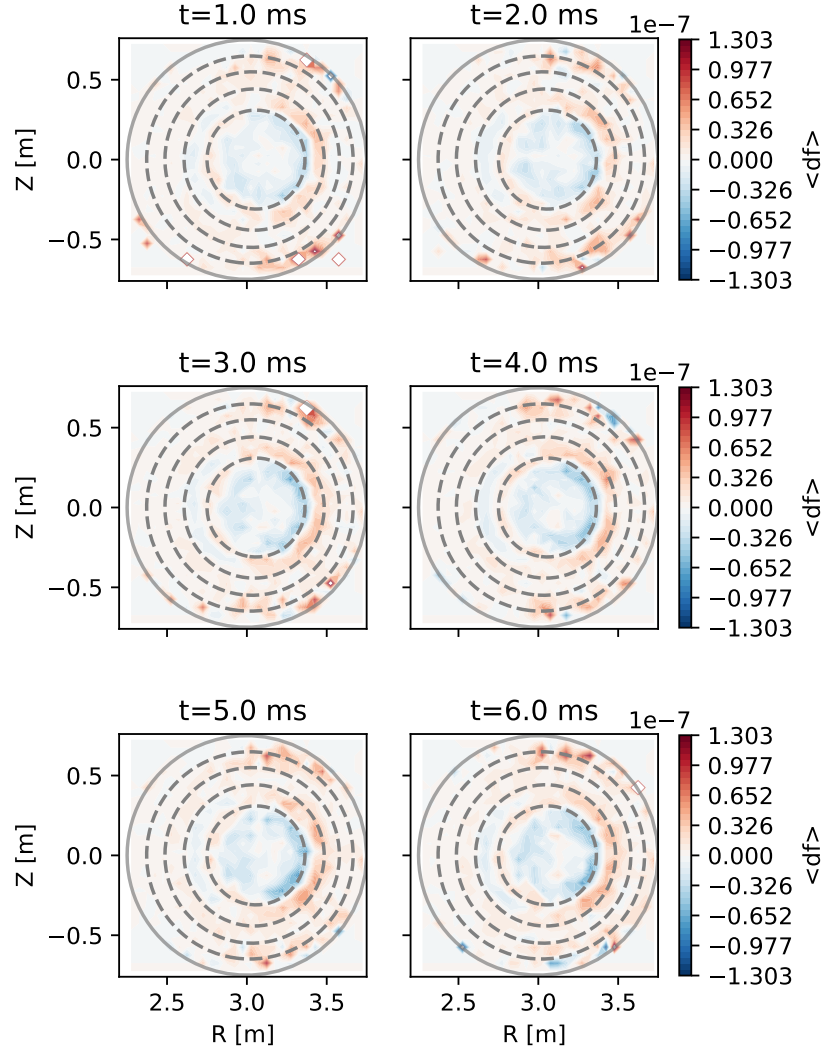


Figure 5.12: Reduced particle transport in the presence of the eigenmode with a constant mode frequency $\omega_0 = 481$ keV computed by the MISHKA code. The initial mode amplitude is $A(t = 0) = 10^{-3}$. $A(t)$ evolves in time as the mode interacts with particles and is solved consistently by the HALO. The particle transport level is much lower than those induced by a chirping mode.

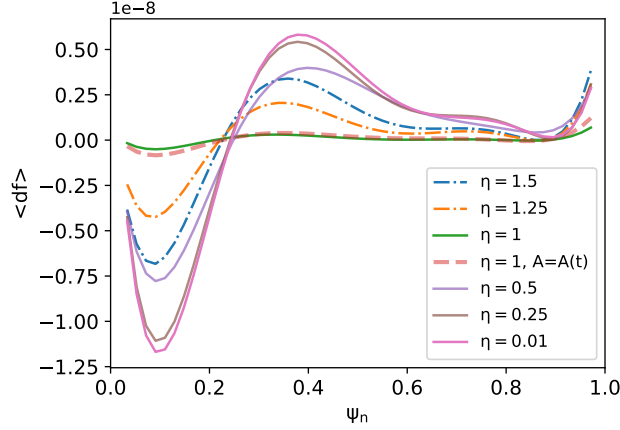


Figure 5.13: The particle transport level varies with the chirp coefficient η . Calculations with various η track particles for the same time of 6 ms and all curves shown here are the final measures at $t = 6$ ms. The mode amplitudes for all are constant $A_0 = 10^{-3}$ except the one marked with $A = A(t)$ (orange dashed). $\eta > 1$ and $0 < \eta < 1$ correspond to up and down chirping frequencies, respectively. The particle transport enhances with growing $|\eta - 1|$ which states the deviation of the ending mode frequency away from the initial value ω_0 computed by the MISHKA code. The exception is when $\eta = 1$ (non-chirp case). Interestingly whether the mode amplitude evolves in time or not (orange dashed and green solid lines), the particle transport is constantly small.

amplitude $A_0 = 10^{-2}, 10^{-3}, 10^{-4}, 10^{-5}$ are selected. HALO tracks particles for 6 ms in the presence of a down chirping mode with a chirp coefficient $\eta = 0.25$. In Fig. 5.14, the particle averaged distribution $\langle df \rangle$ at final state $t = 6$ ms is plotted. For the large mode amplitudes, $A_0 = 10^{-2}$ and 10^{-3} , particles are redistributed outwards and the change in particle number increases with increasing mode amplitude.

We quantify the uncertainty of the calculation by using two different Hammersley sets for loading particles. The quasi-random sequences are determined by setting different values of k in Eq. (5.9), i.e., $k = 1, 2, 3, \dots, n_p$ and $k = n_p + 1, n_p + 2, \dots, 2n_p$, respectively. Here, n_p is the total number of simulated particles. As shown in Fig. 5.15, $\langle df \rangle$ calculated by two sets, labelled in “H1” and “H2”, agrees well for large mode amplitude $A_0 = 10^{-2}$

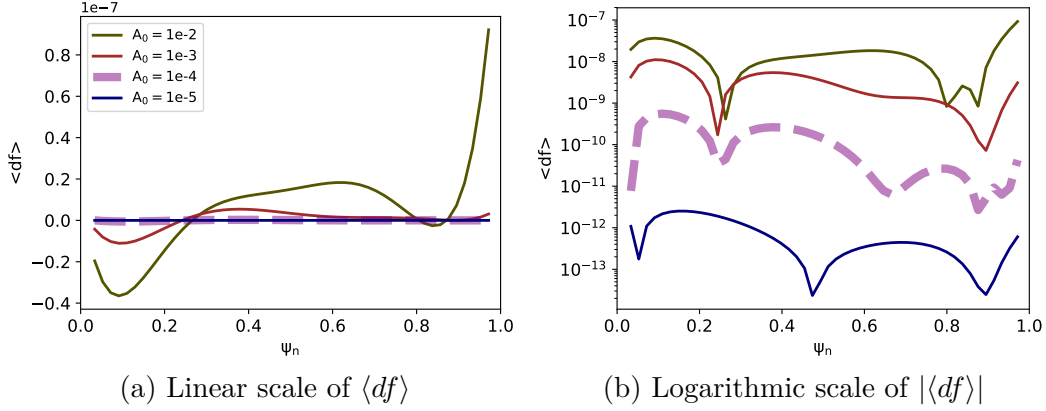


Figure 5.14: The mode amplitude has an effect on the particle transport induced by a down chirping mode. The change in particle number is largely reduced as the mode amplitude weakens. When A_0 is on the order of 10^{-4} or smaller, the chirping mode will not affect the particle transport. The chirp coefficient $\eta = 0.25$ and the simulation time is 6 ms for all cases.

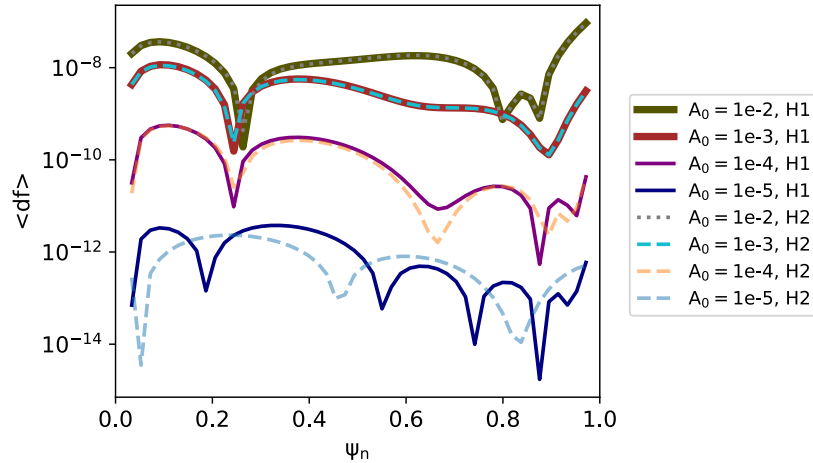


Figure 5.15: $\langle df \rangle$ calculated by two different quasi-random sequences, “H1” (solid) and “H2” (dashed or dotted). The simulation results are more diverged with decreasing mode amplitude.

and 10^{-3} . The uncertainty appears when A_0 is as small as $A_0 = 10^{-4}$ or 10^{-5} . We calculate the coefficient of variation (CV), defined by the standard deviation σ and mean μ , $CV = \sigma/\mu$, which measures the numerical stability when different Monte Carlo loading sequences are used. It can be seen in Fig. 5.16, as the mode amplitude increases, CV decreases and the dispersion of the numerical results around their mean values is largely improved.

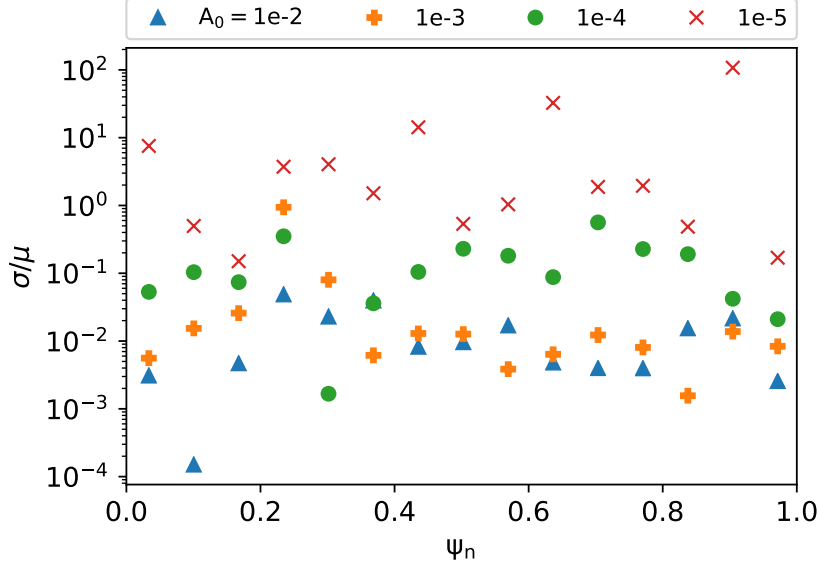


Figure 5.16: Coefficient of the variation, $CV=\sigma/\mu$, where σ and μ are the standard deviation and mean value, respectively. As A_0 increases, CV is reduced and the results are converged for simulating particles with different initial states.

5.6 Discussion and summary

In this chapter, we have modified the evolution of the mode frequency by hand and used a mocked-up alpha distribution in **HALO** to us an indication of the potential impact of chirping on fast particle loss calculations. As predicted in the previous chapter using calculated resonance maps, the chirping frequency widens the wave-particle resonance region and increases the number of the resonant particles that are redistributed.

The modelling shows the dynamics of particles being transported from the plasma centre to the edge assuming a time dependent frequency function. Particles are lost asymmetrically from the core and the lost regions at the outboard side relative to the magnetic axis are shifted outwards. The asymmetry could be correlated with the structure of particle passing orbits.

The results also show the particle transport in constants of motion space

by binning $\langle df \rangle$ in E and P_ϕ space. A clear boundary of particles being lost can be found at the $P_\phi = 0$ surface. Particles are lost from regions with $P_\phi < 0$ and gained in regions with $P_\phi > 0$. The change in P_ϕ depends on the normalised poloidal flux surface ψ_n and particle toroidal velocity v_ϕ , suggesting an evident transport in velocity occurring during wave-particle resonance.

As a comparison, simulations with a constant mode frequency have also been implemented. The particle transport is low compared with the chirping case and not affected by either fixed mode amplitude or time varying mode amplitude when consistently solving for the non-linear wave particle evolution in **HALO**. Furthermore, particle transport increases with $|\eta - 1|$. Here, η is defined as the chirp coefficient and $|\eta - 1|$ shows the degree that the ending frequency deviates from the initial frequency. This includes up and down chirping situations since both chirping frequencies have been observed in experiments.

Even though the particle transport is not influenced by the mode amplitude A for a non-chirping frequency, the value of A can change how many particles are redistributed due to a chirping mode. More particles transport towards the edge as the constant mode amplitude increases as shown in the simulations.

In summary, a simplified model using a mocked-up alpha distribution and an ad-hoc chirp frequency evolution is proposed and simulated in **HALO**. Full non-linear modelling shows that eigenmodes with a single and constant frequency will not cause large particle redistribution. It suggests that attempting to model redistribution and loss of fast particles without a proper inclusion of the frequency evolution of the modes may well be insufficient.

Conclusion

Energetic particle physics is an active research topic in the fusion community and a good confinement of fast particles is a key factor for realising self-sustained fusion energy. This thesis explores fast ion transport induced by perturbed electromagnetic waves through modelling wave-particle interactions and calculating changes in both particle distribution function and particle number during this process. In Chapter 2, the equations of single particle motion and the MHD fluid description for plasmas are reviewed. A kinetic-MHD hybrid model which separately treats thermal and fast plasma components to investigate the wave-particle interaction is also discussed in this chapter.

The hybrid model leads to a wave-particle resonance condition which is expressed in terms of particle motion frequencies and eigenmode frequencies. This motivates the work in Chapter 3 where a full orbit code is developed to solve the charged particle Lorentz motion in a tokamak and work out the poloidal and toroidal motion frequencies as particles complete periodic motion along the torus and in the poloidal cross section directions.

In chapter 4, an application of the particle pushing code is presented. The code is used to generate resonance maps using calculated particle motion

frequencies according to the resonance condition. Experimental evidence of particles being transported in the presence of chirping modes excited by the energetic neutral beams on MAST is also discussed in this chapter. Resonance maps are used to explain this observation and the features of the resonant particle orbits are investigated in detail.

A quantitative study of particle transport is the subject of Chapter 5. An $n=6$ TAE solution is found for a circular tokamak equilibrium configuration. The effect of the eigenmodes and ad-hoc chirping modes on particle transport are evaluated by simulating wave-particle interactions and calculating the perturbed particle distribution function.

6.1 Results

The particle pushing code presented in Chapter 3 has been validated with an analytic study of cyclotron motion in a constant magnetic field. The full orbit code is used to compute particle trajectories using a realistic tokamak magnetic field. Typical particle orbits, i.e. passing and trapped orbits, are calculated for the MAST magnetic configuration. Non-standard orbits such as potato and stagnation orbits are found to be localised near on-axis positions. The capability of the code is then extended to calculate poloidal and toroidal motion frequencies of particles as full orbits are followed in the simulation. Calculations of frequencies do not require additional operations or data post-processing such as Fourier analysis which are always time-consuming and less efficient for large number of particles. The full orbit code is an important numerical tool for the work in the next chapter.

In Chapter 4, a MAST plasma discharge is selected to study fast-ion driven modes and the behaviour of resonant particle orbits. $n = 1$ TAE and

fishbone oscillations with strong chirping are detected by the Mirnov coil array. The observed mode frequencies are approximately 150 and 40 kHz for TAE and fishbones, respectively. It has been found that FIDA measurements are strongly correlated with MHD bursts, indicating a fast particle redistribution occurring due to the excited instabilities. The full orbit code described in Chapter 3 has been used to generate resonance maps and identify particles which satisfy the resonance condition. Those particles could potentially respond to the driven waves. Two branches $p = 0$ and $p = -1$ of resonance are resolved numerically for particles on the mid-plane. The resonant population is broadened because of a chirping mode frequency which could result in an enhanced particle redistribution or loss. The orbits examined suggest a direction for resonant transport induced by the chirping mode, i.e. the resonance shifts towards the plasma core with decreasing chirping frequencies.

Attempts have been made in Chapter 5 to evaluate the transport of a mocked-up alpha particle distribution in the presence of chirping modes. An $n=6$ TAE with eigenfrequency at 481 kHz is numerically found for a near cylindrical equilibrium. The chirping behaviour of the mode frequency is prescribed using a linear function of time. Simulations have shown that particles move outwards from the plasma centre when chirping modes are present while significant particle transport cannot be seen when the mode frequency is constant. The comparison suggests that the inclusion of a chirping frequency is important for understanding the redistribution and loss of fast particles. This result agrees with the conclusion in Chapter 4 which predicts an enhanced resonance between waves and particles could exist due to chirping modes. The resulting redistribution exhibits an asymmetry in position space. The lost region appears aligned with core passing orbits which implies that orbit transitions from passing to trapped might also occur. Some passing

orbits which could enter into the inboard side while circulating the poloidal cross section could transform into trapped orbits which are mostly located at the outboard side. Changes in toroidal angular momentum and energy show particles transport in constants of motion space while they are interacting with the modes. Effects of mode amplitude and chirping rate on particle transport are investigated and an increase of either variable could improve the particle transport for this case.

6.2 Outlook

The effect of chirping modes on fast particle redistribution and loss has been investigated in *HALO* using a simple cylindrical tokamak geometry and mocked-up alpha particle distribution function. To further develop the research, a realistic plasma equilibrium with chirping modes could be a natural follow-up. Here, the fast ion distribution function varies according to fast particle source, whether it is NBI, ICRF or fusion products. A research candidate is the MAST plasma discharge presented in Chapter 4. Plasmas are heated by the NBI and chirping TAE and fishbone oscillations are observed. On the other hand, the MAST-U project has developed a capacity of delivering an off-axis NBI heating in order to mitigate fast ion losses due to instabilities. Therefore, the MAST-U device is a good candidate platform for exploring whether the behaviours demonstrated in the simple case studied are replicated in more realistic scenarios.

An appropriate damping mechanism is currently absent in *HALO* and the mode does not exhibit realistic chirping which matches experiment. This is the reason why we use an ad-hoc linear function to describe the mode evolution during particle redistribution. The current modelling is suggestive

but is unsuitable for providing detailed explanations of experimental observations, i.e. a chirping mode frequency. Work is currently underway to build a collision operator in HALO which should enable more accurate modelling of the evolution of modes in devices such as MAST. Once this is complete it will be possible to self-consistently explore the impact of chirping modes on fast particle redistribution on devices like MAST-U. The calculated mode frequency should be consistent with experimental measurements and this can be a validation of the collisional plasma model.

Bibliography

- [1] J. D. Huba. *NRL plasma formulary*. Vol. 6790. 98-358. Naval Research Laboratory, 1998.
- [2] J. P. Freidberg. *Plasma physics and fusion energy*. Cambridge university press, 2008.
- [3] S. Atzeni and J. Meyer-ter-Vehn. *The Physics of Inertial Fusion: BeamPlasma Interaction, Hydrodynamics, Hot Dense Matter*. Vol. 125. OUP Oxford, 2004.
- [4] E. Moses, J. Lindl, M. Spaeth, R. Patterson, R. Sawicki, L. Atherton, P. Baisden, L. Lagin, D. Larson, B. MacGowan et al. ‘Overview: development of the National Ignition Facility and the transition to a user facility for the ignition campaign and high energy density scientific research’. In: *Fusion Science and Technology* 69.1 (2016), pp. 1–24.
- [5] J. Tollefson et al. ‘US achieves laser-fusion record: what it means for nuclear-weapons research’. In: *Nature* 597.7875 (2021), pp. 163–164.
- [6] M. Shimada et al. ‘Chapter 1: Overview and summary’. In: 47.6 (2007), S1–S17.

- [7] X. Litaudon, S. Abduallev, M. Abhangi, P. Abreu, M. Afzal, K. Aggarwal, T. Ahlgren, J. H. Ahn, L. Aho-Mantila, N. Aiba et al. ‘Overview of the JET results in support to ITER’. In: *Nuclear Fusion* 57.10 (2017), p. 102001.
- [8] P. Barabaschi, Y. Kamada, H. Shirai et al. ‘Progress of the JT-60SA project’. In: *Nuclear Fusion* 59.11 (2019), p. 112005.
- [9] S. E. Wurzel and S. C. Hsu. *Progress toward Fusion Energy Breakeven and Gain as Measured against the Lawson Criterion*. 2021. arXiv: 2105.10954.
- [10] J. Lawson. ‘Some criteria for a useful thermonuclear reactor, AERE’. In: *AERE Report GP/R 1807* (1955).
- [11] J. D. Lawson. ‘Some criteria for a power producing thermonuclear reactor’. In: *Proceedings of the physical society. Section B* 70.1 (1957), p. 6.
- [12] J. R. McNally Jr. ‘Physics of fusion fuel cycles’. In: *Nuclear Technology-Fusion* 2.1 (1982), pp. 9–28.
- [13] T. H. Rider. ‘A general critique of inertial-electrostatic confinement fusion systems’. PhD thesis. Massachusetts Institute of Technology, 1994.
- [14] T. H. Rider. ‘A general critique of inertial-electrostatic confinement fusion systems’. In: *Physics of Plasmas* 2.6 (1995), pp. 1853–1872.
- [15] A. D. Bovet. ‘Suprathermal ion transport in turbulent magnetized plasmas’. PhD thesis. EPFL, 2015.
- [16] Y.-K. Peng and D. Strickler. ‘Features of spherical torus plasmas’. In: *Nuclear Fusion* 26.6 (1986), pp. 769–777.

- [17] U. Stroth, J. Adamek and L. Aho-Mantila. ‘Overview of ASDEX Upgrade results’. In: *Nuclear Fusion* 53.10 (2013), p. 104003.
- [18] R. Buttery, B. Covele, J. Ferron, A. Garofalo, C. Holcomb, T. Leonard, J. Park, T. Petrie, C. Petty, G. Staebler et al. ‘DIII-D research to prepare for steady state advanced tokamak power plants’. In: *Journal of Fusion Energy* 38.1 (2019), pp. 72–111.
- [19] I. Chapman. ‘MAST Upgrade Research Plan’. In: (Nov. 2019). URL: https://ccfe.ukaea.uk/wp-content/uploads/2019/12/MAST-U_RP_2019_v1.pdf.
- [20] J. Menard et al. ‘Overview of the physics and engineering design of NSTX upgrade’. In: *Nuclear Fusion* 52.8 (2012), p. 083015.
- [21] L. Wang. *Toroidal plasma physics experiment lecture notes*. 2013.
- [22] M. Ono and R. Kaita. ‘Recent progress on spherical torus research’. In: *Physics of Plasmas* 22.4 (2015), p. 040501.
- [23] R. Martin. ‘MAST Upgrade – Construction status and early research plans’. In: (2014). URL: http://www-naweb.iaea.org/napc/physics/FEC/FEC2014/fec2014-preprints/239_FIPP826.pdf.
- [24] G. Fishpool, J. Canik, G. Cunningham, J. Harrison, I. Katramados, A. Kirk, M. Kovari, H. Meyer, R. Scannell et al. ‘MAST-upgrade divertor facility and assessing performance of long-legged divertors’. In: *Journal of Nuclear Materials* 438 (2013), S356–S359.
- [25] W. Morris, J. Harrison, A. Kirk, B. Lipschultz, F. Militello, D. Moulton and N. Walkden. ‘MAST upgrade divertor facility: a test bed for novel divertor solutions’. In: *IEEE Transactions on Plasma Science* 46.5 (2018), pp. 1217–1226.

- [26] T. R. Barrett, C. Jones, P. Blatchford, B. Smith, R. McAdams and N. Woods. ‘Engineering design of the double neutral beam injection system for MAST Upgrade’. In: *Fusion engineering and design* 86.6-8 (2011), pp. 789–792.
- [27] M. Turnyanskiy, C. Challis, R. Akers, M. Cecconello, D. Keeling, A. Kirk, R. Lake, S. Pinches, S. Sangaroon and I. Wodniak. ‘Measurement and control of the fast ion redistribution on MAST’. In: *Nuclear Fusion* 53.5 (2013), p. 053016.
- [28] M. Gryaznevich et al. ‘Achievement of Record β in the START Spherical Tokamak’. In: *Phys. Rev. Lett.* 80 (1998), pp. 3972–3975.
- [29] M. Peng. ‘Spherical torus pathway to fusion power’. In: *Journal of fusion energy* 17.1 (1998), pp. 45–59.
- [30] R. D. Stambaugh, V. S. Chan, R. L. Miller and M. J. Schaffer. ‘The spherical tokamak path to fusion power’. In: *Fusion Technology* 33.1 (1998), pp. 1–21.
- [31] A. Costley. ‘Towards a compact spherical tokamak fusion pilot plant’. In: *Philosophical Transactions of the Royal Society A* 377.2141 (2019), p. 20170439.
- [32] E. Gibney. ‘UK hatches plan to build world’s first fusion power plant.’ In: *Nature* (2019).
- [33] T. H. Stix. ‘Heating of toroidal plasmas by neutral injection’. In: *Plasma Physics* 14.4 (1972), p. 367.
- [34] N. J. Fitzgerald. ‘Modelling the neutralisation process in neutral beam injectors’. PhD thesis. Dublin City University, 2009.

- [35] A. Pankin, D. McCune, R. Andre, G. Bateman and A. Kritz. ‘The tokamak Monte Carlo fast ion module NUBEAM in the National Transport Code Collaboration library’. In: *Computer Physics Communications* 159.3 (2004), pp. 157–184.
- [36] E. Hirvijoki, O. Asunta, T. Koskela, T. Kurki-Suonio, J. Miettunen, S. Sipilä, A. Snicker and S. Äkäslompolo. ‘ASCOT: Solving the kinetic equation of minority particle species in tokamak plasmas’. In: *Computer Physics Communications* 185.4 (2014), pp. 1310–1321.
- [37] M. Weiland, R. Bilato, R. Dux, B. Geiger, A. Lebschy, F. Felici, R. Fischer, D. Rittich, M. Van Zeeland, E. M. Team et al. ‘RABBIT: Real-time simulation of the NBI fast-ion distribution’. In: *Nuclear Fusion* 58.8 (2018), p. 082032.
- [38] S. H. Ward, R. Akers, A. S. Jacobsen, P. Ollus, S. D. Pinches, E. Tholerus, R. G. Vann and M. A. Van Zeeland. ‘Verification and validation of the high-performance Lorentz-orbit code for use in stellarators and tokamaks (LOCUST)’. In: *Nuclear Fusion* 61.8 (2021), p. 086029.
- [39] M. Nightingale, G. Crawford, S. Gee, D. Hurford, D. Martin, M. Simmonds, R. Smith, C. Tsai and S. Warder. ‘The MAST neutral beam injection system’. In: *Fusion engineering and design* 56 (2001), pp. 529–532.
- [40] S. Gee, R. Baldwin, A. Borthwick, D. Ciric, G. Crawford, L. Hackett, D. Homfray, D. Martin, J. Milnes, T. Mutters et al. ‘MAST neutral beam long pulse upgrade’. In: *Fusion engineering and design* 74.1-4 (2005), pp. 403–407.

- [41] P. Stevenson, R. Baldwin, V. Dunkley, A. Vadgama and S. Warder. ‘Design and commissioning of the MAST neutral beam power supplies for the long pulse beam upgrade’. In: *2009 23rd IEEE/NPSS Symposium on Fusion Engineering*. IEEE. 2009, pp. 1–4.
- [42] D. Homfray, D. Ciric, V. Dunkley, R. King, D. Payne, M. Simmonds, B. Stevens, P. Stevenson, C. Tame, S. Warder et al. ‘Overview of MAST neutral beam system performance’. In: *2009 23rd IEEE/NPSS Symposium on Fusion Engineering*. IEEE. 2009, pp. 1–4.
- [43] D. A. Homfray, A. Benn, D. Ciric, I. Day, V. Dunkley, D. Keeling, S. Khilar, D. King, R. King, U. Kurutz et al. ‘Real time neutral beam power control on MAST’. In: *Fusion engineering and design* 86.6-8 (2011), pp. 780–784.
- [44] S. Sharapov. *Energetic Particles in Tokamak Plasmas*. CRC Press, 2021.
- [45] L. C. Appel, T. Fülöp, M. Hole, H. Smith, S. D. Pinches, R. Vann, M. team et al. ‘Compressional Alfvén eigenmodes on MAST’. In: *Plasma Physics and Controlled Fusion* 50.11 (2008), p. 115011.
- [46] M. Hole and L. C. Appel. ‘Fourier decomposition of magnetic perturbations in toroidal plasmas using singular value decomposition’. In: *Plasma Physics and Controlled Fusion* 49.12 (2007), p. 1971.
- [47] M. Hole, L. Appel and R. Martin. ‘A high resolution Mirnov array for the Mega Ampere Spherical Tokamak’. In: *Review of Scientific Instruments* 80.12 (2009), p. 123507.
- [48] Y. V. Petrov and R. Harvey. ‘A comparison of RF heating calculated with the CQL3D Fokker-Planck solver and with a Monte-Carlo code’.

- In: *AIP Conference Proceedings*. Vol. 2254. 1. AIP Publishing LLC. 2020, p. 060007.
- [49] K.-L. Wong. ‘A review of Alfvén eigenmode observations in toroidal plasmas’. In: *Plasma physics and controlled fusion* 41.1 (1999), R1.
- [50] H. Duong, W. Heidbrink, E. Strait, T. Petrie, R. Lee, R. Moyer and J. Watkins. ‘Loss of energetic beam ions during TAE instabilities’. In: *Nuclear Fusion* 33.5 (1993), p. 749.
- [51] V. Kiptily, M. Fitzgerald, V. Goloborodko, S. Sharapov, C. Challis, D. Frigione, J. Graves, M. Mantsinen, P. Beaumont, M. Garcia-Munoz et al. ‘Fusion product losses due to fishbone instabilities in deuterium JET plasmas’. In: *Nuclear Fusion* 58.1 (2017), p. 014003.
- [52] M. Fitzgerald, J. Buchanan, S. Sharapov, V. Kiptily, M. Sertoli, G. Szepesi, J. Boom, R. Akers, D. King et al. ‘Full-orbit and drift calculations of fusion product losses due to explosive fishbones on JET’. In: *Nuclear Fusion* 59.1 (2018), p. 016004.
- [53] W. Heidbrink. ‘Basic physics of Alfvén instabilities driven by energetic particles in toroidally confined plasmas’. In: *Physics of Plasmas* 15.5 (2008), p. 055501.
- [54] H. Alfvén. ‘Existence of electromagnetic-hydrodynamic waves’. In: *Nature* 150.3805 (1942), pp. 405–406.
- [55] S. Sharapov. ‘MHD and fast particles in tokamaks’. In: (Sept. 2018). URL: https://juser.fz-juelich.de/record/283637/files/Sharapov_E1-4.pdf.
- [56] G. Fu, C. Cheng, R. Budny, Z. Chang, D. Darrow, E. Fredrickson, E. Mazzucato, R. Nazikian and S. Zweben. ‘Stability analysis of

- toroidicity-induced Alfvén eigenmodes in TFTR deuterium-tritium experiments’. In: *Physical review letters* 75.12 (1995), p. 2336.
- [57] W. Kerner, D. Borba, S. Sharapov, B. Breizman, J. Candy, A. Fasoli, L. Appel, R. Heeter, L.-G. Eriksson and M. Mantsinen. ‘Theory of Alfvén eigenmode instabilities and related alpha particle transport in JET deuterium-tritium plasmas’. In: *Nuclear fusion* 38.9 (1998), p. 1315.
- [58] E. Carolipio, W. Heidbrink, C.-Z. Cheng, M.-S. Chu, G. Fu, A. Jaun, D. Spong, A. Turnbull and R. White. ‘The toroidicity-induced Alfvén eigenmode structure in DIII-D: Implications of soft x-ray and beam-ion loss data’. In: *Physics of Plasmas* 8.7 (2001), pp. 3391–3401.
- [59] M. Van Zeeland, G. Kramer, M. Austin, R. Boivin, W. Heidbrink, M. Makowski, G. McKee, R. Nazikian, W. Solomon and G. Wang. ‘Radial structure of Alfvén eigenmodes in the DIII-D tokamak through electron-cyclotron-emission measurements’. In: *Physical review letters* 97.13 (2006), p. 135001.
- [60] L. Chen. ‘Theory of magnetohydrodynamic instabilities excited by energetic particles in tokamaks’. In: *Physics of Plasmas* 1.5 (1994), pp. 1519–1522.
- [61] M. Cecconello, O. Jones, W. Boeglin, R. Perez, D. Darrow, I. Klimek, S. Sharapov, M. Fitzgerald, K. McClements, D. Keeling et al. ‘Energetic ion behaviour in MAST’. In: *Plasma Physics and Controlled Fusion* 57.1 (2015), p. 014006.
- [62] O. Jones, M. Cecconello, K. McClements, I. Klimek, R. Akers, W. Boeglin, D. Keeling, A. Meakins, R. Perez, S. Sharapov et al. ‘Measurements and modelling of fast-ion redistribution due to

- resonant MHD instabilities in MAST'. In: *Plasma Physics and Controlled Fusion* 57.12 (2015), p. 125009.
- [63] S. Pinches, V. Kiptily, S. Sharapov, D. Darrow, L.-G. Eriksson, H.-U. Fahrbach, M. Garcia-Muñoz, M. Reich, E. Strumberger, A. Werner et al. 'Observation and modelling of fast ion loss in JET and ASDEX Upgrade'. In: *Nuclear fusion* 46.10 (2006), S904.
- [64] K. McClements and E. Fredrickson. 'Energetic particles in spherical tokamak plasmas'. In: *Plasma Physics and Controlled Fusion* 59.5 (2017), p. 053001.
- [65] J. Dawson. 'On landau damping'. In: *The physics of fluids* 4.7 (1961), pp. 869–874.
- [66] F. Porcelli, R. Stankiewicz, W. Kerner and H. L. Berk. 'Solution of the drift-kinetic equation for global plasma modes and finite particle orbit widths'. In: *Physics of plasmas* 1.3 (1994), pp. 470–480.
- [67] R. G. Littlejohn. 'Variational principles of guiding centre motion'. In: *Journal of Plasma Physics* 29.1 (1983), pp. 111–125.
- [68] J. P. Freidberg. *ideal MHD*. Cambridge University Press, 2014.
- [69] H. Grad and H. Rubin. 'Hydromagnetic equilibria and force-free fields'. In: *Journal of Nuclear Energy (1954)* 7.3-4 (1958), pp. 284–285.
- [70] V. D. Shafranov. 'Equilibrium of a toroidal plasma in a magnetic field'. In: *Journal of Nuclear Energy. Part C, Plasma Physics, Accelerators, Thermonuclear Research* 5.4 (1963), p. 251.
- [71] L. Lao, H. S. John, R. Stambaugh, A. Kellman and W. Pfeiffer. 'Reconstruction of current profile parameters and plasma shapes in tokamaks'. In: *Nuclear fusion* 25.11 (1985), p. 1611.

- [72] L. Appel, I. Lupelli and J. Contributors. ‘Equilibrium reconstruction in an iron core tokamak using a deterministic magnetisation model’. In: *Computer Physics Communications* 223 (2018), pp. 1–17.
- [73] N. Conway, M. De Bock, C. Michael, M. Walsh, P. Carolan, N. Hawkes, E. Rachlew, J. McCone, S. Shibaev and G. Wearing. ‘The MAST motional Stark effect diagnostic’. In: *Review of Scientific Instruments* 81.10 (2010), p. 10D738.
- [74] R. Scannell, M. Walsh, M. Dunstan, J. Figueiredo, G. Naylor, T. O’Gorman, S. Shibaev, K. Gibson and H. Wilson. ‘A 130 point Nd: YAG Thomson scattering diagnostic on MAST’. In: *Review of Scientific Instruments* 81.10 (2010), p. 10D520.
- [75] N. Conway, P. Carolan, J. McCone, M. Walsh and M. Wisse. ‘High-throughput charge exchange recombination spectroscopy system on MAST’. In: *Review of scientific instruments* 77.10 (2006), 10F131.
- [76] A. Mikhailovskii, G. Huysmans, W. Kerner and S. Sharapov. ‘Optimization of computational MHD normal-mode analysis for tokamaks’. In: *Plasma Physics Reports* 23.10 (1997), pp. 844–857.
- [77] L. D. Landau. ‘On the vibrations of the electronic plasma’. In: *Zh. Eksp. Teor. Fiz.* 10 (1946), p. 25.
- [78] J. W. Thomas. *Numerical partial differential equations: finite difference methods*. Vol. 22. Springer Science & Business Media, 2013.
- [79] J. P. Boris and R. A. Shanny. *Proceedings: Fourth Conference on Numerical Simulation of Plasmas, November 2, 3, 1970*. Naval Research Laboratory, 1972.

- [80] H. Qin, S. Zhang, J. Xiao, J. Liu, Y. Sun and W. M. Tang. ‘Why is Boris algorithm so good?’ In: *Physics of Plasmas* 20.8 (2013), p. 084503.
- [81] D. McCune. ‘NTCC PSPLINE Module’. In: (1999). URL: <https://w3.pppl.gov/ntcc/PSPLINE/>.
- [82] J. A. Rome and Y. M. Peng. ‘The topology of tokamak orbits’. In: *Nuclear fusion* 19.9 (1979), p. 1193.
- [83] C. Michael, N. Conway, B. Crowley, O. Jones, W. Heidbrink, S. Pinches, E. Braeken, R. Akers, C. Challis, M. Turnyanskiy et al. ‘Dual view FIDA measurements on MAST’. In: *Plasma Physics and Controlled Fusion* 55.9 (2013), p. 095007.
- [84] W. Heidbrink, Y. Luo, K. Burrell, R. Harvey, R. Pinsker and E. Ruskov. ‘Measurements of fast-ion acceleration at cyclotron harmonics using Balmer-alpha spectroscopy’. In: *Plasma Physics and Controlled Fusion* 49.9 (2007), p. 1457.
- [85] M. Salewski, B. Geiger, D. Moseev, W. Heidbrink, A. S. Jacobsen, S. B. Korsholm, F. Leipold, J. Madsen, S. K. Nielsen, J. Rasmussen et al. ‘On velocity-space sensitivity of fast-ion D-alpha spectroscopy’. In: *Plasma Physics and Controlled Fusion* 56.10 (2014), p. 105005.
- [86] K. McClements, K. Tani, R. Akers, Y. Liu, K. Shinohara, H. Tsutsui and S. Tsuji-Iio. ‘The effects of resonant magnetic perturbations and charge-exchange reactions on fast ion confinement and neutron emission in the Mega Amp Spherical Tokamak’. In: *Plasma Physics and Controlled Fusion* 60.9 (2018), p. 095005.

- [87] K. Tani, K. Shinohara, T. Oikawa, H. Tsutsui, K. McClements, R. Akers, Y. Liu, M. Suzuki, S. Ide, Y. Kusama et al. ‘Application of a non-steady-state orbit-following Monte-Carlo code to neutron modeling in the MAST spherical tokamak’. In: *Plasma Physics and Controlled Fusion* 58.10 (2016), p. 105005.
- [88] H. Berk, B. Breizman, J. Candy, M. Pekker and N. Petviashvili. ‘Spontaneous hole–clump pair creation’. In: *Physics of Plasmas* 6.8 (1999), pp. 3102–3113.
- [89] M. Fitzgerald, J. Buchanan, R. J. Akers, B. N. Breizman and S. Sharapov. ‘HALO: A full-orbit model of nonlinear interaction of fast particles with eigenmodes’. In: *Computer Physics Communications* 252 (2020), p. 106773.
- [90] S. Pinches, L. Appel, J. Candy, S. Sharapov, H. Berk, D. Borba, B. Breizman, T. Hender, K. Hopcraft, G. Huysmans et al. ‘The HAGIS self-consistent nonlinear wave-particle interaction model’. In: *Computer Physics Communications* 111.1-3 (1998), pp. 133–149.
- [91] R. Akers, E. Verwichte, T. Martin, S. Pinches and R. Lake. ‘GPGPU Monte Carlo calculation of gyro-phase resolved fast ion and n-state resolved neutral deuterium distributions’. In: *39th EPS Conference on Plasma Physics 2012, EPS 2012 and the 16th International Congress on Plasma Physics*. 2012, pp. 1822–1825.
- [92] J. M. Hammersley and D. Handscomb. ‘Percolation processes’. In: *Monte Carlo Methods*. Springer, 1964, pp. 134–141.
- [93] T.-T. Wong, W.-S. Luk and P.-A. Heng. ‘Sampling with Hammersley and Halton points’. In: *Journal of graphics tools* 2.2 (1997), pp. 9–24.

- [94] G. Huysmans, S. Sharapov, A. Mikhailovskii and W. Kerner.
‘Modeling of diamagnetic stabilization of ideal magnetohydrodynamic instabilities associated with the transport barrier’. In: *Physics of Plasmas* 8.10 (2001), pp. 4292–4305.
- [95] G. Huysmans, J. Goedbloed, W. Kerner et al. ‘Isoparametric bicubic Hermite elements for solution of the Grad-Shafranov equation’. In: *International Journal of Modern Physics C* 2.01 (1991), pp. 371–376.
- [96] J. Candy, D. Borba, H. Berk, G. Huysmans and W. Kerner.
‘Nonlinear interaction of fast particles with Alfvén waves in toroidal plasmas’. In: *Physics of Plasmas* 4.7 (1997), pp. 2597–2611.

Colophon

This thesis is based on a template developed by Matthew Townson and Andrew Reeves. It was typeset with L^AT_EX 2_ε. It was created using the *memoir* package, maintained by Lars Madsen, with the *madsen* chapter style. The font used is Latin Modern, derived from fonts designed by Donald E. Kuth.